ARTERIAL TORTUOSITY MEASUREMENT SYSTEM FOR EXAMINING CORRELATIONS WITH VASCULAR DISEASE

by

Karl Thomas Diedrich

A dissertation submitted to the faculty of
The University of Utah
in partial fulfillment of the requirements for the degree of

Doctor of Philosophy

Department of Biomedical Informatics

The University of Utah

December 2011

The University of Utah Graduate School

STATEMENT OF DISSERTATION APPROVAL

The dissertation of **Karl Thomas Diedrich**

has been approved by the following supervisory committee members:

Dennis Parker, Chair		**7/14/2011** Date Approved
John Roberts, Member		**7/14/2011** Date Approved
Richard Schmidt, Member		**7/14/2011** Date Approved
Lisa Cannon Albright, Member		**7/14/2011** Date Approved
Paul Clayton, Member		**7/19/2011** Date Approved

And by **Joyce Mitchell**, Chair of

the Department of **Biomedical Informatics**

and by Charles A. Wight, Dean of the The Graduate School.

ABSTRACT

High arterial tortuosity, or twistedness, is a sign of many vascular diseases. Some ocular diseases are clinically diagnosed in part by assessment of increased tortuosity of ocular blood vessels. Increased arterial tortuosity is seen in other vascular diseases but is not commonly used for clinical diagnosis. This study develops the use of existing magnetic resonance angiography (MRA) image data to study arterial tortuosity in a range of arteries of hypertensive and intracranial aneurysm patients.

The accuracy of several centerline extraction algorithms based on Dijkstra's algorithm was measured in numeric phantoms. The stability of the algorithms was measured in brain arteries. A centerline extraction algorithm was selected based on its accuracy. A centerline tortuosity metric was developed using a curve of tortuosity scores. This tortuosity metric was tested on phantoms and compared to observer-based tortuosity rankings on a test data set. The tortuosity metric was then used to measure and compare with negative controls the tortuosity of brain arteries from intracranial aneurysm and hypertension patients.

A Dijkstra based centerline extraction algorithm employing a distance-from-edge weighted center of mass (DFE-COM) cost function of the segmented arteries was selected based on generating 15/16 anatomically correct centerlines in a looping artery

compared to 15/16 for the center of mass (COM) cost function and 7/16 for the inverse modified distance from edge cost function. The DFE-COM cost function had a lower root mean square error in a lopsided phantom (0.413) than the COM cost function (0.879). The tortuosity metric successfully ordered electronic phantoms of arteries by tortuosity. The tortuosity metric detected an increase in arterial tortuosity in hypertensive patients in 13/13 (10/13 significant at $\alpha = 0.05$). The metric detected increased tortuosity in a subset of the aneurysm patients with Loeys-Dietz syndrome (LDS) in 7/7 (three significant at $\alpha = 0.001$).

The tortuosity measurement combination of the centerline algorithm and the distance factor metric tortuosity curve was able to detect increases in arterial tortuosity in hypertensives and LDS patients. Therefore the methods validated here can be used to study arterial tortuosity in other hypertensive population samples and in genetic subsets related to LDS.

To my family Mi-Young, Han and Leo and to the memory of Kim Kil-Soon.

TABLE OF CONTENTS

ABSTRACT iii

LIST OF TABLES x

LIST OF ABBREVIATIONS USED xii

ACKNOWLEDGEMENTS xv

1. INTRODUCTION 1

Objective 1
Arterial tortuosity 1
Clinical diagnosis by arterial tortuosity 1
Medical implications of tortuosity 3
Tortuosity types 4
Tortuosity measures 4
Relationship between tortuosity types and measures 5
Quantitatively measured vascular diseases 5
Arterial tortuosity measurement method 6
Imaging blood vessels 7
Risks of ionizing radiation in imaging 7
Nuclear magnetic resonance imaging safety 8
Nuclear magnetic resonance basics 8
MRI hardware components 10
Generation of MRI image 12
Time-of-flight magnetic resonance angiography 14
Filling a gap in research 15
Tortuosity measurement and analysis system 16
Experimental papers 17
References 21

2. COMPARING PERFORMANCE OF CENTERLINE ALGORITHMS FOR QUANTITATIVE ASSESSMENT OF BRAIN VASCULAR ANATOMY 26

Abstract 27

Introduction 28
Materials and methods 30
Source images 30
Tools 31
Segmentation 31
Cost function segmentation preprocessing 31
Centerline algorithms 33
Stability measure 34
Accuracy 35
Results 36
Phantom centerline stability and accuracy 36
Stability and accuracy on phantoms with noise 37
Artery centerline stability 37
Discussion 40
Conclusion 43
Acknowledgements 43
Literature cited 61
Supplementary materials 63
Source images 63
Segmentation 63
Literature cited 65

3. VALIDATION OF AN ARTERIAL TORTUOSITY MEASURE WITH APPLICATION TO HYPERTENSION COLLECTION OF CLINICAL HYPERTENSIVE PATIENTS 67

Abstract 69
Background 69
Methods 69
Results 70
Conclusions 70
Background 70
Methods 73
Image analysis flow 73
Centerline cost functions 74
Numeric phantom generation 75
Centerline stability and accuracy 75
Tortuosity measurement 76
Tortuosity measurement of phantoms 76
Segmentation 77
Human source images for hypertension tortuosity study 77
MRI scanners 79
Arteries measured 79
Filtering the images 80

Resolution and interpolation 80
Tortuosity comparisons 81
Results 81
Centerline stability and accuracy 81
Tortuosity measurement of phantoms 82
Median filter effect 83
Resolution and interpolation effect on tortuosity 83
Comparison of negative control populations 84
Female and male comparisons 85
Korean hypertension tortuosity comparison 86
Utah hypertension 87
Discussion 87
Conclusions 90
List of abbreviations used 91
Competing interests 92
Authors' contributions 92
Acknowledgements 92
References 125

4. MEDICAL RECORD AND IMAGING EVALUATION TO IDENTIFY ARTERIAL TORTUOSITY PHENOTYPE IN POPULATIONS AT RISK FOR INTRACRANIAL ANEURYSMS 128

Abstract 130
Introduction 130
Materials and methods 132
Source images 132
Arterial tortuosity measurement summary 132
Tools 133
Statistical tests 134
Segmentation 134
Centerlines 134
Artery selection and tortuosity measurement 135
Visual correlation 135
Results 137
Discussion 139
Acknowledgments 143
References 155

5. CONCLUSION 158

Developing the use of arterial tortuosity 158
Validation of arterial tortuosity measurement 159
Quantitative image phenotype measurement of genotype 161

Flexible analysis system 161
Value of quantitative measurement 162
Secondary use of image data 163
Future work 164
Arterial tortuosity in hypertension 164
Arterial tortuosity in LDS 165
Quantitative phenotypes 167
Contribution to the field of bioinformatics 168
Summary 169
References 170

LIST OF TABLES

2.1. Helix line phantom stability and accuracy 58

2.2. Comparison of algorithm stability and accuracy on phantoms 58

2.3. Comparison of centerline algorithms on MRA brain images 58

2.4. Means by algorithm 59

2.5. Algorithm centerline stability measurements 60

3.1. Tortuosity curve measurement point……..……..120

3.2. Comparison of algorithm stability and accuracy of comb phantom 120

3.3. Comparison of algorithm stability and accuracy on 3 branch phantom 121

3.4. Comparison of centerline algorithms on MRA brain images 122

3.5. Helix phantom tortuosity 123

3.6. Negative control demographics 123

3.7. Utah retrospective tortuosity comparison 124

4.1. Aneurysm cases versus negative control tortuosity comparisons……..……..149

4.2. Negative control age comparisons 150

4.3. Familial aneurysm cases versus negative control tortuosity comparisons 151

4.4. Loeys-Dietz/Marfan syndrome cases versus negative control tortuosity comparisons 152

4.5. Nonfamilial aneurysms versus negative control tortuosity comparisons 153

4.6. High-risk relative cases versus negative control tortuosity comparisons 154

LIST OF ABBREVIATIONS USED

ACA anterior cerebral artery

Acom anterior communicating artery

ADC analog to digital converter

B magnetic field

BT binary thinning

COL Collagen

COM center of mass

d distance

DFE distance from edge

DFM distance factor metric

DFM3 smoothed distance factor metric

DNA deoxyribonucleic acid

DSA Digital subtraction angiographyFBN fibrillin

G gradient

HTN hypertensive

IA intracranial aneurysm

ICA internal carotid artery

ICM Inflection count metric

IRB institutional review board

L left

L length

L3 smoothed length

LDS Loeys-Dietz syndrome

M bulk magnetization

MFS Marfan syndrome

MIP maximum intensity projection

MR magnetic resonance

MRA magnetic resonance angiography

MRI magnetic resonance imaging

NEG negative

NMR nuclear magnetic resonance

R right

RF radio frequency

SOAM Sum of angles metric

T Tesla

TGF Transforming growth factor

TGFBR Transforming growth factor beta receptor

TOF time of flight

T_1 longitudinal relaxtion time

T_2 transverse relaxation time

T_E echo time

T_{pe} phase encoding time

T_R repetition time

U.S.A United States of America

UT Utah

ZBS Z buffer segmentation

ACKNOWLEDGEMENTS

I would like to thank the members of my committee, Dennis Parker, John Roberts, Richard Schmidt, Lisa Cannon Albright, and Paul Clayton for their guidance that allowed me to expand my research potential.

I thank my co-authors John Roberts, Richard Schmidt, Lisa Canon-Albright, Dennis Parker, Chang-Ki Kang, Zang-Hee Cho, and Anji T. Yetman who helped obtain the data necessary for this research.

I would like to express many thanks to the students and staff at Utah Center for Advanced Imaging Research (UCAIR).

Finally I express thanks to my family Mi-Young, Han and Leo and my parents Charles and Sandra who supported me in returning to graduate school.

CHAPTER 1

INTRODUCTION

Objective

Many vascular diseases affect arteries altering lumen diameter, vessel wall thickness and shape. One method used to quantify the shape of arteries is to measure their tortuosity or twistedness. Diseased arteries may have increased arterial tortuosity compared to healthy arteries. *This research developed software for quantitatively measuring and comparing tortuosities of arteries from disease and negative control populations to determine which diseases are associated with arterial tortuosity.*

Arterial tortuosity

Clinical diagnosis by arterial tortuosity

Some vascular diseases are known to correlate with increased arterial tortuosity. Arterial tortuosity is included in diagnosis before venous tortuosity because arteries are under higher pressure than veins and will be affected by pressure more. Arteries were found in vitro to exhibit increased tortuosity with increasing pressure [1]. Arteries are afflicted by aneurysms more often than veins. Autopsy studies have shown intracranial aneurysm rates of 0.2 to 9.9 (mean 5%) percent in the general population [2], whereas a retrospective study at Walter Reed Army Medical Center found venous aneurysms in 30

of 2000 patients (1.5%) and this hospital population may be an overestimate of the frequency in the general population [3]. Ophthalmologists and other clinicians use high tortuosity of the retinal blood vessels seen in fundus photographs of the dilated pupil to diagnose retinal diseases such as retinopathy of prematurity [4]. High tortuosity is also used to diagnose retinitis pigmentosa and diabetic retinopathy, and low tortuosity is used to identify retinal vasculitis [5]. Rapidly growing cancer tumors recruit new highly tortuous arteries by angiogenesis [6]. Genetic syndromes such as arterial tortuosity syndrome [7] and Loeys-Dietz syndrome (LDS) [8, 9] are known to increase arterial tortuosity.

Arterial tortuosity is one of the differentiating characteristics between the rare and newly described LDS and the more common (occurring in 2-3 per 10000 individuals) and better known Marfan syndrome (MFS) [10] [11-15]. In addition patients with LDS have also been misdiagnosed with Ehlers-Danlos syndrome type IV, which is caused by a mutation in the COL3A1 gene and is not known for high arterial tortuosity [7]. In a study of 25 LDS patients all 25 were visually assessed as having high arterial tortuosity [16]. LDS causes aneurysms in a wider anatomical area than MFS requiring imaging over a wider range of anatomy, making the correct LDS diagnosis important [17]. Arterial tortuosity may be a distinguishing characteristic between LDS and related diseases.

Distinguishing between MFS and LDS is important. LDS is a highly aggressive disease. Twenty per cent of LDS patients have aneurysms of the head or neck [9]. Mean age at death for LDS type I (TGFBR1 mutation) was 22.6 versus 31.8 for type II (TGFBR2 mutation) [9]. The clinical presentation of LDS type I and II had no apparent

differences [9]. MFS and LDS have many overlapping clinical characteristics making misdiagnosis possible [14]. MFS patients are only followed with aortic arch imaging whereas LDS patients need more comprehensive imaging to detect aneurysms in other parts of the body [12, 17]. MFS patients get aortic arch aneurysms that can rupture. MFS patients show no abnormal risk of nonaortic arch aneurysms while 92% of LDS patients develop other aneurysms [8].

Currently the clinical diagnosis of retinal diseases and LDS includes visual qualitative assessment of blood vessel tortuosity. Validation of quantitative tortuosity measurements is needed to develop quantitative tortuosity measurement for clinical diagnosis.

Medical implications of tortuosity

Tortuosity of blood vessels has medical implications. Highly tortuous arterioles may require high blood pressure (hypertension) to push blood cells through small twisted arterioles [18]. Highly twisted arteries have physically prevented stenting [19]. High arterial tortuosity may also be a sign of weakened arterial walls caused by defects in proteins such as elastin [1]. The force of blood moving parallel with the blood vessels may stretch them increasing length causing tortuosity [1]. Blood pressure forces perpendicular to the blood vessels may stretch the walls out resulting in aneurysms [1]. Thus high arterial tortuosity could be a sign of existing vascular disease and a warning of future disease.

Tortuosity types

Vascular diseases cause different types of tortuosity. Tortuosity has been characterized in three types [20]. In type I tortuosity arteries exhibit broad meandering curves. High type II tortuosity arteries have dense nests of curved and erratically twisting vessels of a variety of lengths. The final type III tortuosity arteries have high frequency low amplitude coils or sinusoidal curves [20]. Type I tortuosity broadly affects arteries' complete structure and is likely caused by underlying systemic disease. Type II tortuosity has been associated with arteriovenous malformations and III tortuosity has been associated with tumor angiogenesis [20].

Tortuosity measures

Several methods to measure arterial tortuosity have been developed. Most tortuosity measurements are made on centerlines through the middle of the arteries. Centerlines simplify the arteries to a single line passing through the middle of the artery making measurement of length possible. The distance factor metric (DFM) measures the ratio of the length L along arterial centerlines divided by the straight distance d between two end-points [4, 20-25]. The inflection count metric (ICM) multiplies the number of direction changes by the DFM to factor in the number of changes in direction [20, 26]. The sum of angles metric (SOAM) measures a sum of angles along the centerline [20, 26]. The tortuosity measure used on arterioles in microscopy slides measures the ratio of the length of the largest twist in the blood vessel to the largest diameter of the blood vessel [27]. Other tortuosity measurement methods use the integral of the derivative or

second derivative of the centerline that is sensitive to abrupt changes along the centerline [22, 28]. The different tortuosity measures vary in which types of arterial tortuosity they detect.

Relationship between tortuosity types and measures

Different existing measures of tortuosity work better for different types of tortuosity. The most commonly used measure has been the DFM partly due to its simplicity of implementation. The DFM performs well detecting high type I tortuosity arteries but not well detecting high type II and type III [20]. The SOAM performed well on type III but not on type I or II. The inflection count metric (ICM) [20] worked well detecting type I and type II tortuosity. The SOAM and ICM measurements were developed to measure small areas of local tortuosity seen in tumor angiogenesis [20, 28].

Quantitatively measured vascular diseases

Previous research has correlated several vascular diseases with quantitative tortuosity metrics. DFM based methods detected increased arterial tortuosity in retinal blood vessels with retinopathy of prematurity [1]. Measurements based on the integral of second derivative of the centerline measured increases in retinal blood vessel tortuosity with retinitis pigmentosa and diabetic retinopathy and decreased tortuosity with vasculitis compared to normal controls [2]. The ratio of the diameter of the largest loop to largest vascular diameter measure detected an increase in arteriolar tortuosity in brain blood

vessels from autopsy in hypertensive patients [27]. The SOAM measured an increase in arterial tortuosity with aging in magnetic resonance angiography (MRA) images while the ICM measurement did not in the same data set [29]. The ICM found a decrease in tortuosity of the middle cerebral arteries from MRA images with increased cardiovascular exercise which was not seen with the SOAM measurement [30]. However many diseases, even some known to increase arterial tortuosity visually, have not been quantitatively investigated and clinical use of quantitative measurement is not widespread and only appears to be used consistently with retinal arteries.

Arterial tortuosity measurement method

This study is concerned with the relationship between blood vessel tortuosity and vascular disease. The study started with the DFM tortuosity measure due to its ability to detect type I tortuosity and simplicity of implementation. Tortuosity measure by curvature of the centerline was also implemented by numeric integration of the second derivative along the centerline. The curvature required specification of many implementation parameters that change the measures. The DFM tortuosity measure was free of implementation parameters. The study started with the DFM tortuosity measure to detect arterial tortuosity. When and if the DFM tortuosity measure proved ineffective modifications were made to the measure. The tortuosity measurement software developed can substitute alternative measures of tortuosity if the DFM is inadequate.

Imaging blood vessels

Blood vessels can be imaged for tortuosity measurement by several different modalities. Retinal blood vessels are routinely imaged in two dimensions in fundus photography by ophthalmologists [21, 31]. Small arterioles are imaged in two-dimensional histological photomicrographs but only in autopsies [27, 32]. Digital subtraction angiography (DSA) with contrast agents creates high resolution two-dimensional projection images that can display small arteries and veins [33]. CTA with contrast agents images both arteries and veins in three dimensions. And MRA can image both arteries and veins or arteries only in three dimensions. MRA's ability to isolate arteries (Figure 1.1 A) from veins simplifies measurement of arteries [34] since veins can obscure the arteries (Figure 1.1 B).

Risks of ionizing radiation in imaging

DSA and CTA expose the patients to ionizing radiation and contrast agents. Ionizing radiation potentially increases the risk of cancer in a linear no lower threshold manner [35]. No lower threshold means that when large numbers of patients are exposed to even small radiation doses, cancers are generated by the imaging [36-38]. Contrast agents used in DSA and CTA can have side effects. Patients can be allergic to contrast agents [34]. Nonionizing, noncontrast MRA imaging is preferred for safety [39, 40].

Nuclear magnetic resonance imaging safety

Nuclear magnetic resonance (NMR) is the basis of magnetic resonance imaging (MRI) and MRA which can image blood vessels without ionizing radiation or contrast. MRI scanners typically measure the collective signal from the protons that are the nuclei of hydrogen atoms from water and lipids and other hydrocarbons in the body. Therefore the magnetic resonance (MR) signal comes from the subject themselves although MRI scanners emit nonionizing radiation waves to image subjects. Added ionizing radiation or contrast agents are not required. Contrast agents do exist that can be injected to increase image contrast between different tissues, but are not always necessary. Thus MRI has no known long term side effects [39, 41].

Nuclear magnetic resonance basics

The following provides a classical physics description of NMR. The NMR signal employed in MRI typically comes from the hydrogen proton nuclei. Imaging based on the nuclei of other atoms exists but is less common. The protons have nuclear magnetic moments μ that in the absence of an applied magnetic field are oriented in random directions and sum to produce zero net bulk magnetization $M = \Sigma\mu_{all} = 0$. In the presence of a magnetic field B, any given magnetic moment μ will precess about the direction of the applied field B with a frequency known as the Larmor frequency: $\omega = \gamma B$. The type of atom determines the gyromagnetic ratio γ, which is 42.58 MHz/Tesla (T) for hydrogen. The magnetic moments μ will not produce a measurable signal until they come into alignment with each other. When the protons of a subject are exposed to a large external

magnetic field vector B_0, after a short time through a process known as relaxation, the magnetic moments have a tendency to align parallel with the field to sum to produce a net longitudinal bulk magnetization $M = \Sigma\mu_{all} > 0$. The bulk magnetization M is then manipulated to produce the measured NMR signal that is used to reconstruct the anatomical image.

An additional electromagnetic radio frequency (RF) pulse B_1 applied perpendicular to the B_0 field at the resonance frequency, ω, tips the bulk magnetization M out of alignment with B_0. At this point, the bulk magnetization vector M has a longitudinal component M_z and transverse component M_{xy} with a tip angle α between the vector of M and the vector of B_0 (Figure 1.2). Like the underlying magnetic moments μ, M precesses or wobbles around the B_0 vector axis like a spinning top or dreidle in a cone pattern with a transverse M_{xy} bulk magnetization component perpendicular to the B_0 field. The M_{xy} component of the magnetization forms the basis of the detected NMR signal. After tipping, through a process of relaxation the bulk magnetization returns to alignment with B_0 recovering the M_z component while reducing the M_{xy} component.

The recovery of M_z and M_{xy} to equilibrium is known as relaxation. The speed of relaxation is tissue dependent. Two forms of relaxation exist governing the recovery of M_z and the destruction of M_{xy}. Each specific tissue has a longitudinal T_1, related to the recovery of M_z, and transverse T_2, related to the loss of M_{xy}. Tissue specific differences in T_1 and T_2 and the proton density (PD) (increased proton density increases signal) are used to create contrast between tissues and highlight and suppress desired tissues with an MRI scanner.

MRI hardware components

An MRI scanner has three main hardware components: a main magnet, a magnetic field gradient system, and a radio frequency (RF) system [39]. The main magnet creates a static homogeneous magnetic field B_0. The subject is placed in the magnetic field and the bulk magnetization M of the subject aligns with the B_0 field. The gradient system alters the local magnetic environment to allow localization of the bulk magnetization. The RF system tips the magnetization away from B_0 and receives signals produced by the precessing transverse bulk magnetization M_{xy} [39, 41].

Main magnet

The main magnet is typically a cooled superconducting magnet that creates the strong nearly uniform static field B_0. Good image quality requires homogeneity of the magnetic field B_0, which the main magnet is usually not capable of alone. Shim coils add magnetic field to even out the B_0 field of the main magnet. The magnets are contained in a long hollow cylindrical shaped case with a hollow bore. The subject lies on a movable table that slides into the hollow bore for imaging.

MRI scanners now typically come in 1.5 T, 3.0 T and 7.0 T field strengths. A Tesla (T) is the Système international d'unités (SI) unit of magnetic field strength. For comparison the Earth's magnetic field at the equator is 31 μT and a refrigerator magnet is around 5 mT. MRI scanners at 1.5 T and 3.0 T are FDA approved and are commonly used in clinical imaging. Scanners at 7.0 T are not FDA approved for clinical use but can be used with institutional review board (IRB) approval for research purposes only.

Higher field strengths have increased signal to noise ratios which can be employed to acquire images at higher resolutions making imaging of smaller arteries possible [42-44].

Gradient fields

A gradient in the main B_0 field is needed for signal localization to create the three-dimensional image. Without the gradient the scanner could detect tissue signals but would not know where the tissues are located and would not be able to reconstruct the image. Gradients G_x, G_y and G_z are created by coil systems positioned around the bore and each modify the z-component of the main field along the spatial x, y and z directions, respectively. The field due to the gradients $B_g = xG_x + yG_y + zG_z$ changes the magnetic field $B = B_0 + B_g$ making the resonance frequency $\omega = \gamma(B_0 + xG_x + yG_y + zG_z)$ a function of position. In practice the gradients are seldom all turned on at the same time but are turned on and off as part of the image acquisition process.

Radio frequency system

The radio frequency (RF) system has transmitter and receiver coils. Some systems use a combined transceiver coil. The transmitter applies uniform B_1 magnetic fields perpendicular to B_0 at specific resonance frequency to the subject. MRI scanners come with whole body coils inside the case of the main magnet and specially designed surface coils which may be placed close to anatomy of interest [39]. Surface coils placed on or close to the subject to increase signal to noise ratio in a small field of view help imaging

small structures such as narrow diameter arteries [45]. After the transmitted B_1 RF ends, the receiver coils detect the precession of the transverse bulk magnetization M_{xy}.

Generation of MRI image

The MR image is acquired by sampling NMR signals from the transverse bulk magnetization M_{xy} of the subject. The RF system and gradients are used to manipulate and sample signals of the bulk magnetization M throughout the spatial frequency or Fourier domain also known as k-space described below. Successive manipulations measure sample frequencies throughout k-space. When k-space has been completely sampled the anatomical spatial domain is recovered by an inverse Fourier transform [39, 41].

First, the gradient coils are used to select a slab for excitation. A G_z gradient alters the resonance frequency linearly of the protons along the Z axis parallel to B_0 according to $\omega(z) = \gamma(B_0 + zG_z)$. The transmission RF coils apply B_1 perpendicular to B_0 in a pulse at a narrow band width of resonance frequencies exciting a slab perpendicular to B_0 with known Z location. The G_z gradient and B_1 RF pulse are ended. Localization of the signal along the Y and X directions is imposed with phase and frequency encoding by gradients G_y and G_x. The G_y gradient phase encodes the signal by applying gradient in B parallel to B_0 but varying along Y for a time-duration T_{pe} changing the resonance frequencies linearly along the Y axis according to $\omega(y) = \gamma(B_0 + yG_y)$. After the G_y gradient ends the resonance frequencies all return to the previous resonance frequency ω but the relative phase of magnetization now varies linearly along the Y axis phase (□) encoding the

signal according to □(y) = -γ y $G_y T_{pe}$. The G_x gradient turns on to frequency encode the signal by changing the resonance frequencies linearly along the X axis according to ω(x) = γ(B_0 +xG_x). The gradient encoding along the X axis and phase encoding along the Y axis of signal frequencies form the frequency domain of the image known as k-space. The k-space frequency signals of the image are sampled with the MRI scanner by manipulating the gradients, RF-pulses to guide the scanner through k-space. The frequency signals are converted with an analog to digital converter (ADC) for digital recording. When sufficient frequencies of k-space are sampled and recorded the frequency signals are inverse Fourier transformed in two dimensions or three dimensions into image space creating the image.

The image acquisition can be in two dimensions or three dimensions. In the two-dimensional acquisition the B_1 RF pulse excites a narrow slab determining the Z position. In three dimensional imaging the B_1 RF pulse excites a wide slab and then a second G_z gradient is used to phase the spins to encode location on the Z axis. The choice of two- or three-dimensional acquisition depends on the imaging application.

Repeated G_y phase encoding gradients at different magnitude G_y and/or duration T_{pe} selectively encode the k-Y axis rows of k-space. The G_x gradient frequency encodes the k-X axis columns of k-space and the ADC receiver samples the magnitudes of frequencies at time intervals while the frequency encoding G_x gradient is turned on. The gradients are manipulated to sample k-space in patterns to collect data from sufficient phase and frequency signals to reconstruct the image.

The combination of RF pulses, gradients and receiver listening periods are collectively known as a pulse sequence. The pulse sequence specifies the timing, magnitude, duration and order of RF pulses, gradients and signal sampling (turning on the receiver). The timing between repetitions of the B_1 RF pulse is repetition time T_R and the time between the B_1 RF pulse and the peak signal of the echo is echo time T_E. Pulse sequences use differences in longitudinal T_1 relaxation times, transverse T_2 relaxation times and proton density of the tissues to create contrast that make tissues borders in the image visible and selectively highlight or suppress tissues types.

Time-of-flight magnetic resonance angiography

Time-of-flight (TOF) magnetic resonance angiography (MRA) pulse sequences have the ability to distinguish moving blood from immobile background tissues. MRA even takes advantage of arterial blood moving faster than venous blood to highlight arterial blood while suppressing venous blood [46]. MRA uses thick slab B_1 RF excitation pulses and three-dimensional data acquisition. MRA pulse sequences use repeated B_1 RF slab selection excitation pulses and gradient echoes with small tip angles spaced close together in time with short T_R and short T_E that saturates the excited tissues. The saturated background tissues are not able to recover their longitudinal magnetization [47, 48]. The blood within the excited volume is continuously replaced by fresh blood flowing into the volume. As a result, the blood does not experience the signal saturation and appears as bright tissue in the image. [40, 46, 49]. By keeping the T_R times very short TOF-MRA can even saturate and suppress signal from slower venous blood [50] leaving

fast moving arterial blood brightest [47]. Even the arterial walls will be dimmer than the moving blood [47]. Diseased arteries with low blood flow may also appear dim or not be visible at all [45]. Thus MRA is showing physiology and not just anatomy [49]. TOF-MRA images are not free of background tissues due to signal recovery by short T_1 tissues [48]. These background tissues may have intensities as high as the arterial blood [47] requiring extra image postprocessing steps to segment the arterial blood from these background tissues. The amplification of the flowing blood by the pulse sequence allows this procedure to be done without contrast, thereby increasing patient safety [34].

Filling a gap in research

Quantitative arterial tortuosity measurements are rarely used clinically. More research is needed to validate quantitative arterial tortuosity measurement for clinical use. Arterial tortuosity of only a limited numbers of vascular diseases has been studied. Arterial tortuosity due to tumors is a local phenomenon but it is not known if systemic vascular diseases such as hypertension correlate with increased arterial tortuosity in all or only limited arteries. Tortuosity measurements are needed for more arteries in more vascular diseased populations to build evidence for clinical use of quantitative tortuosity measurements.

One major obstacle to studying arterial tortuosity is the cost of imaging new subjects and corresponding negative controls. MRA images already exist for many subjects with vascular diseases. Studying the effects of vascular diseases on arterial

tortuosity in these existing images opens up a low cost and quick method to study the effects of many vascular diseases.

There are many challenges to studying arterial tortuosity using existing MRA images. The existing images from clinical scans and previous research studies were often acquired with different scanners and parameters, covering different arteries or parts of arteries at different resolutions. Corresponding negative controls are not collected for clinical scans. The challenges of correlating arterial tortuosity with vascular diseases in existing MRA are studied in three experimental papers submitted for publication in peer reviewed journals and duplicated here in Chapters 2, 3 and 4.

Tortuosity measurement and analysis system

The experiments to correlate arterial tortuosity with vascular diseases were conducted with an arterial tortuosity measurement and comparison system developed in the course of this research. The system included plugins to ImageJ [51], an image processing tool. The plugins handled image processing tasks such as filtering, segmenting, calculating the centerline and selecting arteries for tortuosity measurement. Arterial tortuosity measures were computed from centerline data compiled in the database and analyzed using the statistical environment, R [52]. The statistical analysis environment and relational database were also used to organize data by case and control group for comparison between groups. This system was used in all of the experimental papers.

Experimental papers

In Chapter 2 the first paper “Comparing Performance of Centerline Algorithms for Quantitative Assessment of Brain Vascular Anatomy” tackles the issues of generating centerlines for all arteries of interest. Centerlines are necessary for the tortuosity measurements. To measure tortuosity in a large range of different arteries, centerline algorithms must be able to consistently make centerlines that accurately represent the anatomy of the arteries. In this experiment different Dijkstra based centerline algorithms are compared for their ability to create accurate and stable centerlines in numeric phantoms of different shapes and in MRA brain images. One of the most challenging arteries to calculate centerlines for is the internal carotid artery (ICA) in the brain. Anatomically, the ICA has a looping structure where distant inferior (or upstream) and superior (or downstream) portions of the vessel are nearly adjacent. During segmentation of the ICA from the background, the adjacent portions of vessel are often erroneously connected, resulting in a shortcut or “kiss” which subsequently affects the centerline extraction. The study measures and selects a centerline algorithm that can draw centerlines around the difficult loop of the ICA without taking the kissing shortcut.

In Chapter 3 the paper “Validation of an Arterial Tortuosity Measure with Application to Hypertension” further refined the centerline algorithm and developed and tested a tortuosity measurement method. Tortuosity was measured by calculating DFM tortuosity curves rather than single DFM tortuosity measurements and tested the underlying DFM tortuosity measurement on numeric phantoms and on hypertensive and control populations. This paper deals with many of the challenges of reusing existing

image data. The images in this study truncated arteries at different points making direct comparison at the same end-points impossible. The study uses DFM tortuosity curves to compare truncated arteries. The study also has image data for the same subjects acquired at different resolutions making it possible to measure the effect of resolution on the DFM tortuosity metric and develop a strategy to reduce the resolution effect. The study also compares negative controls collected with different methodologies.

Hypertension was an interesting vascular disease for arterial tortuosity measurement. Hypertension had been correlated with increased tortuosity of brain matter arterioles from autopsy photomicrographs [27]. Large arteries observed in vivo with MRA images of living subjects have not been correlated with increased tortuosity before this study. The study included a set of hypertension data acquired at 7.0 T which is rare. The 7.0 T data set contained images of large diameter arteries like the ICA down to the small diameter lenticulostriate arteries not seen at lower field strength.

In Chapter 4 the paper “Medical Record and Imaging Evaluation To Identify Arterial Tortuosity Phenotype in Populations At Risk For Intracranial Aneurysms” examines the relationship between arterial tortuosity and intracranial aneurysms. In a previous study on the mechanisms of arterial and aneurysmal tortuosity, the elastin protein of extracted arteries was degraded *in vitro* weakening the arterial walls causing increased arterial tortuosity and aneurysmal dilations [1]. There were no previous studies on patients with intracranial aneurysms. This study looked for increased arterial tortuosity in populations with familial intracranial aneurysms, unaffected members of high intracranial aneurysm risk pedigrees and in other patients with intracranial aneurysms.

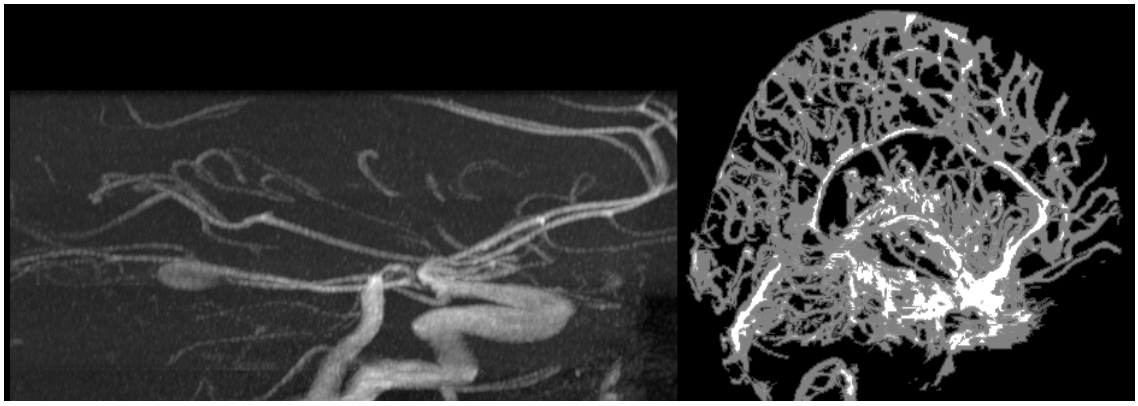

Figure 1.1.Arterial imaging modalitites. (Left) Maximum intensity projection (MIP) image of TOF-MRA image displays flowing arterial blood. (Right) Both veins and arteries appear in the computed tomography angiography (CTA) segmented blood vessel image making arteries difficult to distinguish.

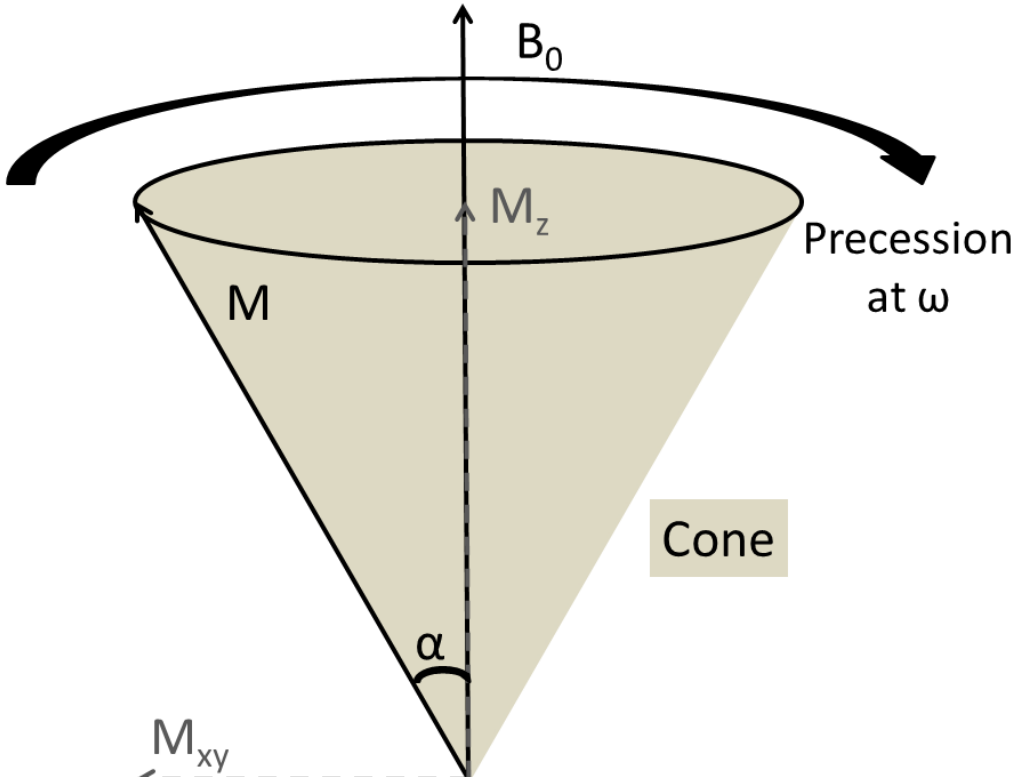

Figure 1.2. The bulk magnetization vector M precesses about the static magnetic field vector B_0 at resonance frequency ω with longitudinal component M_z and transverse component M_{xy} at tip angle α.

References

1. Dobrin PB, Schwarcz TH, Baker WH: **Mechanisms of arterial and aneurysmal tortuosity**. *Surgery* 1988, **104**:568-571.

2. **Unruptured intracranial aneurysms--risk of rupture and risks of surgical intervention. International Study of Unruptured Intracranial Aneurysms Investigators**. *N Engl J Med* 1998, **339**:1725-1733.

3. Gillespie DL, Villavicencio JL, Gallagher C, Chang A, Hamelink JK, Fiala LA, O'Donnell SD, Jackson MR, Pikoulis E, Rich NM: **Presentation and management of venous aneurysms**. *J Vasc Surg* 1997, **26**:845-852.

4. Capowski JJ, Kylstra JA, Freedman SF: **A numeric index based on spatial frequency for the tortuosity of retinal vessels and its application to plus disease in retinopathy of prematurity**. *Retina (Philadelphia, Pa.)* 1995, **15**:490-500.

5. Dougherty G, Johnson MJ, Wiers MD: **Measurement of retinal vascular tortuosity and its application to retinal pathologies**. *Med Biol Eng Comput* 2010, **48**:87-95.

6. Bullitt E, Reardon DA, Smith JK: **A review of micro- and macrovascular analyses in the assessment of tumor-associated vasculature as visualized by MR**. *Neuroimage* 2007, **37 Suppl 1**:S116-9.

7. Ritelli M, Drera B, Vicchio M, Puppini G, Biban P, Pilati M, Prioli MA, Barlati S, Colombi M: **Arterial tortuosity syndrome in two Italian paediatric patients**. *Orphanet J Rare Dis* 2009, **4**:20.

8. Loeys BL, Chen J, Neptune ER, Judge DP, Podowski M, Holm T, Meyers J, Leitch CC, Katsanis N, Sharifi N, Xu FL, Myers LA, Spevak PJ, Cameron DE, De Backer J, Hellemans J, Chen Y, Davis EC, Webb CL, Kress W, Coucke P, Rifkin DB, De Paepe AM, Dietz HC: **A syndrome of altered cardiovascular, craniofacial, neurocognitive and skeletal development caused by mutations in TGFBR1 or TGFBR2**. *Nat Genet* 2005, **37**:275-281.

9. Loeys BL, Schwarze U, Holm T, Callewaert BL, Thomas GH, Pannu H, De Backer JF, Oswald GL, Symoens S, Manouvrier S, Roberts AE, Faravelli F, Greco MA, Pyeritz RE, Milewicz DM, Coucke PJ, Cameron DE, Braverman AC, Byers PH, De Paepe AM, Dietz HC: **Aneurysm syndromes caused by mutations in the TGF-beta receptor**. *N Engl J Med* 2006, **355**:788-798.

10. Kono AK, Higashi M, Morisaki H, Morisaki T, Tsutsumi Y, Akutsu K, Naito H, Sugimura K: **High prevalence of vertebral artery tortuosity of Loeys-Dietz syndrome in comparison with Marfan syndrome**. *Jpn J Radiol* 2010, **28**:273-277.

11. Mizuguchi T, Collod-Beroud G, Akiyama T, Abifadel M, Harada N, Morisaki T, Allard D, Varret M, Claustres M, Morisaki H, Ihara M, Kinoshita A, Yoshiura K-ichiro, Junien C, Kajii T, Jondeau G, Ohta T, Kishino T, Furukawa Y, Nakamura Y, Niikawa N, Boileau C, Matsumoto N: **Heterozygous TGFBR2 mutations in Marfan syndrome**. *Nat Genet* 2004, **36**:855-860.

12. Choo JTL, Tan TH, Lai AHM, Wong KY: **Loeys-Dietz syndrome: a Marfan-like syndrome associated with aggressive vasculopathy**. *Singapore Med J* 2009, **50**:e353-357.

13. Dietz HC, Cutting GR, Pyeritz RE, Maslen CL, Sakai LY, Corson GM, Puffenberger EG, Hamosh A, Nanthakumar EJ, Curristin SM: **Marfan syndrome caused by a recurrent de novo missense mutation in the fibrillin gene**. *Nature* 1991, **352**:337-339.

14. Ramirez F, Dietz HC: **Marfan syndrome: from molecular pathogenesis to clinical treatment**. *Curr Opin Genet Dev* 2007, **17**:252-258.

15. Pereira L, Andrikopoulos K, Tian J, Lee SY, Keene DR, Ono R, Reinhardt DP, Sakai LY, Biery NJ, Bunton T, Dietz HC, Ramirez F: **Targetting of the gene encoding fibrillin-1 recapitulates the vascular aspect of Marfan syndrome**. *Nat Genet* 1997, **17**:218-222.

16. Rodrigues VJ, Elsayed S, Loeys BL, Dietz HC, Yousem DM: **Neuroradiologic manifestations of Loeys-Dietz syndrome type 1**. *AJNR Am J Neuroradiol* 2009, **30**:1614-1619.

17. Yetman AT, Beroukhim RS, Ivy DD, Manchester D: **Importance of the clinical recognition of Loeys-Dietz syndrome in the neonatal period**. *Pediatrics* 2007, **119**:e1199-1202.

18. Moody DM, Brown WR, Challa VR, Ghazi-Birry HS, Reboussin DM: **Cerebral microvascular alterations in aging, leukoaraiosis, and Alzheimer's disease**. *Ann N Y Acad Sci* 1997, **826**:103-116.

19. Alazzaz A, Thornton J, Aletich VA, Debrun GM, Ausman JI, Charbel F: **Intracranial percutaneous transluminal angioplasty for arteriosclerotic stenosis**. *Arch Neurol* 2000, **57**:1625-1630.

20. Bullitt E, Gerig G, Pizer SM, Lin W, Aylward SR: **Measuring tortuosity of the intracerebral vasculature from MRA images**. *IEEE Trans Med Imaging* 2003, **22**:1163-1171.

21. Lotmar W, Freiburghaus A, Bracher D: **Measurement of vessel tortuosity on fundus photographs**. *Albrecht Von Graefes Arch Klin Exp Ophthalmol* 1979, **211**:49-57.

22. Hart WE, Goldbaum M, Côté B, Kube P, Nelson MR: **Measurement and classification of retinal vascular tortuosity**. *Int J Med Inform* 1999, **53**:239-252.

23. O'Flynn PM, O'Sullivan G, Pandit AS: **Geometric variability of the abdominal aorta and its major peripheral branches**. *Ann Biomed Eng* 2010, **38**:824-840.

24. Dougherty G, Varro J: **A quantitative index for the measurement of the tortuosity of blood vessels**. *Med Eng Phys* 2000, **22**:567-574.

25. O'Flynn PM, O'Sullivan G, Pandit AS: **Methods for three-dimensional geometric characterization of the arterial vasculature**. *Ann Biomed Eng* 2007, **35**:1368-1381.

26. Bullitt E, Aylward SR, Van Dyke T, Lin W: **Computer-assisted measurement of vessel shape from 3T magnetic resonance angiography of mouse brain**. *Methods* 2007, **43**:29-34.

27. Hiroki M, Miyashita K, Oda M: **Tortuosity of the white matter medullary arterioles is related to the severity of hypertension**. *Cerebrovasc Dis* 2002, **13**:242-250.

28. Johnson MJ, Dougherty G: **Robust measures of three-dimensional vascular tortuosity based on the minimum curvature of approximating polynomial spline fits to the vessel mid-line**. *Med Eng Phys* 2007, **29**:677-90.

29. Bullitt E, Zeng D, Mortamet B, Ghosh A, Aylward SR, Lin W, Marks BL, Smith K: **The effects of healthy aging on intracerebral blood vessels visualized by magnetic resonance angiography**. *Neurobiol Aging* 2010, **31**:290-300.

30. Bullitt E, Rahman FN, Smith JK, Kim E, Zeng D, Katz LM, Marks BL: **The effect of exercise on the cerebral vasculature of healthy aged subjects as visualized by MR angiography**. *AJNR Am J Neuroradiol* 2009.

31. Kagan A, Aurell E, Tibblin G: **Signs in the fundus oculi and arterial hypertension: unconventional assessment and significance**. *Bull World Health Organ* 1967, **36**:231-241.

32. Spangler KM, Challa VR, Moody DM, Bell MA: **Arteriolar tortuosity of the white matter in aging and hypertension. A microradiographic study**. *J Neuropathol Exp Neurol* 1994, **53**:22-26.

33. Bui BT, Miller S, Mildenberger P, Sam A 2nd, Sheng R: **Comparison of contrast-enhanced MR angiography to intraarterial digital subtraction angiography for evaluation of peripheral arterial occlusive disease: results of a phase III multicenter trial**. *J Magn Reson Imaging* 2010, **31**:1402-1410.

34. Miyazaki M, Lee VS: **Nonenhanced MR angiography**. *Radiology* 2008, **248**:20-43.

35. *National Research Council committee to assess health risks from exposure to low level of ionizing radiation: BEIR VII, Phase 2*. Washington, DC: National Academies Press; 2006.

36. Griffey RT, Sodickson A: **Cumulative radiation exposure and cancer risk estimates in emergency department patients undergoing repeat or multiple CT**. *AJR Am J Roentgenol* 2009, **192**:887-892.

37. Sodickson A, Baeyens PF, Andriole KP, Prevedello LM, Nawfel RD, Hanson R, Khorasani R: **Recurrent CT, cumulative radiation exposure, and associated radiation-induced cancer risks from CT of adults**. *Radiology* 2009, **251**:175-184.

38. Huang B, Law MW-M, Khong P-L: **Whole-body PET/CT scanning: estimation of radiation dose and cancer risk**. *Radiology* 2009, **251**:166-174.

39. Liang Z-P, Lauterbur PC: *Principles of Magnetic Resonance Imaging: A Signal Processing Perspective*. 1st edition. Wiley-IEEE Press; 1999.

40. Laub GA, Kaiser WA: **MR angiography with gradient motion refocusing**. *J Comput Assist Tomogr* 1988, **12**:377-382.

41. Prince JL, Links J: *Medical Imaging Signals and Systems*. 1st edition. Prentice Hall; 2005.

42. Kang C-K, Park C-W, Han J-Y, Kim S-H, Park C-A, Kim K-N, Hong S-M, Kim Y-B, Lee KH, Cho Z-H: **Imaging and analysis of lenticulostriate arteries using 7.0-Tesla magnetic resonance angiography**. *Magn Reson Med* 2009, **61**:136-144.

43. Cho Z-H, Kang C-K, Han J-Y, Kim S-H, Kim K-N, Hong S-M, Park C-W, Kim Y-B: **Observation of the lenticulostriate arteries in the human brain in vivo using 7.0T MR angiography**. *Stroke* 2008, **39**:1604-1606.

44. Kang C-K, Park C-A, Park C-W, Lee Y-B, Cho Z-H, Kim Y-B: **Lenticulostriate arteries in chronic stroke patients visualised by 7□T magnetic resonance angiography**. *Int J Stroke* 2010, **5**:374-380.

45. Hendrix LE, Strandt JA, Daniels DL, Mark LP, Borne JA, Czervionke LF, Haughton VM, Williams AL: **Three-dimensional time-of-flight MR angiography with a surface coil: evaluation in 12 subjects**. *AJR Am J Roentgenol* 1992, **159**:103-106.

46. Axel L: **Blood flow effects in magnetic resonance imaging**. *AJR Am J Roentgenol* 1984, **143**:1157-1166.

47. Suri JS, Liu K, Reden L, Laxminarayan S: **A review on MR vascular image processing algorithms: acquisition and prefiltering: part I**. *IEEE Trans Inf Technol Biomed* 2002, **6**:324-337.

48. Singer JR, Crooks LE: **Nuclear magnetic resonance blood flow measurements in the human brain**. *Science* 1983, **221**:654-656.

49. Bosmans H, Wilms G, Dymarkowski S, Marchal G: **Basic principles of MRA**. *Eur J Radiol* 2001, **38**:2-9.

50. Liauw L, van Buchem MA, Spilt A, de Bruïne FT, van den Berg R, Hermans J, Wasser MN: **MR angiography of the intracranial venous system**. *Radiology* 2000, **214**:678-682.

51. **ImageJ, U.S. National Institutes of Health, Bethesda, Maryland, USA** [http://rsb.info.nih.gov/ij/].

52. **R: A language and environment for statistical computing. R Foundation for Statistical Computing, Vienna, Austria. ISBN 3-900051-07-0** [http://www.R-project.org/].

CHAPTER 2

COMPARING PERFORMANCE OF CENTERLINE ALGORITHMS FOR QUANTITATIVE ASSESSMENT OF BRAIN VASCULAR ANATOMY

Karl T. Diedrich[1], John A. Roberts[1], Richard H. Schmidt[2] and Dennis L. Parker[1]

[1]Utah Center for Advanced Imaging Research, Department of Radiology, University of Utah, 729 Arapeen Drive, Salt Lake City, UT 84108, USA

[2]Department of Neurosurgery, University of Utah, Health Science Center, Bldg 550, 5th Floor, 175 N. Medical Drive East, Salt Lake City, UT 84132, USA

Grant sponsors: NLM Grants: T15LM007124, and 1R01 HL48223, and the Ben B. and Iris M. Margolis Foundation.

* Correspondence to: Karl T. Diedrich, Department of Radiology, University of Utah, 729 Arapeen Drive, Salt Lake City, UT 84108, USA. E-mail: Karl.Diedrich@utah.edu Tel.: 1-801-581-3141. Fax: 1-801-585-3592

Abstract

Attributes like length, diameter and tortuosity of tubular anatomical structures such as blood vessels seen in medical images can be measured from centerlines. This study develops methods for comparing the performance of centerline algorithms. Several centerline algorithms exist but there are challenges to calculating centerlines. The starting point of a vascular tree can affect calculated centerlines. Vessels can loop back touching or kissing themselves causing problems for centerline algorithms. This study develops methods for evaluating the accuracy and stability of centerline algorithms.

Images of human brain arteries were acquired with time of flight (TOF)–magnetic resonance angiography (MRA) and the arteries were segmented. Dijktra's shortest paths based centerline algorithms were developed with different cost functions. The cost functions were the inverse modified distance from edge ($MDFE_i$) of the segmentation, the center of mass (COM) of the segmentation, the binary thinned (BT)-$MDFE_i$ and the BT-COM. The algorithms generated centerlines trees of simulated numeric vasculature phantoms and of segmented brain arteries. The accuracy of the centerline algorithms were measured by the Root Mean Square Error from known centerlines of electronic phantoms. The stability of the centerlines was measured by starting the centerline tree from multiple points and measuring the differences between the centerline trees. The accuracy and stability of the centerlines were visualized by overlaying centerlines on the

vasculature images. The visualization was used to assess algorithm performance on a kissing vessel in human brain arteries.

The BT-COM cost function centerline was the most stable in numeric phantoms and human brain arteries. The $MDFE_i$ based centerline was most accurate in the numeric phantoms. The COM based centerline handled the kissing artery in the human brain in 16 out of 16 cases whereas the BT-COM was correct in 10 out of 16 and $MDFE_i$ was correct in 6 out 16.

The COM based centerline algorithm handled the kissing arteries of the brain images and will be used for quantitative assessment of vascular morphology in later studies. The highest stability did not correspond with the highest accuracy in numeric phantoms. The highest stability and accuracy in numeric phantoms also did not correspond to the best centerlines in subject data. The centerline visualization methods were critical for assessing centerlines in subject data.

Key words: Centerline, MRA, stability, vascular.

Introduction

Vascular diseases can be diagnosed and characterized by abnormalities in blood vessel morphology observed with three-dimensional medical imaging techniques such as magnetic resonance angiography (MRA). An example of this includes the correlation of the severity of hypertension with tortuosity or twistedness of arteries (Hiroki et al., 2002). Currently, nearly all medical evaluation of 3D images is performed qualitatively by visual assessment by specialists. Quantitative assessment of vessel morphology including

radius, length and tortuosity (twistedness) measurements by computer software would make comparison of measurements across medical centers, tracking changes over time, and automated screening for vascular disease possible. Quantitative assessment of artery morphology can be made from centerlines of arteries (O'Flynn et al., 2007; Lesage et al., 2009). Arterial centerlines have also been used to measure the tortuosity of blood vessels (Bullitt et al., 2003). Centerlines can be used to measure artery lengths and radius. Change of radius in arterial centerlines can potentially detect stenoses and aneurysms (Frangi et al., 1999; Kang et al., 2009; Lesage et al., 2009). Centerlines can be used for many tasks involving the quantitative analysis of blood vessels.

Stable and accurate centerline algorithms are needed to quantitatively measure and investigate the blood vessels and the effects of disease on blood vessels. Stability of the centerline is the ability of an algorithm to create the same centerline for the same image data with different input parameters, primarily the starting point of the centerline tree. Accuracy refers to how close a calculated centerline is to an ideal centerline for a numeric phantom. Centerline accuracy and stability measurement methods are needed to select the best algorithms for generating centerlines for a quantitative task. Accuracy and stability visualization methods are needed to know where centerlines are accurate or inaccurate, stable or unstable. Different studies will have different areas of interest; the researcher will want to know if the centerline is accurate and stable in the area of interest. For example intracranial aneurysms typically occur in the circle of Willis arteries, which experience higher blood pressure and pressure variations than the peripheral intracranial arteries (Arimura et al., 2004). Thus, for the purpose of aneurysm detection, it is more

important that the circle of Willis arterial centerlines are stable whereas the stability of the peripheral arterial centerlines is less important to aneurysm assessment.

The purpose of this study is to develop methods for measuring and visualizing the accuracy and stability of centerline algorithms and select the best available algorithm for creating centerlines in central arteries of human brain MRA images. Arterial centerlines have the potential for developing diagnostic and descriptive measures of vascular diseases. The methods developed here may also be used to quantify tubular structures in any three-dimensional image.

Materials and methods

Source images

In this study we collected images: a computer generated helical and straight line phantom (Fig. 2.1 A, B), two computer generated branching phantoms with background noise from Aylward (Aylward and Bullitt, 2002) (Fig. 2.2 A, B) and eight human brain Time of Flight (TOF)-MRA images (Fig. 2.3). The helical phantom was generated by calculating points on a helical and straight lines then rolling a ball with a 6 voxel radius along the points. The eight MRA image data sets were selected from our ongoing intracranial aneurysm study approved by the University of Utah Institutional Review Board. Additional information on the data set is in the Source Images supplement section.

Tools

Image processing tools for this study were developed in Java with the ImageJ toolkit (Rasband, 1997; Burger and Burge, 2007). Results were stored in the MySQL database (available at http://www.mysql.com/). Graphing results and statistical analysis were performed with R (R Development Core Team, 2009) .

Segmentation

The unsegmented computer generated branching phantoms and the eight human brain MRA images were segmented from the background noise and brain tissue leaving the simulated arterial tissue (Fig. 2. 4 A, B) or the human brain arterial tissue (Fig. 2.5) with a z-buffer segmentation (ZBS) algorithm (Parker et al., 2000; Chapman et al., 2004). The point where the three branches of the branching phantoms meet is narrow so that the region growing threshold employed during the ZBS segmentation had to be lowered in order to keep the segmented branches all in one connected component (Fig. 2.4 B). Additional details of the segmentation process are covered in the Segmentation supplement section. The result of segmentation is the extracted arterial tree.

Cost function segmentation preprocessing

To generate a centerline through the segmented arteries a cost was assigned to every voxel (a three-dimensional pixel) in the extracted arterial tree. Four different costs functions were: $MDFE_i$, COM, BT-COM and BT-$MDFE_i$.

The $MDFE_i$ cost function calculates a value for each voxel that is higher for voxels closer to the edge of the arteries and lower for voxels closer to the middle of the arteries by first calculating the distance from edge (DFE), modifying the DFE (MDFE) to break ties and inverting to make the costs higher on the outside and lower on the inside (Zhang et al., 2005) (Fig. 2.6).

The center of mass cost function loops through every voxel in the segmentation and calculates the average X, Y and Z positions of each voxel and up to 26 three-dimensional neighbors as the center of mass, recording each voxel's center of mass and cumulative distance moved from the original position to each subsequent center of mass through multiple iterations. At each iteration, the center of mass calculation depends on the positions of the previous iteration. The center of mass calculation is repeated until all voxels have been moved a minimum of 30 times. Increasing iterations increased stability only minimally after 30 iterations. The cumulative distances moved are divided by the minimum nonzero distance moved in the entire segmentation and the result is cubed. Voxels at the segmentation edge begin moving with the earliest iterations and tend to move the farthest, generating high cost scores. Voxels near the center move with later iterations and for short distances, generating low cost scores (Fig. 2.7).

The BT centerline algorithm (Homman, 2007) eroded the segmentations to single voxel-width skeletons (Fig. 2.8 A, B and Fig. 2.9). The brain artery skeletons are close to centerlines but have short segments running across wide arteries (Fig. 2.9). The skeletons were used as inputs into the $MDFE_i$ or COM cost functions to utilize the existing software program developed for the inverse MDFE and COM centerlines. The DFE will

always be one for every voxel and not change the skeleton. The voxels will typically only have 1, 2 or 3 neighbors in the COM reducing the amount of movement compared to the earlier algorithms.

The result of preprocessing are cost values for every voxel in the extracted arterial tree. The costs will be higher at the edge and lower in the middle. The binary thinned arteries will only have one cost value. The centerline of the arteries will be the lowest cost path through the cost function.

Centerline algorithms

To calculate the centerline the precomputed arterial tree costs were input into the Dijkstra shortest paths algorithm (Dijkstra, 1959). Dijkstra's algorithm calculated the lowest cost centerlines from every voxel back to a selected starting root voxel. Then the paths less than 30 voxels long were removed leaving a skeleton centerline of the arterial tree (Zhang et al., 2005). The root of the $MDFE_i$ based centerline trees was the maximum MDFE, the thickest point in the arterial tree (Zhang et al., 2005). The root of the BT-$MDFE_i$ based centerline tree was the most central voxel in the arterial tree. The root of the COM based centerline tree and binary thinning-center of mass (BT-COM) based centerline trees are voxels with the lowest center of mass score. In the event of tied starting root points the root closest to the center of the image was selected. The centerlines tend toward the lower cost middle voxels of the preprocessed segmentations (Fig. 2.10 A, B). Shortest paths centerline generation on the binary thinned input has the effect of pruning off short branches that are running across artery widths (Fig. 2.11). The

results of the centerline algorithms were single voxel width centerline skeletons of the arterial trees.

Stability measure

Stability of the centerline was measured by generating the centerlines for the same segmentation starting at different root points. The first centerline tree is initiated from the root as described for the centerline algorithms. The arterial tree endpoints of the largest connected centerline tree were used as roots for a second round of centerlines. Smaller centerline trees of segmented arteries not connected to the largest section were discarded.

To measure and identify stable and unstable centerlines, the first round and all second round centerlines were accumulated in one image. The most stable centerline points occur in the same voxel for all N centerline root points. The stability measure for an image was the percentage of centerline voxels in the accumulated image called centerline for all of the centerline roots.

To visualize the accumulated centerlines the inverse of the accumulation was plotted in 3-D with the surrounding segmentation. This makes unstable voxels that are called centerline by fewer than N roots brighter than their neighbors and therefore easily visible (Fig. 2.12 left column).

Accuracy

Accuracy of the centerlines of the phantoms is measured by the root mean square error (RMSE) of Euclidean distances from the algorithm generated centerline points to the nearest known centerline point for a phantom. The centerline points used to generate the helix line phantom were known. The known centerline points for the helix line phantom were sparse (Fig. 2.1B); the algorithm-derived centerlines had more points because the centerlines extend out to last voxel at the end while the known center points used to generate the phantom stop at one radius distance from the edge of the phantom as seen in Fig. 2.1B. Therefore, the RMSE was computed only over the set of known points and their nearest centerline determined neighbors. Aylward and Bullitt (Aylward and Bullitt, 2002) provided ideal subvoxel accuracy positive control centerline coordinates, available in a text file, for the branching phantoms with noise. The RMSE of these phantoms was calculated between each centerline point determined by the Dijkstra algorithm and the closest subvoxel positive control point. The accuracy of the helix line phantom was visualized by plotting each algorithm centerline coordinate in red accumulating for each starting root and plotting the positive centerline control points in green. The red and green color together made yellow showing where the algorithm and positive control points were the same and where they differed (Fig. 2.12 right column).

Results

Phantom centerline stability and accuracy

The centerline tree of first helix line phantom (Fig. 2.1B) had seven ends. The first starting point in the thickest point of the phantom followed by starting points at the seven ends made total of eight centerline trees for the stability analysis. In this case, the inverse $MDFE_i$ cost function was the least stable with the lowest stability score (Table 2.1). Instability occurred throughout the helix at bifurcations and at line ends (Figure 2.12 A). The binary thinning skeleton only left one possible highly stable centerline with some instability occurring at ends when the skeleton was passed to either the inverse $MDFE_i$ or COM programs. The COM based centerline was more stable (higher stability score) than the inverse $MDFE_i$ based centerline (Table 2.1).

The $MDFE_i$ cost function was the most accurate (lowest RMSE) despite being the most unstable (lowest stability score) (Table 2.1). The accuracy visualization shows the positive control green, algorithm red and overlapping yellow centerlines (Fig. 2.12 right column). The inaccuracies occur at ends and bifurcations and in the helix portion of the phantom. The locations of the inaccuracies are similar to the locations of instability (Fig. 2.12). The COM based centerline lost more accuracy than the other algorithms bending around bifurcations as seen by the green color in Fig. 2.12 D. The binary thinning algorithms were frequently a few voxels off as seen by the green in the helix (Fig. 2.12 F, H) accounting for the high RMSE of accuracy.

Stability and accuracy on phantoms with noise

The $MDFE_i$ based centerline algorithm had the lowest stability and best accuracy (lower RMSE) for the lower SD 10 noise phantom. For the higher SD 20 noise phantom the COM and binary thinning paired with COM had lower RMSE. Binary thinning followed by the COM based algorithm consistently outperformed binary thinning followed by the $MDFE_i$ based algorithm with higher stability scores and lower RMSE of accuracy. Therefore the rest of the trials on MRA data used the binary thinning followed only by the COM based algorithm for centerline generation. The number of primary (one) plus secondary starting root points was three for most algorithms and four for the binary thinning followed by the COM based algorithm because the initial start point for the first round centerline was near an end of the branching object for the tests with three starting roots. The binary thinning followed by COM had the highest stability besides having the extra centerline tree (Table 2.2). The bright end of the lower right branch in Fig. 2.13 B shows that much of COM based algorithm instability happens at the end of the branch because one of the starting roots occurred here, shortening the centerline. When the centerline was rooted at another branch end the centerline extended longer at this branch end. This was an example of how the starting point alters the centerline tree.

Artery centerline stability

The running time for calculating COM costs for arterial trees was under 60 seconds for a total time of 3 to 5 minutes to generate the centerlines for all the centerline algorithms. Stability images from the segmentation are shown in Fig. 2.14. A region of

instability was seen in the left internal carotid artery in Fig. 2.14 A. In the vessel segmentation, the internal carotid artery siphon frequently loops back and touches itself creating a shortcut for the centerline to pass through. The $MDFE_i$ based centerlines pass through the kissing point (Fig. 2.15 A and Fig. 2.16 B). Dijkstra's shortest paths on the segmentation cost functions of the $MDFE_i$ and COM based algorithms produce only nonlooping branches. In the $MDFE_i$ based algorithm, the first centerline passes through the kissing point and subsequently two centerlines extend out from the kissing point to end on the distant edges of the siphon arterial wall (Fig. 2.14 A and B and Fig. 2.16 B). The COM based algorithm produced high scores near the kissing point, even though the scores in the kissing point are low (Fig. 2.15 B), causing the first centerline to run around the siphon loop (Fig. 2.14 C, D and Fig. 2.16 B). Shorter centerlines are subsequently generated by Dijkstra's algorithm (Dijkstra, 1959) from the kissing point to end at the longer centerline. However, these shorter centerlines fall below the 30 voxel length threshold and are removed leaving the final centerline tree (Fig. 2.16 B). The BT-COM based centerline consistently forms a loop with one part of the centerline passing through the narrow kissing point (Fig. 2.14 E, F and Fig. 2.16 C). Failing to pass a centerline through the internal carotid artery (ICA) siphon loop is a common centerline failure and is used as a measure of centerline accuracy in the MRI images since there is no gold standard centerline for computing the RMSE as with the earlier phantoms.

As with the phantoms the COM and BT-COM based centerline had higher stability than the $MDFE_i$ based centerlines. We recorded when the centerline succeeded and failed to pass through the ICA siphon (Table 2.3). Success meant that the centerline

passed through the ICA without touching the edge of the segmentation for all roots; any failure of one tree was counted as a failure. The $MDFE_i$ based centerline would frequently pass through the ICA siphon correctly for some starting root locations but not others leading to its lower mean stability measure.

A one-way analysis of variance (ANOVA), using the *lm* command from R (R Development Core Team, 2009), of the centerline accuracy in the 16 ICA siphons by algorithm ($MDFE_i$, COM, BT-COM) showed a significant difference p-value = 3.62e-04. The COM was significantly more accurate than BT-COM, p-value = 1.26e-02. BT-COM was more accurate than $MDFE_i$ but not significantly different, p-value = 9.01e-02.

One-way ANOVA showed the algorithm significantly affects the stability, p-value = 1.63e-06. As the centerline stability box and whiskers plot shows the BT-COM based algorithm and COM algorithm are very close in stability, p-value = 0.846 indicating no significant difference. The $MDFE_i$ algorithm produces a significantly less stable centerline than the BT-COM based algorithm, p-value < 0.0001 (Fig. 2.17 A and Table 2.4).

The first run of different centerline algorithms can produce differing numbers of tree ends for roots of following centerline trees generated to measure stability. More ends and more centerline trees create more opportunity for instability. The centerline algorithms did not produce significantly different numbers of tree ends (p-value = 0.862). The number of tree ends used as roots does not account for the instability of the $MDFE_i$ centerline algorithm as seen in Fig. 2.17 B and Table 2.4. Table 2.4 summarizes the centerline stability data by algorithm recorded in Table 2.5.

Discussion

Our study showed the COM based centerline algorithm was more stable and correctly calculated more centerlines around the kissing ICA loops than the other algorithms tested using the newly developed centerline stability measure and visualization of ICA loop centerline. The stability measurement strategy demonstrated the consistency of the COM based centerline algorithm in the kissing ICA loops. The stability measurement strategy of starting the centerline tree at different points can be reused to test other centerline algorithms for use on any tubular structure. The stability, and phantom accuracy, visualization methods developed here identified where inaccuracy and instability were occurring. These methods are also usable for a wide range of centerline algorithms and applications of centerlines to anatomical studies.

This study is a first attempt to address the problem of kissing vessels. Kissing blood vessels are common in the segmentations of the brain and other anatomy. The method of having the centerline follow the middle of the mass of the artery solved the kissing vessel problem in the ICA loop in this study. Using mass in the centerline algorithm will be useful in any anatomical case where the true anatomical centerline is in the largest mass and noise creates smaller adjacent structures to the vessel.

The measure of stability from multiple starting points was able to determine the COM based algorithm handled the ICA kissing siphon from all starting ends ensuring the stability of the algorithm. It would be computationally impractical to test stability by starting the stability measure from every point in the segmentation or even from every point in the first centerline tree. By starting the centerline trees from all ends of the first

centerline tree the centerline algorithm will approach the regions of instability such as kissing ICA loop and all bifurcations from all directions thus testing the algorithm from all directions. The visualization of stability and accuracy allowed us to see that the instabilities and inaccuracies are mainly occurring at kissing vessel points and bifurcations.

The COM based centerline algorithm generates correct centerlines in cases where the artery is much larger than the kissing points and is resistant to adjacent segmentation noise as long as the noise is smaller than the artery. The COM based centerline gravitates toward the center of the largest mass and in the case of the ICA siphon the largest mass is in the loop and kissing section is smaller contributing less to the center of the mass.

All the cost functions had inaccuracies in the loop of the helix. The curve of the helix in the phantom is approximated to the nearest voxel and the centerline algorithms also have to approximate voxel positions causing the inaccuracies and instability frequently seen in curving centerlines. Curved centerlines often have a stair-stepped appearance. Some applications of the centerline may require subvoxel smoothing of the centerline to obtain smooth curves.

A limitation of comparing centerline algorithms by stability is that the most accurate centerline algorithm was not always the most stable algorithm. The BT algorithm was inherently stable because it erodes the segmentation from all outside points simultaneously to a single skeleton line. The BT cost functions, paired with $MDFE_i$ or COM, had consistently high stability while not having the highest accuracy in the phantom or in the count of correct ICA siphon centerlines in the brain images. The BT

algorithm removed most voxels of the segmentation in the skeletonization step leaving a limited path for the centerline generation from the skeleton allowing the BT algorithms to maintain high stability.

Highest stability also did not correspond to highest accuracy in the no noise and low noise phantoms where the $MDFE_i$ based algorithm was least stable but most accurate. In the brain images the COM based algorithm was clearly most accurate in the ICA siphon and was not significantly less stable than the most stable BT-COM based algorithm, while having the lowest stability in all phantoms and brain images the $MDFE_i$ based centerlines were the most accurate in the no added noise helix line phantom (Figure 2.1 A, B) and low SD 10 noise (Figure 2.2 A) phantoms. The RMSE of accuracy of the $MDFE_i$ centerlines increased from 0.393 in the SD 10 noise phantom to 0.674 in the SD 20 noise phantom (Table 2.2), a greater increase than the other more stable COM, BT-$MDFE_i$ and BT-COM based algorithms. It makes sense that the least stable centerline would lose accuracy the fastest as noise increases. As noise increases the stability of the algorithm becomes increasingly important to maintaining accuracy. The $MDFE_i$ based centerlines were the least accurate in the ICA siphons of the brain images that contain the noise of the MRI.

The current study tested a limited number of centerline algorithms both internally and externally developed. The stability measure and visualization of inverse stability are usable by researchers testing algorithms for particular centerline extraction applications of tubular anatomy. There may not be an ultimate singular centerline algorithm suitable for all applications. The COM based algorithm which was best in this study for extracting

the ICA siphon loop is prone to missing small dim arteries near larger brighter arteries. An application looking at a small dim artery would have to use another algorithm making the availability of comparison methods important. Tubular structures occur frequently in anatomy. In addition to the arteries studied here other anatomical structures studied with centerlines include veins, lung bronchioles, large and small intestine, nerves, bones and any other tubular anatomical structures.

Conclusion

Centerlines can be used to measure features of tubular anatomical structures. This study expands the range of structures that can have a centerline calculated. The kissing ICA siphon loops could not have a centerline made with the existing $MDFE_i$ (Zhang et al., 2005) and BT (Homman, 2007) algorithms. The COM algorithm developed here made a centerline possible in the ICA siphon loop. The centerline stability measure showed that the COM algorithm handled the kissing ICA siphon starting from any direction showing that the COM algorithm is stable in this case. The stability measure can be reused to test centerline algorithms when evaluating centerline algorithms for other tubular anatomical structures.

Acknowledgements

We greatly appreciate the help of the staff at the Utah Center for Advanced Imaging Research in supporting this research.

The branching phantoms used in this paper were generated and made available by the CASILab at The University of North Carolina at Chapel Hill and were distributed by the MIDAS Data Server at Kitware, Inc.

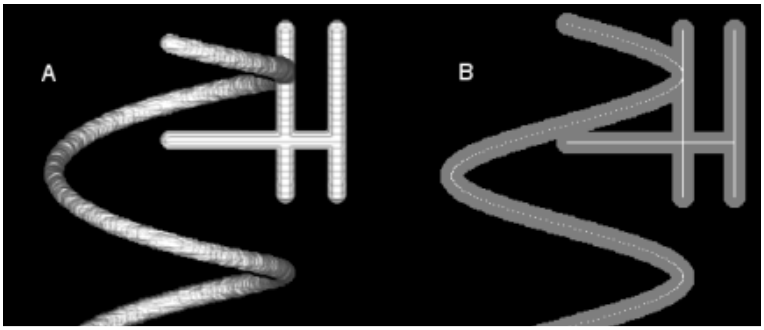

Figure 2.1. Electronic phantoms. (A) Shaded surface rendering of phantom. (B) Maximum intensity projection of phantom with centerline points used to generate the phantom.

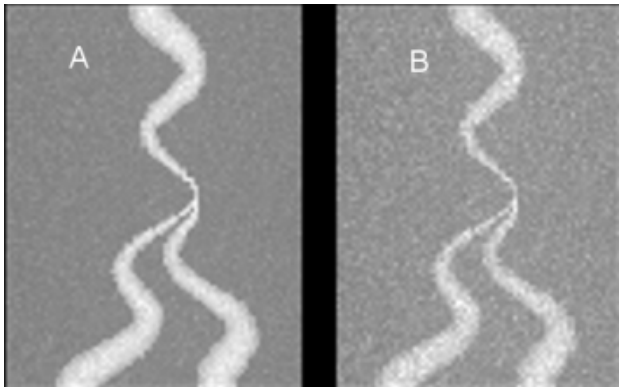

Figure 2.2. Aylward phantoms with background intensity 100 and tubular objects with cross-sectional intensities in a parabolic profile ranging from 150 at the edge to 200 at the middle of the object with increasing Gaussian noise. (A) Phantom with Standard Deviation (SD) 10 noise added. (B) Phantom with SD 20 noise added.

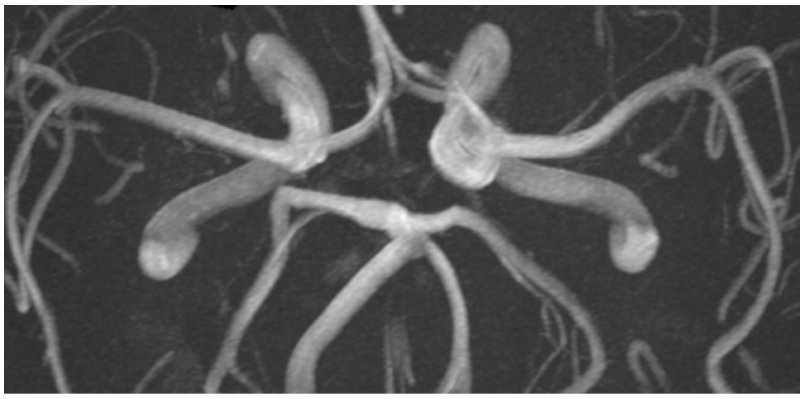

Figure 2.3. Magnetic resonance angiography (MRA) images of patient from 3 T MRI scanner viewed from the top with background brain tissue.

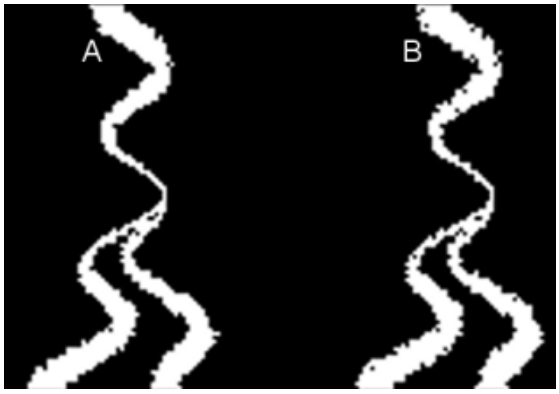

Figure 2.4. MIP projects of the segmented computer generated branching phantoms. (A) SD 10 segmentation with the seed histogram region growing threshold set at 0.15. (B) SD 20 segmentation with the seed histogram region growing threshold set at 0.13.

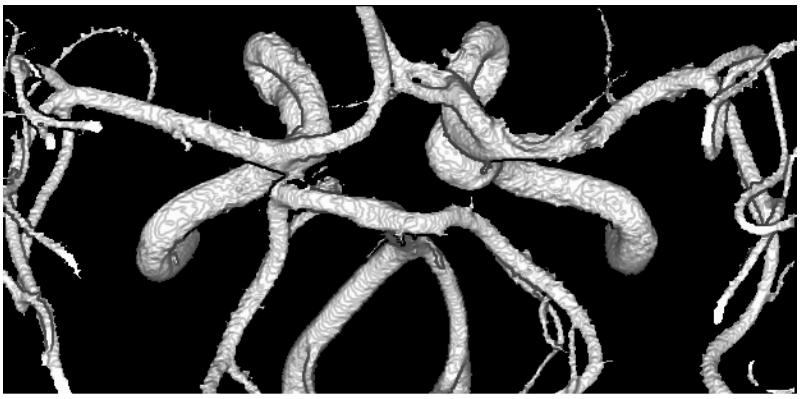

Figure 2.5. Segmented arteries shaded surface depth image shows the segmentation in 3D.

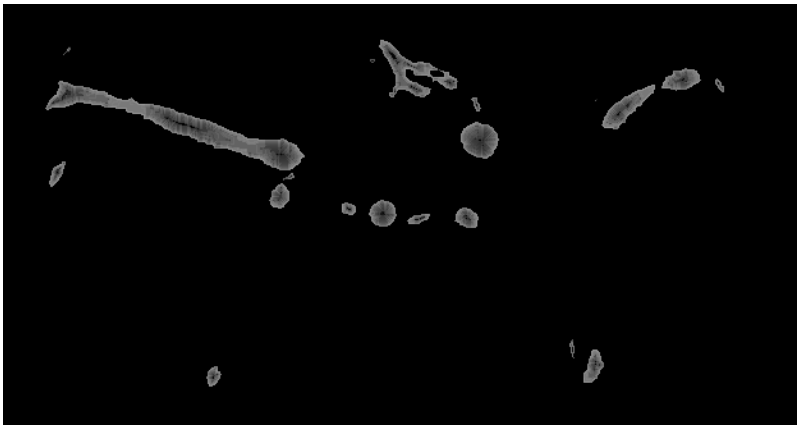

Figure 2.6. Brain artery segmentation inverse Modifed Distance From Edge ($MDFE_i$) cost function score cross section. Brighter is higher cost, darker is lower cost.

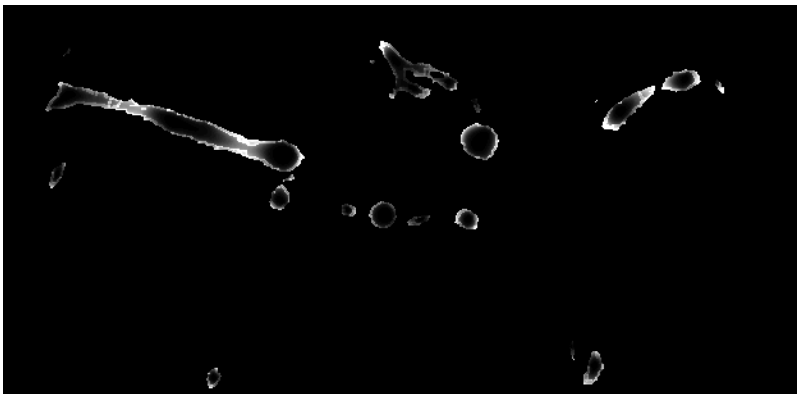

Figure 2.7. Brain artery segmentation Center Of Mass (COM) cost function score cross section. Brighter is higher cost, darker is lower cost.

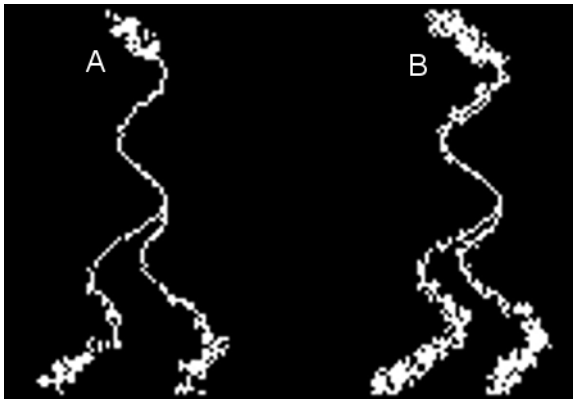

Figure 2.8. Binary thinned phantoms. (A) SD 10 binary thinned skeleton. (B) SD 20 binary thinned skeleton.

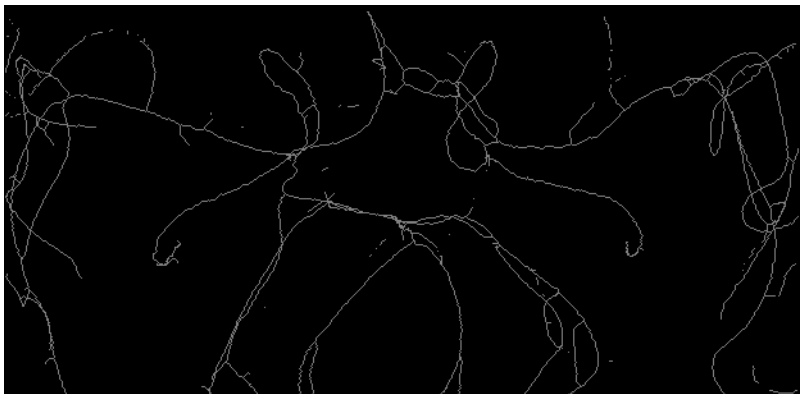

Figure 2.9. Maximum intensity transverse projection of binary thinned arteries. Binary thinning of segmented artery data produces a skeleton of the segmentation with lines running frequently across the arteries.

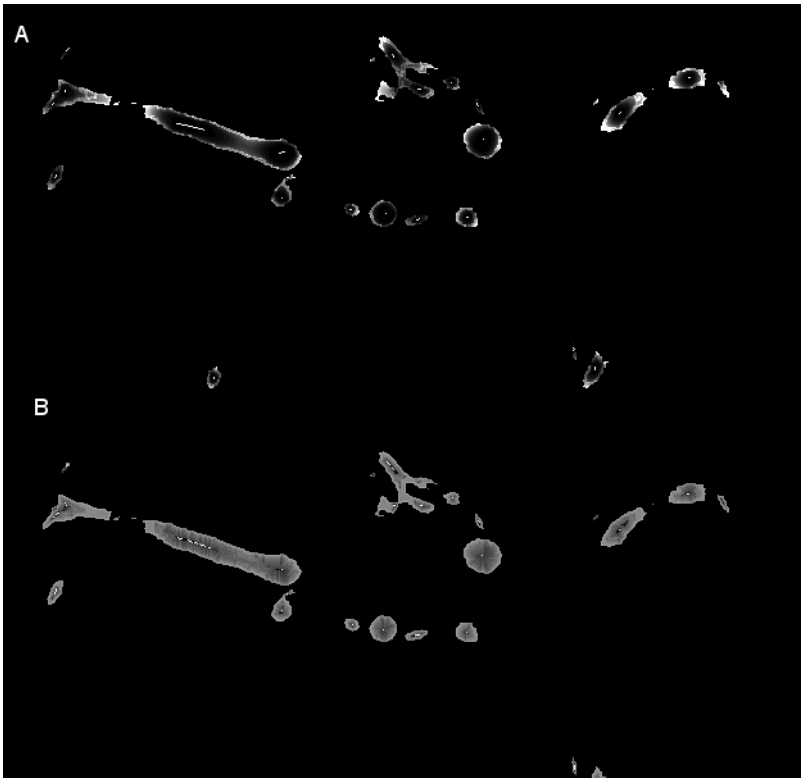

Figure 2.10. Cross sections of centerlines in artery segmentation cost functions. The centerlines line in the low cost darker middles of the segmented arteries. (A) COM cost function. (B) $MDFE_i$ cost function.

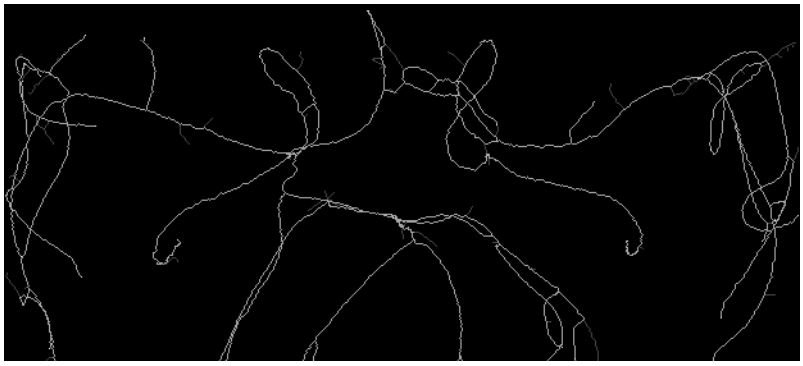

Figure 2.11. Maximum intensity transverse projection of binary thinned arteries. The skeleton is turned into a centerline by processing the skeleton with Dijkstra's shortest paths algorithm and removing lines less than 30 voxels long. The final centerline is shown bright with the removed short lines shown in the dim segmentation background intensity.

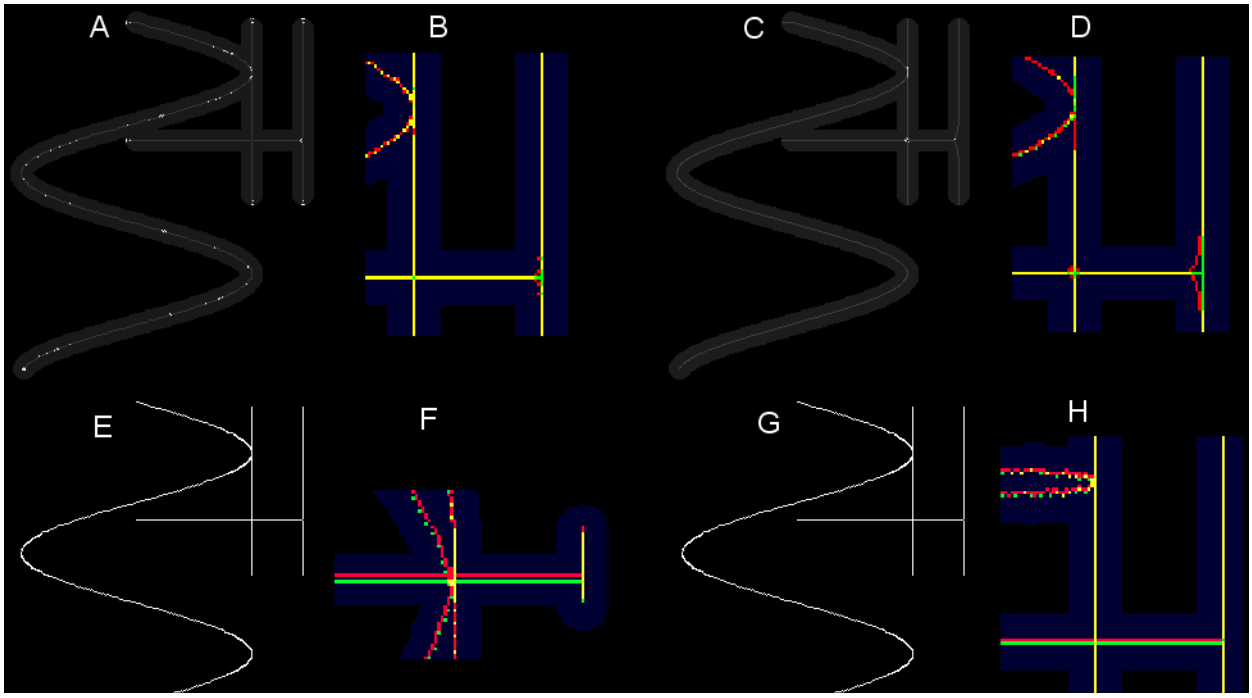

Figure 2.12. Phantom stability and accuracy (A-H) Phantom stability and accuracy visualization. A,C,E,G maximum intensity projection (MIP) of stability images. B, D,F,H shows zoomed in and rotated MIP images of accuracy images to show where the known green centerlines differ from the red algorithm centerlines and were they overlap in yellow. A- B is the $MDFE_i$ algorithm, C-D is the COM algorithm, E-F is the BT-$MDFE_i$ algorithm, G-H is the BT-COM algorithm.

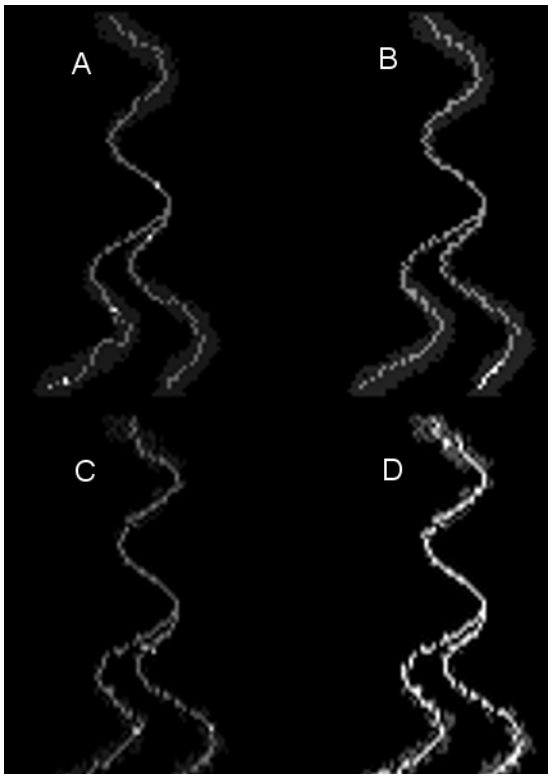

Figure 2.13. Stability images showing the inverted stability centerlines of the branching phantom with SD 20 Gaussian noise. (A) $MDFE_i$ stability lines on the segmented image. (B) COM stability lines on the segmented image. (C) BT-$MDFE_i$ stability on the skeleton. (D) BT-COM on the skeleton.

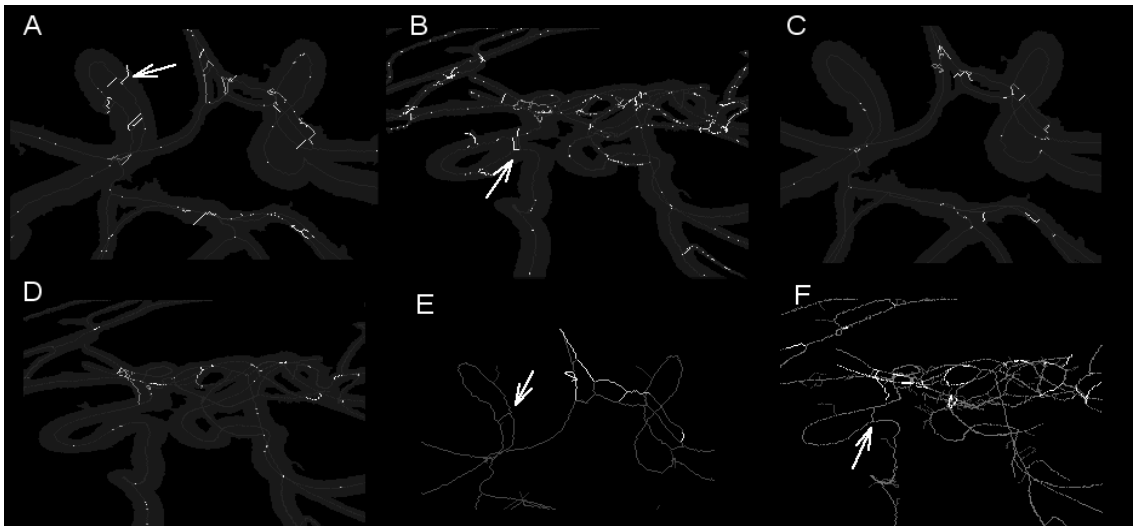

Figure 2.14. Maximum intensity projections of stability images show the center-line instability brightly. (A) $MDFE_i$ algorithm centerline transverse MIP. (B) $MDFE_i$ cost scoring the centerline passes through the kissing ICA siphon. (C) COM algorithm centerline transverse MIP. (D) COM cost scoring the centerline takes the larger wider loop around the ICA siphon instead of the narrow kissing point. (E) BT-COM centerline transverse MIP. (F) BT-COM centerline shortcuts through kissing vessel loop.

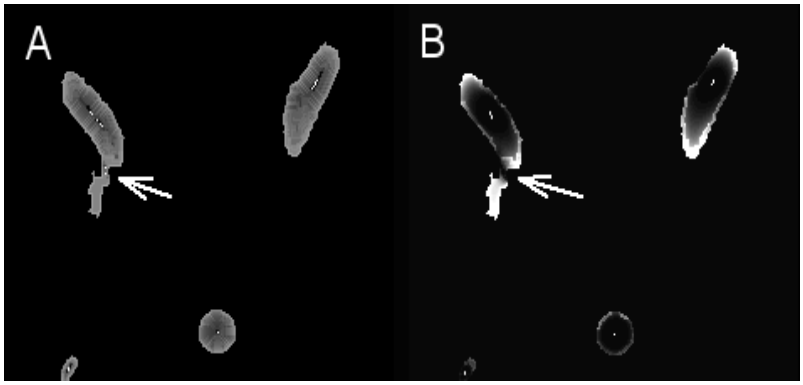

Figure 2.15. Cost function cross sections (A) The $MDFE_i$ cost function scores showing a kissing ICA siphon loop with the centerline passing through. (B) The COM cost function scores showing a kissing ICA siphon with no centerline passing through.

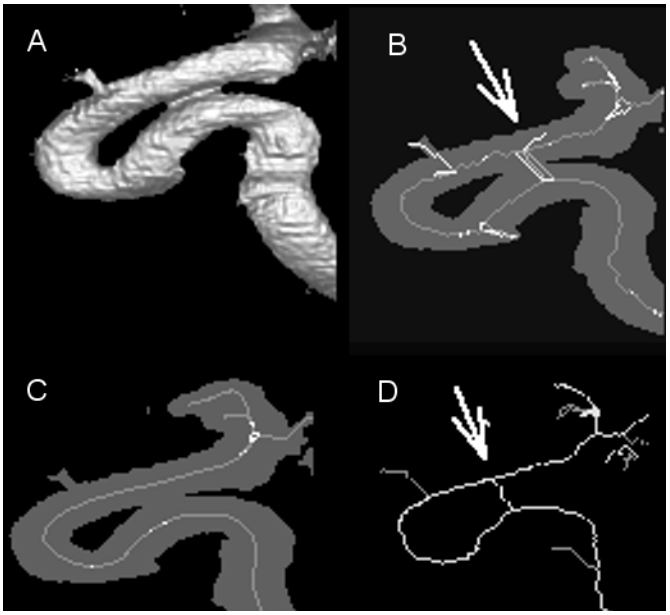

Figure 2.16. Stability MIP images of segmented kissing ICA siphon loop. (A) Shaded surface depth image of ICA loop shows thin kissing point. (B) $MDFE_i$ centerline passes through narrow kissing point. (C) COM centerline draws line around low scoring siphon loop. A centerline is made through the narrow kissing point but is removed by thresholding to eliminate short centerline lines segments. The COM centerline appears to come closer to the inside edge than the outer edge of the bend. (D) The BT-COM centerline passes through the narrow kissing point.

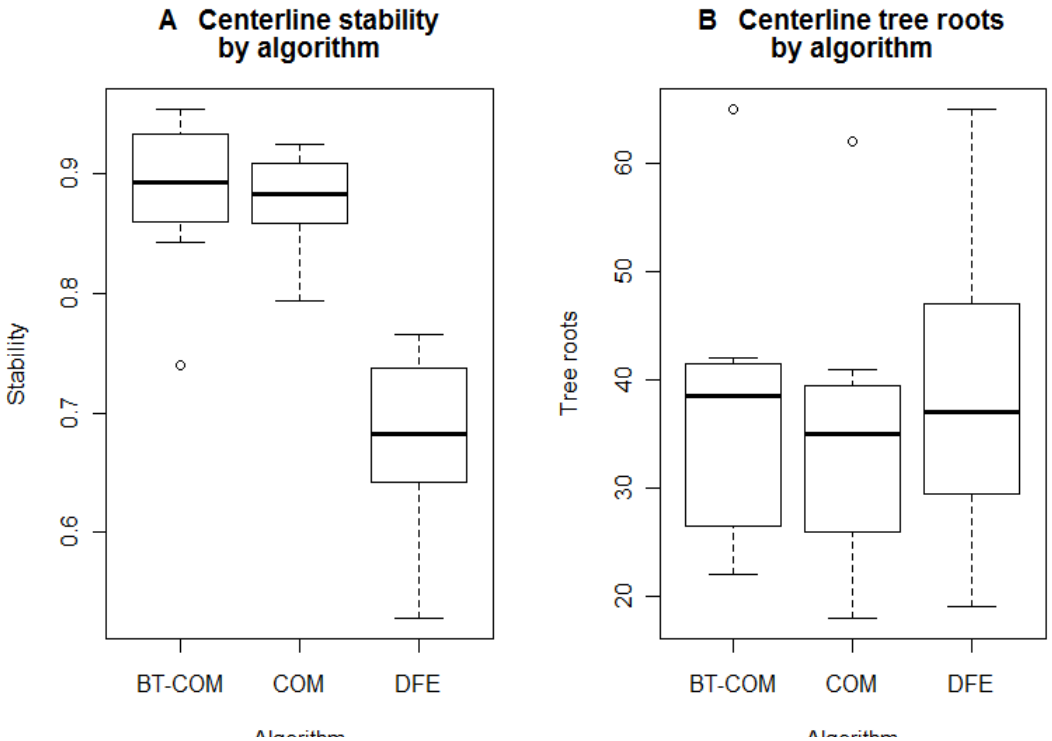

Figure 2.17. Algorithm stability (A) Box and whiskers plot showing the greater instability of the $MDFE_i$ (labeled DFE) centerline algorithm compared to COM and BT-COM centerline algorithms. (B) The three centerline algorithms produce a similar number of centerline tree ends used as tree roots for the centerline stability analysis.

Table 2.1. Helix line phantom stability and accuracy

Algorithm	Stability	RMSE of Accuracy
$MDFE_i$	0.880	0.240
COM	0.980	0.610
$BT\text{-}MDFE_i$	1.000	1.833
BT-COM	1.000	1.830

Table 2.2. Comparison of algorithm stability and accuracy on phantoms

Phantom	Algorithm	Number of trees	Stability	RMSE of Accuracy
SD 10	$MDFE_i$	3	0.930	0.393
SD 10	COM	3	0.960	0.463
SD 10	$BT\text{-}MDFE_i$	3	0.910	0.438
SD 10	BT-COM	4	1.000	0.437
SD 20	$MDFE_i$	3	0.946	0.674
SD 20	COM	3	0.950	0.528
SD 20	$BT\text{-}MDFE_i$	3	0.920	0.519
SD 20	BT-COM	4	1.000	0.457

Stability and accuracy comparison of the $MDFE_i$, COM, $BT\text{-}MDFE_i$ and BT-COM algorithms on branching tubular phantoms with standard deviation (SD) 10 and 20 distributed Gaussian noise.

Table 2.3. Comparison of centerline algorithms on MRA brain images

Algorithm	ICA siphons accurate	Portion ICA siphons correct	Both ICA correct in image	Mean number of trees	Standard deviation of trees	Mean stability	Standard deviation stability
$MDFE_i$	6/16	0.375	1/8	38.875	14.672	0.677	0.076
COM	16/16	1.000	8/8	35.125	13.314	0.877	0.042
BT-COM	10/16	0.625	4/8	37.500	13.617	0.883	0.068

Comparison of centerline stability, number of centerline tree roots and correctness of the centerline through the internal carotid artery (ICA) siphon between centerline algorithms on 8 brain artery MRA images.

Table 2.4. Means by algorithm

Algorithm	Mean stability	Mean number of trees
BT-COM	0.88275	37.50000
COM	0.87650	35.12500
$MDFE_i$	0.67737	38.87500

Table 2.5. Algorithm centerline stability measurements

Sample	DFE Trees	DFE stability	COM Trees	COM Stability	Thinning Trees	Thinning Stability
445	40	0.692	38	0.867	38	0.903
443	53	0.644	41	0.909	41	0.937
136	41	0.641	37	0.886	39	0.842
20	34	0.673	28	0.924	30	0.882
49	65	0.529	62	0.848	65	0.740
807	19	0.762	18	0.793	23	0.953
788	33	0.713	33	0.879	42	0.877
656	26	0.765	24	0.906	22	0.928

Literature cited

Arimura H, Li Q, Korogi Y, Hirai T, Abe H, Yamashita Y, Katsuragawa S, Ikeda R, and Doi K. 2004. Automated computerized scheme for detection of unruptured intracranial aneurysms in three-dimensional magnetic resonance angiography. Acad Radiol 11:1093-104.

Aylward SR, and Bullitt E. 2002. Initialization, noise, singularities, and scale in height ridge traversal for tubular object centerline extraction. IEEE Trans Med Imaging 21:61-75.

Bullitt E, Gerig G, Pizer SM, Lin W, and Aylward SR. 2003. Measuring tortuosity of the intracerebral vasculature from MRA images. IEEE Trans Med Imaging 22:1163-1171.

Burger W, and Burge MJ. 2007. Digital Image Processing: An Algorithmic Introduction using Java. 1st ed. Springer.

Chapman BE, Stapelton JO, and Parker DL. 2004. Intracranial vessel segmentation from time-of-flight MRA using pre-processing of the MIP Z-buffer: accuracy of the ZBS algorithm. Med Image Anal 8:113-26.

Cormen TH, Leiserson CE, Rivest RL, and Stein C. 2009. Introduction to Algorithms, Third Edition. 3rd ed. The MIT Press.

Dijkstra EW. 1959. A note on two problems in connexion with graphs. Numerische Mathematik 1:269-271.

Farnham JM, Camp NJ, Neuhausen SL, Tsuruda J, Parker D, MacDonald J, and Cannon-Albright LA. 2004. Confirmation of chromosome 7q11 locus for predisposition to intracranial aneurysm. Hum Genet 114:250-5.

Frangi AF, Niessen WJ, Hoogeveen RM, van Walsum T, and Viergever MA. 1999. Model-based quantitation of 3-D magnetic resonance angiographic images. IEEE Trans Med Imaging 18:946-956.

Hiroki M, Miyashita K, and Oda M. 2002. Tortuosity of the white matter medullary arterioles is related to the severity of hypertension. Cerebrovasc. Dis 13:242-250.

Homman H. 2007. Insight Journal - Implementation of a 3D thinning algorithm. Available from: http://www.insight-journal.org/browse/publication/181

Kang D-G, Suh DC, and Ra JB. 2009. Three-dimensional blood vessel quantification via centerline deformation. IEEE Trans Med Imaging 28:405-414.

Lesage D, Angelini ED, Bloch I, and Funka-Lea G. 2009. A review of 3D vessel lumen segmentation techniques: models, features and extraction schemes. Med Image Anal 13:819-845.

O'Flynn PM, O'Sullivan G, and Pandit AS. 2007. Methods for three-dimensional geometric characterization of the arterial vasculature. Ann Biomed Eng 35:1368-1381.

Parker DL, Chapman BE, Roberts JA, Alexander AL, and Tsuruda JS. 2000. Enhanced image detail using continuity in the MIP Z-buffer: applications to magnetic resonance angiography. J Magn Reson Imaging 11:378-88.

R Development Core Team. 2009. R: A language and environment for statistical computing. R Foundation for Statistical Computing, Vienna, Austria. ISBN 3-900051-07-0. Available from: http://www.R-project.org/

Rasband W. 1997. ImageJ, U.S. National Institutes of Health, Bethesda, Maryland, USA. Available from: http://rsb.info.nih.gov/ij/

Zhang L, Chapman BE, Parker DL, Roberts JA, Guo J, Vemuri P, Moon SM, and Noo F. 2005. Automatic detection of three-dimensional vascular tree centerlines and bifurcations in high-resolution magnetic resonance angiography. Invest Radiol 40:661-71.

Supplementary materials

Source images

The sample objects used for testing segmentation and centerline algorithm stability and accuracy included artificial phantom data and eight Time of Flight (TOF) MRA image data sets. A binary valued helix line phantom was created by propagating a sphere along a path defined by straight lines and helices. Two computer generated branching gray-scale phantoms with background intensity 100 and tubular objects with cross-sectional parabolic intensity profiles ranging from 150 at the edge to 200 at the middle of the artery with added Gaussian noise of standard deviation 10 and 20 were obtained from (Aylward and Bullitt, 2002).

The eight MRA image data sets were selected from our ongoing intracranial aneurysm study approved by the University of Utah Institutional Review Board. Three of the eight subjects were selected from high aneurysm risk family pedigrees (Farnham et al., 2004). Six subjects have intracranial aneurysms, including the three high-risk subjects. The patients were imaged with TOF-MRA on a Siemens TIM Trio 3.0 T MRI scanner. The images were acquired with anisotropic voxels (0.3 X 0.3 X 0.6mm^3) and were zero fill interpolated by a factor of 2 in all directions for final dimensions of 0.15 X 0.15 X 0.3 mm^3.

Segmentation

Each artery segmentation takes approximately 3 to 5 minutes on a 2.83 GHz Intel Core 2 Quad CPU running Linux. The branching phantoms and the arterial blood vessels

were segmented from the background using a Z-buffer segmentation and region growing method (Parker et al., 2000). In the Z-buffer segmentation (ZBS) algorithm, the Z-buffer stores the location (Z) along the project direction of the brightest point in the image along each ray. In a Z-buffer image formed by displaying the locations of the brightest voxels, voxels that project from arteries appear smoothly connected because there is a high probability that the high intensity vessel voxels will project and that adjacent projections will select voxels in close axial proximity. In extended regions of uniform signal where voxels project from background and other nonvessel tissues the Z-buffer image tends to appear noisy because there is little probability that voxels in adjacent projections share similar axial positions in the source image volume. Seed voxels for region growing are obtained by joining smoothly connected voxels in the Z-buffer. The smaller phantoms used seeds of 10 connected voxels and the larger brain images used seeds of 30 connected voxels. The 3D segmentations are completed by intensity-based region growing in the source images starting from the ZBS seed and iteratively adding voxels with intensity over a threshold. For the brain MRA images the region-growing threshold is determined from a histogram of the seed intensities as the maximum intensity of the bottom 15 percentile of the seed intensities. The seed threshold was selected to fill large aneurysms in our image collection.

The resulting vessel segmentations often contained internal holes in regions of low signal intensity in the source images caused by slow or recirculating blood flow. Holes were filled by finding empty bubbles completely surrounded by arterial voxels as determined by connected component analysis (Cormen et al., 2009). After this large hole

filling step, individual voxels were filled in that had 21 of 26 neighboring arterial voxels within a radius of 3 voxels as in (Zhang et al., 2005). This hole filling was repeatedly applied 3 times and then completely surrounded bubbles were filled once more. The hole filling parameters were selected to completely fill aneurysms in the tested subjects.

To eliminate small kissing arteries in the brain image segmentations, voxels less than 0.3 mm from the external surface of the segmented vessels were deleted from the segmentation. The voxel size is this study is 0.15 X 0.15 X 0.3 mm^3. Therefore all voxels less than 0.3 mm from the edge of the segmentation were removed, meaning that one voxel in the transverse x, y plane is removed. This reduced segmentation noise and only resulted in the loss of smaller peripheral blood vessels. This was acceptable because our study focused on the performance of centerlines in the region of the carotid siphon.

Literature cited

Arimura H, Li Q, Korogi Y, Hirai T, Abe H, Yamashita Y, Katsuragawa S, Ikeda R, and Doi K. 2004. Automated computerized scheme for detection of unruptured intracranial aneurysms in three-dimensional magnetic resonance angiography. Acad Radiol 11:1093-104.

Aylward SR, and Bullitt E. 2002. Initialization, noise, singularities, and scale in height ridge traversal for tubular object centerline extraction. IEEE Trans Med Imaging 21:61-75.

Bullitt E, Gerig G, Pizer SM, Lin W, and Aylward SR. 2003. Measuring tortuosity of the intracerebral vasculature from MRA images. IEEE Trans Med Imaging 22:1163-1171.

Burger W, and Burge MJ. 2007. Digital Image Processing: An Algorithmic Introduction using Java. 1st ed. Springer.

Chapman BE, Stapelton JO, and Parker DL. 2004. Intracranial vessel segmentation from time-of-flight MRA using pre-processing of the MIP Z-buffer: accuracy of the ZBS algorithm. Med Image Anal 8:113-26.

Cormen TH, Leiserson CE, Rivest RL, and Stein C. 2009. Introduction to Algorithms, Third Edition. 3rd ed. The MIT Press.

Dijkstra EW. 1959. A note on two problems in connexion with graphs. Numerische Mathematik 1:269-271.

Farnham JM, Camp NJ, Neuhausen SL, Tsuruda J, Parker D, MacDonald J, and Cannon-Albright LA. 2004. Confirmation of chromosome 7q11 locus for predisposition to intracranial aneurysm. Hum Genet 114:250-5.

Frangi AF, Niessen WJ, Hoogeveen RM, van Walsum T, and Viergever MA. 1999. Model-based quantitation of 3-D magnetic resonance angiographic images. IEEE Trans Med Imaging 18:946-956.

Hiroki M, Miyashita K, and Oda M. 2002. Tortuosity of the white matter medullary arterioles is related to the severity of hypertension. Cerebrovasc. Dis 13:242-250.

Homman H. 2007. Insight Journal - Implementation of a 3D thinning algorithm. Available from: http://www.insight-journal.org/browse/publication/181

Kang D-G, Suh DC, and Ra JB. 2009. Three-dimensional blood vessel quantification via centerline deformation. IEEE Trans Med Imaging 28:405-414.

Lesage D, Angelini ED, Bloch I, and Funka-Lea G. 2009. A review of 3D vessel lumen segmentation techniques: models, features and extraction schemes. Med Image Anal 13:819-845.

O'Flynn PM, O'Sullivan G, and Pandit AS. 2007. Methods for three-dimensional geometric characterization of the arterial vasculature. Ann Biomed Eng 35:1368-1381.

Parker DL, Chapman BE, Roberts JA, Alexander AL, and Tsuruda JS. 2000. Enhanced image detail using continuity in the MIP Z-buffer: applications to magnetic resonance angiography. J Magn Reson Imaging 11:378-88.

R Development Core Team. 2009. R: A language and environment for statistical computing. R Foundation for Statistical Computing, Vienna, Austria. ISBN 3-900051-07-0. Available from: http://www.R-project.org/

Rasband W. 1997. ImageJ, U.S. National Institutes of Health, Bethesda, Maryland, USA. Available from: http://rsb.info.nih.gov/ij/

Zhang L, Chapman BE, Parker DL, Roberts JA, Guo J, Vemuri P, Moon SM, and Noo F. 2005. Automatic detection of three-dimensional vascular tree centerlines and bifurcations in high-resolution magnetic resonance angiography. Invest Radiol 40:661-71.

CHAPTER 3

VALIDATION OF AN ARTERIAL TORTUOSITY MEASURE WITH APPLICATION TO HYPERTENSION COLLECTION OF CLINICAL HYPERTENSIVE PATIENTS

Karl T. Diedrich[1,2§], John A. Roberts[1], Richard H. Schmidt[3], Chang-Ki Kang[4], Zang-Hee Cho[4], and Dennis L. Parker[1,2]

[1]Utah Center for Advanced Imaging Research, Department of Radiology, University of Utah, 729 Arapeen Drive, Salt Lake City, UT 84108, USA

[2]Department of Biomedical Informatics, University of Utah, 26 South 2000 East Room 5775 HSEB, Salt Lake City, UT 84112, USA

[3]Department of Neurosurgery, University of Utah, Health Science Center, Bldg 550, 5th Floor, 175 N. Medical Drive East, Salt Lake City, UT 84132, USA

[4]Neuroscience Research Institute, Gachon University of Medicine and Science 1198, Kuwol-dong, Namdong-gu, Incheon, 405-760, Korea

[§]Corresponding author

Email addresses:

KTD: Karl.Diedrich@utah.edu
JAR: roberts@ucair.med.utah.edu
RHS: richard.schmidt@hsc.utah.edu
CKK: changkik@gmail.com
ZHC: zcho@gachon.ac.kr
DLP: parker@ucair.med.utah.edu

Abstract

Background

Hypertension may increase tortuosity or twistedness of arteries. We applied a centerline extraction algorithm and tortuosity metric to magnetic resonance angiography (MRA) brain images to quantitatively measure the tortuosity of arterial vessel centerlines. The most commonly used arterial tortuosity measure is the distance factor metric (DFM). This study tested a DFM based measurement's ability to detect increases in arterial tortuosity of hypertensives using existing images. Existing images presented challenges such as different resolutions which may affect the tortuosity measurement, different depths of the area imaged, and different artifacts of imaging that require filtering.

Methods

The stability and accuracy of alternative centerline algorithms was validated in numerically generated models and test brain MRA data. Existing images were gathered from previous studies and clinical medical systems by manually reading electronic medical records to identify hypertensives and negatives. Images of different resolutions were interpolated to similar resolutions. Arterial tortuosity in MRA images was measured from a DFM curve and tested on numerically generated models as well as MRA images from two hypertensive and three negative control populations. Comparisons were made between different resolutions, different filters, hypertensives versus negatives, and different negative controls.

Results

In tests using numerical models of a simple helix, the measured tortuosity increased as expected with more tightly coiled helices. Interpolation reduced resolution-dependent differences in measured tortuosity. The Korean hypertensive population had significantly higher arterial tortuosity than its corresponding negative control population across multiple arteries. In addition one negative control population of different ethnicity had significantly less arterial tortuosity than the other two.

Conclusions

Tortuosity can be compared between images of different resolutions by interpolating from lower to higher resolutions. Use of a universal negative control was not possible in this study. The method described here detected elevated arterial tortuosity in a hypertensive population compared to the negative control population and can be used to study this relation in other populations.

Background

There is evidence that hypertension can affect blood vessel morphology. Increasing stage of hypertension has been shown to correlate with increased tortuosity or twistedness of white matter arterioles in autopsy photomicrographs [1]. In vitro studies on extracted dog arteries showed increasing blood pressure caused increases in tortuosity [2]. In contrast, one study in Korea found that while the number and branches of

lenticulostriate arteries visible in Magnetic Resonance Angiography (MRA) images decreased in hypertensive subjects compared to negative controls, an increase in tortuosity was not seen in tortuosity measurements made on 2D projections of the 3D data [3].

Tortuosity measurement has the potential to quantify morphological changes in arteries due to hypertension. Tortuosity can be measured from MRA images of arteries. The process starts with MRA imaging of arteries, segmentation of arteries, calculation of centerlines, and calculation of tortuosity from the centerlines. Centerlines simplify arteries and other tubular structures to a single line passing through the middle of the artery making measurement of length and position possible. Measurements on the centerlines can be used to calculate tortuosity scores.

The most commonly used tortuosity measure is the distance factor metric (DFM) that requires two end-points to measure the ratio of the length L along the centerline and the distance d between two end-points [4-10]. The DFM suffers some weaknesses. Some arteries only have one anatomical end-point in an image volume and local tortuosity scores can rise and fall along an artery. The DFM can miss local tortuosity depending on the selection of the two end-points. Furthermore, the comparison of DFM tortuosity between multiple subjects can be challenging when the image volumes do not all share the same two anatomical centerline end-points.

Centerlines can be calculated by Dijkstra's algorithm [11] which finds the shortest or lowest cost path from any given point in the arterial segmentation to a selected goal point or node. Each voxel (three-dimensional pixel) of the arterial segmentation is

assigned a cost based on its position with respect to the goal. The longest lowest cost paths from the distal ends of the arteries back to a central goal node are the centerlines [12]. The selection of the central goal node and cost function can affect the path of the centerline.

Existing images from previous studies and clinical scans provide a large set of data for analysis that saves the time and cost of acquiring new images. Reusing existing images for comparison studies may present difficulties if the images have been acquired with different parameters including the field strength of the magnetic resonance imaging (MRI) scanner, resolution, and field of view (FOV) placement. FOV placement may affect whether the same artery segments are seen in both views. Differences in resolution may affect the tortuosity measure. Some vessels visible in MRA images from high 7.0 T field strengths may not be seen at lower resolution and the high field may cause phase flow artifacts [13, 14] that can be mistaken for arteries by centerline algorithms, requiring pre- or postprocessing for removal. Filtering can cause data loss and could affect the tortuosity measure. Negative controls may be obtained from existing images from patients with nonvascular diseases but proof of being truly negative is needed.

Testing of centerline and tortuosity measurement algorithms can be conducted on numeric phantoms. Numeric phantoms are three-dimensional shapes generated by equations in computer software with known morphology and centerlines. Algorithm calculated centerlines can be compared to known centerlines to assess accuracy and tortuosity measures can be tested on different shapes with known tortuosity.

In this study we first test the stability and accuracy of our Dijkstra's shortest path centerline algorithms by using different cost functions and goal node voxels on numeric phantoms and a sample of brain MRA images. We modified the classical DFM tortuosity measurement to create a tortuosity curve that provides additional information and tested the measurement on numeric phantoms. We applied the DFM tortuosity curve measurement to existing brain MRA images. The images included data on the same subjects filtered for noise with different filters and at different resolutions to test the effects of filtering and resolution on tortuosity. Hypertension data from the Korean hypertension study [3] and clinical hypertension data from Utah were tested to determine if the method can detect a correlation between hypertension and tortuosity of the arteries visible in MRA images. Tortuosity was also compared between three negative controls to test similarity and determine if universal negative controls can be used.

Methods

Image analysis flow

The image data are analyzed by interpolation, filtering, segmentation, centerline extraction, tortuosity curve calculation, and reading of the tortuosity score. The interpolation and filtering were optional steps. Segmentation was not needed in numeric phantoms without background noise. Details on the analysis steps are described below.

Centerline cost functions

Cost functions for input into Dijsktra's shortest path centerline algorithm included the modified distance from edge (MDFE) cost, center of mass (COM) and distance from edge (DFE)-COM. The DFE measures the distance of each segmented voxel to the nearest edge of the artery. The DFE exhibits a degeneracy which can interfere with centerline extraction: adjacent voxels may be equally distant from their nearest respective edges. The DFE is essentially a one-dimensional measure, ignoring all other edge locations but one in its calculation. The MDFE was developed [12] to use local spatial information to break ties between adjacent voxels with the same DFE values.

The COM function is computed by iteratively moving each voxel toward the current COM of its adjacent neighbor voxels, effectively collapsing the object inward. For the objects considered in this study, 30 iterations of motion toward the center of mass were sufficient. Each iteration uses the previous iteration's mean positions and the cumulative distance moved by each voxel is recorded. To calculate the COM cost for each voxel, the cumulative distances moved were divided by the minimum nonzero distance moved in the entire segmentation and the result was cubed. Voxels at the segmentation edge moved farther, generating higher cost and voxels near the center moved shorter distances, generating lower costs. Because the COM calculation depends on the relationship between each voxel and its neighbors, it is highly sensitive to the shape of the object, eliminating most of the degeneracies encountered with the DFE algorithm.

The DFE-COM cost function combines the two cost functions. During the iterations of the COM algorithm, rather than assigning uniform weights to neighbor voxels, a weighted center of mass was computed using the DFE values as weights. Weighting gave more influence to the voxels with higher DFE in the middle of arteries when calculating the COM cost function.

Numeric phantom generation

Numeric phantoms were generated by beginning with defined single point width centerlines. The centerlines were then discretized and placed within a discrete image volume. All voxels within a predefined radius of the centerline voxels were identified as object voxels, simulating imaged arteries. A subset of the discrete centerline locations were then used as positive controls for comparison with subsequent centerline extraction (Figure 3.1).

Centerline stability and accuracy

The stability and accuracy of the DFE-COM cost-function centerline algorithm was measured and compared to the separate MDFE and COM cost function centerline algorithms on a set of numeric phantoms. The first numeric phantom considered was a comb phantom with a three voxel radius. A second series of branching phantoms with increasing image noise as designed by Aylward et al. [15] was also studied. Finally, the

stability and ability of each algorithm to calculate centerlines around the internal carotid artery (ICA) siphon loop were tested with eight 3.0 T brain MRA image volumes.

Tortuosity measurement

Tortuosity was determined at every point along the selected centerlines with the DFM [5, 8] creating tortuosity curves. A single tortuosity measure was taken from each tortuosity curve either at the end of centerline or where the DFM was a maximum. Selection of the DFM value depended upon properties of the arteries being measured and is described in detail later.

Tortuosity measurement of phantoms

The DFM tortuosity measurement was tested on 3-D numeric helix phantoms of increasing pitch with the DFE-COM centerline tortuosity measurement. The helix phantoms were generated by drawing a line with the equation $h(t) = [r*\cos(t), r*\sin(t), (p*t)/(2\pi)]$ where r was the helix radius and p was the pitch of the helix and the radius of the simulated arterial width was 6 voxels. The helix radius r was fixed at 100 and four helices were generated with pitches $5(2\pi)$, $10(2\pi)$, $20(2\pi)$ and $40(2\pi)$ (Figure 3.2). The quantitative DFM tortuosity scores were taken at the highest peak of the tortuosity curves.

Segmentation

The arteries in the MRA images were segmented from background (Figure 3.3) using the Z-buffer segmentation (ZBS) algorithm [16]**.** ZBS algorithm works based on the assumption that arteries are the brightest structures in the image, they are sparsely represented in the image volume, and that bright artery voxels will be spatially close together. The algorithm casts rays in the Z axis through the 3D image volume finding the z-position of the brightest voxel in each ray. The z-positions of clusters of brightest voxels are then used as seeds for region growing and artery segmentation [16]. The artery segmentation is grown from the seed voxels by iteratively adding all neighboring voxels with intensities over a predetermined intensity threshold. The intensity threshold was set as the 20^{th} percentile of all intensities of the seed voxels. Bubbles in the segmentation caused by low intensity slow moving or recirculating blood were filled using connected component analysis [17]. Small holes at the edges of the segmentation were filled by iterative reclassification. In three iterations, hole voxels were filled when they were surrounded by arterial voxels within 8 voxel steps along rays in 24 of 26 directions [12]. Finally connected component bubble filling was repeated.

Human source images for hypertension tortuosity study

The hypertensive subjects were drawn from two populations. Twenty hypertensive subjects were identified by measurement of blood pressure at the Neuroscience Research Institute (NRI), Gachon University of Medicine and Science in Incheon, South Korea [3] and twenty negative controls were collected in the same study

under approval from the Gachon University institutional review board and the Korean Food and Drug Administration.

For the second population, MRA images were selected from existing brain MRA images acquired from clinical hypertensive patients between 2008 and 2010 at the University of Utah Medical Center. The selection of subjects and the retrospective study of previously acquired images were performed with approval from the University of Utah institutional review board. All the Utah hypertensives (N =21) had a history of hypertension in the medical record demonstrating that they were under the care of a physician, making this a controlled hypertensive population. Diagnoses commonly associated with hypertension were allowed in the Utah hypertensive case population including transient ischemic attack, ischemic stroke, arterial disease, heart disease, sleep apnea and atrial fibrillation. Other diseases that may independently affect vasculature were excluded from the Utah hypertensive case population. These were diabetes, cancer [18], intracranial aneurysm, and genetic syndromes: hereditary hemorrhagic telangiectasia, Marfan syndrome and Loeys-Dietz syndrome [19, 20]. The Utah negative control population was collected with IRB approval from clinical brain MRA images acquired from 2008 to 2010 (N = 45). The Utah negative control population had the following traits: subjects with headache, trigeminal neuralgia or head trauma; available brain MRA head images; no vascular pathology recorded in the radiology report; and no indication of the above listed diseases associated with hypertension in the subjects' medical records.

A third negative control population was obtained from a study on healthy aging conducted in North Carolina, U.S.A. [21]. Vascular and psychological diseases were screened out in this sample.

MRI scanners

The data were acquired on different MRI scanners. The NRI data set was acquired with a 7.0 T MRI scanner (Magnetom, Siemens Medical Systems, Erlangen, Germany) [22, 23]. The North Carolina data were acquired with a 3.0 T MRI scanner (Allegra, Siemens Medical Systems). The Utah images were clinical scans from both 1.5 T (GE) and 3.0 T (Siemens) MRI scanners at a range of image resolutions.

Arteries measured

The arteries measured, the start and end points of the centerlines considered, and the points along the tortuosity curve selected for tortuosity measurement are described in Table 3.1. Examples of artery selection are shown in Figure 3.4. The measurements for the lenticulostriate arteries (LSA) were for the left-most, right–most, and a mean of up to four prominent LSAs. Figure 3.5 demonstrates the tortuosity curves created for an internal carotid artery (ICA) with the DFM measurement taken from the peaks of the curves (Figure 3.5 top) and the left anterior cerebral artery (ACA) – anterior communicating artery (Acom)– right ACA (Figure 3.5 bottom) measurement taken from the ends of the curves.

Filtering the images

The NRI data required filtering before segmentation. The image data were median filtered; then the filtered image was subtracted from the original image. The arteries were segmented from the subtracted image. The effect of filtering on tortuosity was tested by measuring tortuosity of the Korean hypertensive population treated with different filters: no median filter, 5x5 median filter and an 11x11 median filter. After the comparison the 5x5 median filter was selected and used for treating the NRI data before segmentation. An exception was made where no filtering step used on segmentations used for measuring the small LSAs.

Resolution and interpolation

The images were acquired at several different resolutions. Lower resolution images were sinc interpolated to higher resolutions [24]. For each subject in the NRI population, two MRA data sets were acquired: a thicker resolution (low 0.8x0.8x0.8 mm) set and a thinner and higher resolution (0.23x0.23x0.36 mm) set. The lower resolution data were interpolated to resolutions of 0.4x0.4x0.4 mm and 0.2x0.2x 0.2mm. The clinical Utah data were acquired from 0.38x0.38x1.6 mm (and interpolated on the scanner to 0.19x0.19x0.8) to 0.52x0.52x1.0 mm resolution and the lower resolution images were 2X interpolated to higher resolution (0.52x0.52x1.0 to 0.26x0.26x0.5 mm). The North Carolina data were acquired at 0.5x0.5x0.8 mm resolution and interpolated to 0.25x0.25x0.4 mm.

The effect of resolution and interpolation were measured in the NRI data set by measuring tortuosities of the same arteries for the same subjects at 0.4x0.4x0.4 mm, 0.2x0.2x0.2 mm and 0.23x0.23x0.36 mm resolutions. The 0.4x0.4x0.4 mm, 0.2x0.2x0.2 mm were interpolated from the same data acquisition and the 0.23x0.23x0.36 mm were acquired separately. The ICA arteries are only in the thicker transverse lower resolution volume limiting the testing of resolution effects to between the 4X (0.2x0.2x0.2 mm) and 2X (0.4x0.4x.4 mm) interpolations of the lower resolution image.

Tortuosity comparisons

Arterial tortuosity was measured and compared between different data sets and sub sets. Sample data information was stored in a MySQL (http://www.mysql.com/) relational database coupled to the R statistical system [25] for visualization and statistical analysis. Comparisons were tested with the Wilcoxon rank-sum test. The tortuosity comparisons were between: different median filter subtractions of the NRI data, all resolutions of NRI data; the three negative controls; males and females; the NRI hypertensives and negatives; and Utah hypertensives and negatives.

Results

Centerline stability and accuracy

Centerline accuracy was measured by comparing the measured centerline with the true centerline in the numeric phantoms and stability was measured by testing the

centerlines found with different starting points. The results for the numeric phantoms are summarized in Figure 3.6 and Tables 3.2 and 3.3. The multiple branches of the comb phantom (Figure 3.1 left) pulled the COM centerline in red below the true centerline in green (Figure 3.6 left). The MDFE cost (Figure 3.6 middle) and DFE-COM (Figure 3.6 right) centerlines overlap (in yellow) more with the true green centerline than the COM centerline.

Centerline stability as a function of cost function algorithm on brain MRA images is summarized in Table 3.4. The DFE-COM was tested on the ICA siphon loop, visualized with a white centerline in Figure 3.4 top left, where it loops back upon itself often kissing itself and causing problems for centerline extraction. The DFE-COM was able to complete as many ICA siphon loops as the COM algorithm with similar stability.

Tortuosity measurement of phantoms

The DFE-COM centerline DFM tortuosity scores were higher for tighter coiled helix phantoms with lower pitches and the tortuosity scores increased proportionally to the increase in the number of coils (Table 3.5). The pitch 40(2π)-helix has approximately one coil (DFM = 2.48) and the pitch 20(2π)-helix has approximately two coils and has almost double (ratio = 1.95) the tortuosity score (DFM = 5.45). The tortuosity curves were displayed with the distance d (Figure 3.7 top) or length L (Figure 3.7 bottom) on the x-axis showing the rise and fall of the tortuosity curve.

Median filter effect

The 7.0 T images were segmented with no suppression of background noise under the ZBS segmentation algorithm shown in Figure 3.8, top. Subtracting a median filtered image from the images as the first step in the segmentation removed the background noise from the segmentation but also removed some of the small lenticulostriate arteries while leaving the larger arteries especially in the case of the 5x5 median filter (Figure 3.8 middle). The larger 11x11 median filter removed most background noise but left some noise near the larger arteries while leaving most LSAs in the segmentation (Figure 3.8 bottom).

The median filter subtractions (none, 5x5 and 11x11) had no significant effect on tortuosity measurements of left ACA, right ACA, left to right ACA, left ACA and right ACA arteries of the hypertensive Korean population at the $\beta = \alpha/n = 0.05/8 = 0.00625$ significance level with a two-sided Wilcoxon rank-sum test.

Resolution and interpolation effect on tortuosity

The tortuosity was measured for the Korean hypertensive and negative control populations from the low and high-resolution images. The image volumes were not all long enough to capture the ICA accounting for low numbers of ICA measurements. Out of the total population size of 40 there were: 19 2X interpolated left ICA, 19 2X interpolated right ICA, 21 4X interpolated left ICA and 23 4X interpolated right ICA. The tortuosity values were compared with a 2-sided Wilcoxon rank-sum test, and a paired 2-sided Wilcoxon rank-sum test on all cases where measurements were made on both the

high and low interpolations of the same artery. The 4X interpolation had 6.40% higher left ICA (P = 0.294, paired P = 0.00042) and 3.65% higher right ICA (P = 0.452, paired P = 0.0348) tortuosity than the 2X interpolation (Figure 3.9 top). The mean resolution of 0.23x0.23x0.36 mm (mean 0.273 mm) is closer to 0.2x0.2x0.2 mm (0.0733 mm difference) than 0.4x0.4x0.4 mm (0.127 mm difference). The mean DFM taken from the tortuosity curves of the left ACA, right ACA and left to right ACA of the 0.23x0.23x0.36 mm images was 6.89±2.45% greater than the 0.4x0.4x0.4 mm images of the same subjects. The 0.2x0.2x0.2 mm images actually had 3.05±1.89% lower tortuosity than the 0.23x0.23x0.36 mm images. The difference in magnitude of both mean resolution and tortuosity between 0.2x0.2x0.2 mm and 0.23x0.23x0.36 mm images was smaller than between the 0.4x0.4x0.4 mm and 0.23x0.23x0.36 mm images (Figure 3.9 bottom). Due to increased similarity of scores, only the 0.2x0.2x0.2 mm and 0.23x0.23x0.36 mm were used for the hypertensive and negative control comparison experiments later in this study.

Comparison of negative control populations

The Korean negative control population showed significantly less arterial tortuosity compared to arteries of the Utah and the North Carolina negative controls (Figure 3.10) and the three populations were of similar age (Table 3.6). The Utah and North Carolina negative controls did not have significantly different arterial tortuosity. ANOVA analysis of the three negative controls: NRI Korean, North Carolina and Utah hospital showed significant differences in the left ACA, left to right ACA, left ICA, and right ICA arteries at the $\beta = \alpha/n = 0.05/5 = 0.01$ level. Pair-wise comparisons between the

negative controls with a 2-sided Wilcoxon rank-sum test showed the Korean population had significantly lower tortuosity of the left to right ACA, left ICA and right ICA than North Carolina and Utah hospital population at the $\beta = 0.01$ level. The North Carolina and Utah populations did not show any significant differences in arterial tortuosity.

Female and male comparisons

The Utah and North Carolina negative populations were split evenly between males and females while the Korean negative population was mostly female. Ethnicity was rarely indicated in the Utah medical record but based on the composition of the state of Utah, the subjects are most likely white European descent. The North Carolina population was mostly of white European descent (Table 3.6). The Korean control was a different ethnicity (Asian versus white European descent) and had a greater percentage of females.

Male and female North Carolina and Utah populations showed no significant differences at the $\beta = \alpha/n = 0.05/5 = 0.01$ level of 2-sided Wilcoxon rank-sum tests for five arteries measured. The lowest P-Value was of the left ICA (P=0.0288) of the North Carolina population where tortuosity values for males were higher than for females and females had higher tortuosity in three of five arteries measured. There was no significant difference in tortuosity between males and females in eight arteries compared at the $\beta = \alpha/n = 0.05/8 = 0.0625$ level in the Utah negative control (lowest P = 0.0114 with a 1.40% increase in male right VA tortuosity).

There was no significant difference in arterial tortuosity between males and females in our entire current collection of tortuosity measurements at the $\alpha = 0.05$ level (lowest $P = 0.342$) (Figure 3.11). The collection included the three negative controls, and subjects with vascular diseases. The diseases included hypertension, diabetes, cancer, stroke, intracranial aneurysm, hereditary hemorrhagic telangiectasia, Marfan syndrome and Loeys-Dietz syndrome subjects. There are more females (257) in the collection than males (185). The mean ages were similar for females (48.2) and males (46.5).

Korean hypertension tortuosity comparison

The Korean hypertensive population had higher tortuosity across all 13 artery measurements than the Korean negative control (Figure 3.12). Ten were significant at the $\alpha = 0.05$ level of the 1-sided Wilcoxon rank sum test. Even with the statistical correction of $\beta = \alpha/n = 0.05/13 = 0.0038$, 5 of the 13 tortuosity measurements were significantly higher in the Korean hypertensive population. The most significant measurements were the left ACA ($P= 0.00377$), the end DFM of left LSAs ($P = 0.000161$), the end DFM of the right LSAs ($P = 0.00052$), the peak DFM of the left LSAs ($P = 0.00977$) and the peak DFM of the right LSAs ($P = 0.00080$). There were more prominent LSAs per subject in the negative control (3.50 left, 3.35 right) than in the hypertensive subjects (2.15 left, 2.30 right).

Utah hypertension

The Utah hypertensive population (N=21) did not show significant increases in tortuosity compared to the Utah hospital negative control (N=45) at the $\beta = \alpha/n = 0.05/8 = 0.00625$ level (Figure 3.13). The test was conducted only against the Utah negative control population. Not all images contained measurable arteries for all arteries examined. The number of measurements and statistical test results are in Table 3.7. An F-test of variances showed higher variance of the hypertensive Utah population tortuosity than the negative control of the right ICA ($P = 0.00206$), left VA ($P = 0.00093$) and right VA ($P = 0.00174$) at the $\beta = 0.00625$ level. The hypertensives were insignificantly higher in tortuosity of seven of the eight arteries compared.

Discussion

We were able to develop a process of measuring arterial tortuosity including segmentation, filtering, interpolation, centerline extraction and DFM tortuosity analysis. The DFE-COM centerline was selected for making tortuosity measurements because it was able to calculate centerlines around most of the ICA siphon loops in a brain MRA data set and had better accuracy in the comb phantom. The subtraction of median filtered images from the MRA data had no significant effect on tortuosity and was used when necessary to improve artery segmentation. The 5x5 median filter was selected when measuring tortuosity of arteries other than the LSAs in the NRI data for the filter's ability to remove more fully background noise and process images faster than the larger filter while producing no significant change in tortuosity measurement. There was too much

chance of data loss when measuring tortuosity of the LSAs to justify the use of the median filter. The DFM tortuosity curve consistently measured the increasing tortuosity of the helix phantoms. Interpolating lower resolution images to higher resolution reduced the effects of resolution on tortuosity measurement. These results led us to use interpolation when comparing tortuosity in hypertensive populations versus negative controls.

Our methods measured a statistically significant increase in arterial tortuosity in the NRI Korean hypertension population compared to the Korean negative control. We also observed a dependence of tortuosity measurements upon image resolution. Higher resolution images increased the DFM tortuosity scores. Interpolating lower resolution images to higher resolutions reduced or eliminated the reduction in tortuosity for lower resolutions. Finally different populations may have different baseline tortuosities.

Hypertension correlated with increased arterial tortuosity in the Korean population study. The consistency across the arteries measured suggests that increased arterial tortuosity with hypertension is a systemic phenomenon. Greater change in tortuosity was seen in the ICA and LSA arteries than in the ACA measurements. The ICAs are longer than the ACAs possibly allowing more twisting due to increased hypertension. The LSAs are narrower than the ACAs and small narrow arterioles have been shown to twist strongly in response to hypertension [1]. The LSAs also had the higher significance of the tortuosity increase. To simplify measuring arterial tortuosity for clinical use, measuring one longer or narrower diameter artery may suffice for gauging tortuosity.

The correlation between tortuosity and hypertension was not repeated in the Utah populations. The Utah hypertensive group was under physician care; therefore many patients may have been on antihypertensive medications making this a largely controlled hypertensive population. Lack of completeness in the medical records made the number of subjects on hypertensive medication difficult to determine. A future experiment could compare controlled versus uncontrolled hypertensive (when identified) populations to study if antihypertensive medications have an effect on arterial tortuosity. Another possibility is that the Utah Hospital negative control is not truly negative. However, the Utah Hospital negative control was similar to the North Carolina negative control population indicating that the Utah hospital control was negative for increased arterial tortuosity and that patients imaged for reasons other than vascular disease reasons are usable as negative controls.

In a retrospective analysis of images such as this one, universal negative controls may not be possible. The Korean population showed significantly lower tortuosity than the Utah population. The North Carolina negative control was similar to the Utah hospital population in tortuosity. The Korean negative control population was mostly female. Females in the Utah hospital and North Carolina negative controls and in the entire tortuosity collection did not show significantly lower tortuosity than the corresponding male populations. The Korean data were higher resolution than the North Carolina or Utah data after final interpolations. Any remaining resolution effect on tortuosity would increase the Korean data more than the others but they still had the lowest tortuosity of the negative controls. The Utah hospital and North Carolina populations were mostly

white Americans of European descent and the Korean population was all Korean descent. Ethnicity remains as one possible cause of the decrease in Korean population tortuosity but the negative Korean control tested here was not a broad representation of the Korean population. With the ability to interpolate images taken at different resolutions we will attempt to obtain more ethnic populations from clinical images to compare arterial tortuosity to determine if ethnicity affects arterial tortuosity.

Conclusions

The methods in the study were able to measure a correlation between hypertension and arterial tortuosity. The DFE-COM centerline algorithm was able to make centerlines for the arteries of interest. The median filter subtraction allowed segmentation of the high-resolution data sets without affecting tortuosity. A significant increase in arterial tortuosity was measured in the uncontrolled NRI Korean hypertensive population versus a corresponding negative control. The Korean hypertensive population was not representative of all hypertensive populations or even of all Koreans. No significant arterial tortuosity increase was seen in the controlled Utah hypertensive population. Therefore we do not know if the increase in tortuosity with hypertension occurs in all populations. These methods can be used to study more populations to find out more about the relationships between hypertension and arterial tortuosity.

List of abbreviations used

ACA anterior cerebral artery

Acom anterior communicating artery

COM center of mass

d distance

DFE distance from edge

DFM distance factor metric

FOV field of view

HTN hypertensive

ICA internal carotid artery

L left

L length

LSA lenticulostriate artery

MDFE modified distance from edge

MIP maximum intensity projection

MRA magnetic resonance angiography

MRI magnetic resonance imaging

NEG negative

R right

T Tesla

TOF time of flight

ZBS Z buffer segmentation

Competing interests

There are no competing interests.

Authors' contributions

KTD developed the software, conducted the measurements and wrote the paper. JAR, DLP and RHS aided in designing the experiments and writing the paper. CKK and ZHC collected and provided the NRI data and contributed to the analysis of the results of the NRI data. All authors read and approved the final manuscript.

Acknowledgements

This work was supported by NLM Grants: T15LM007124, and 1R01 HL48223, and the Ben B. and Iris M. Margolis Foundation.

We greatly appreciate the help of the staff at the Utah Center for Advanced Imaging Research in supporting this research.

The North Carolina negative control population used in this paper were generated and made available by the CASILab at The University of North Carolina at Chapel Hill and were distributed by the MIDAS Data Server at Kitware, Inc.

Figure 3.1. Numeric phantom generation. (left) The comb phantom was made from a comb shaped centerline. (right) A helix phantom was made from a helical centerline

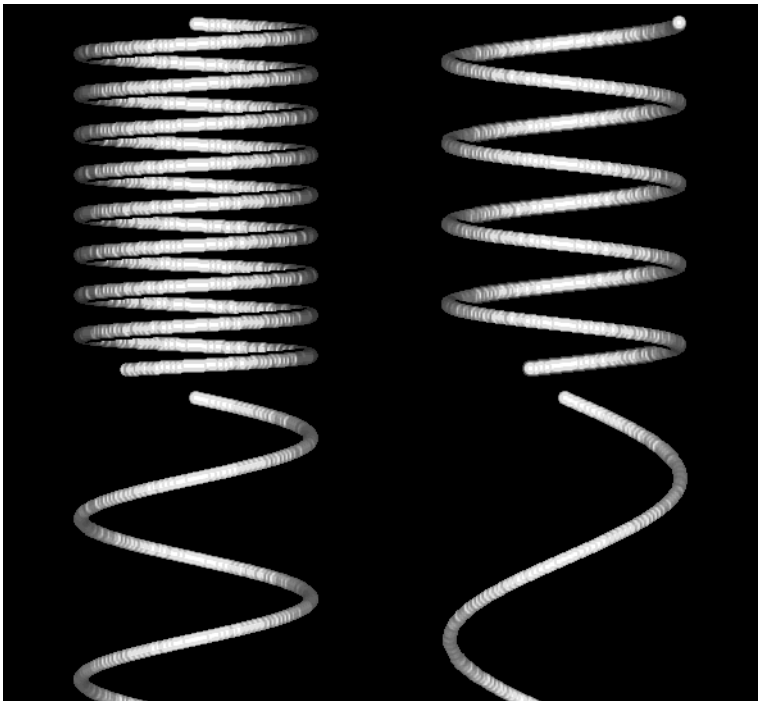

Figure 3.2. Phantom helices. 3-D helix phantoms were display with shaded surfaces. (top left) Pitch 5(2π). (top right) Pitch 10(2π). (bottom left) Pitch 20(2π). (bottom right) Pitch 40(2π).

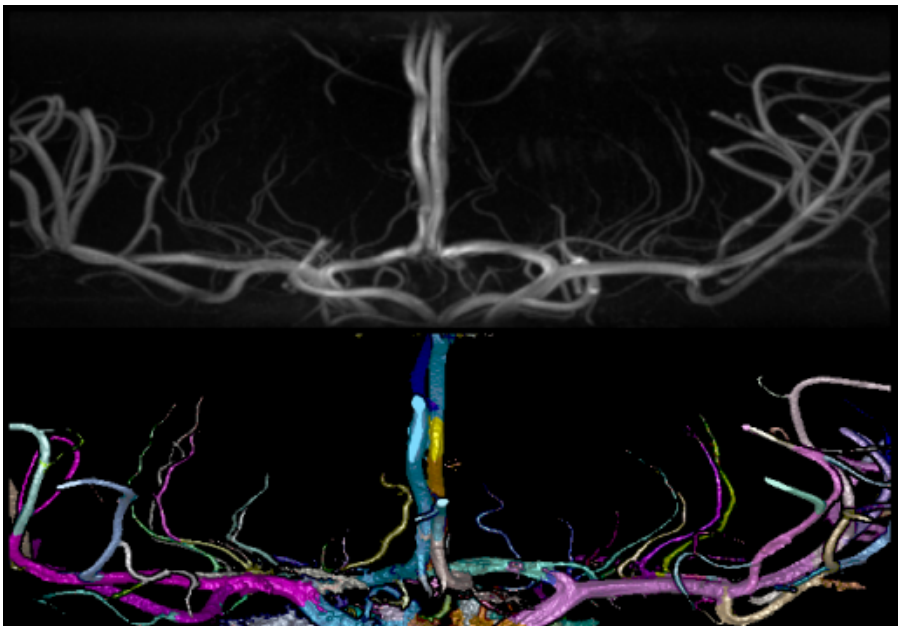

Figure 3.3. High resolution artery segmentation. (top) A high-resolution magnetic resonance angiography normotensive image was shown in maximum intensity projection. (bottom) Segmentation of the arteries was shown in shaded surface with colors to highlight bifurcations.

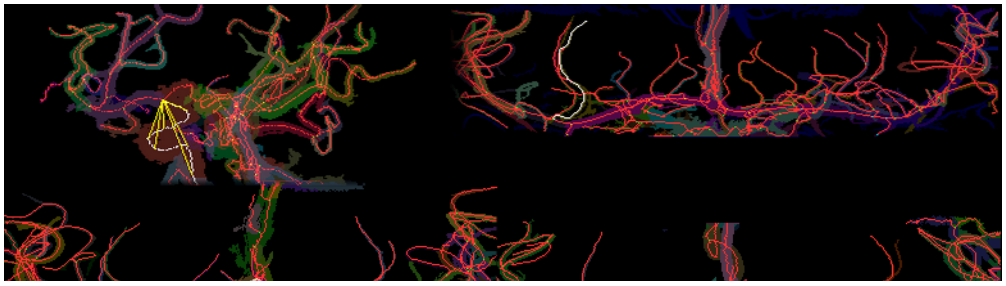

Figure 3.4. Selected centerlines. Centerlines of arteries and selections in white for tortuosity measurement were shown in maximum intensity projection (MIP). (top left) Right ICA was selected in white with progressive distance d in yellow. (top right) A lenticulostriate artery (LSA) of a normotensive subject was selected. (bottom left) The left to right ACA of a hypertensive patient was selected. (bottom right) The anterior cerebral artery (ACA) of a hypertensive subject was selected.

Figure 3.5. Artery tortuosity curves. Tortuosity curves of one subjects. (top). Tortuosity curves of three different subjects ICA arteries. The black curve is from Figure 3.4 top left. Tortuosity rises and falls. (bottom). Repeated tortuosity curves of the left to right ACA artery of the same subject, from Figure 3.4 bottom left, measured from different MRA images.

top

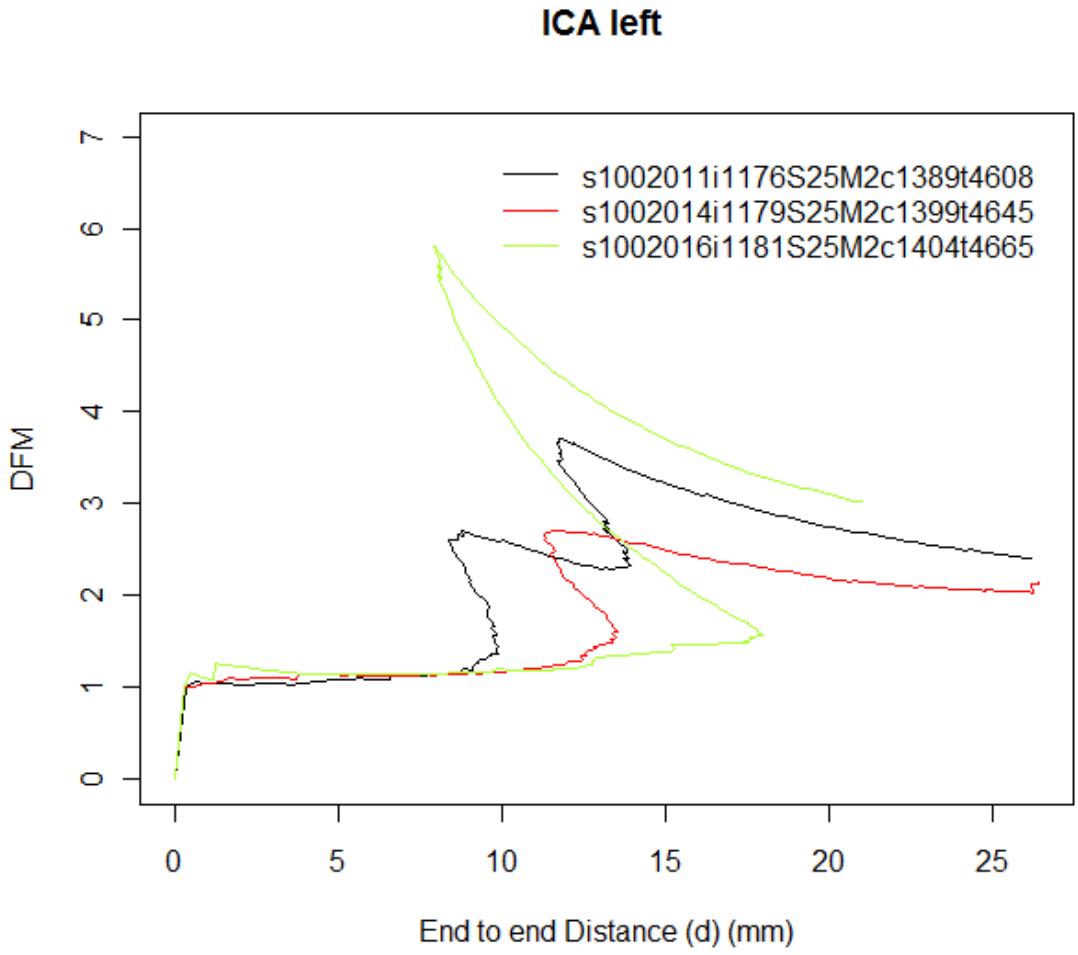
ICA left
s1002011i1176S25M2c1389t4608
s1002014i1179S25M2c1399t4645
s1002016i1181S25M2c1404t4665
DFM
0
1
2
3
4
5
6
7
0
5
10
15
20
25
End to end Distance (d) (mm)

bottom

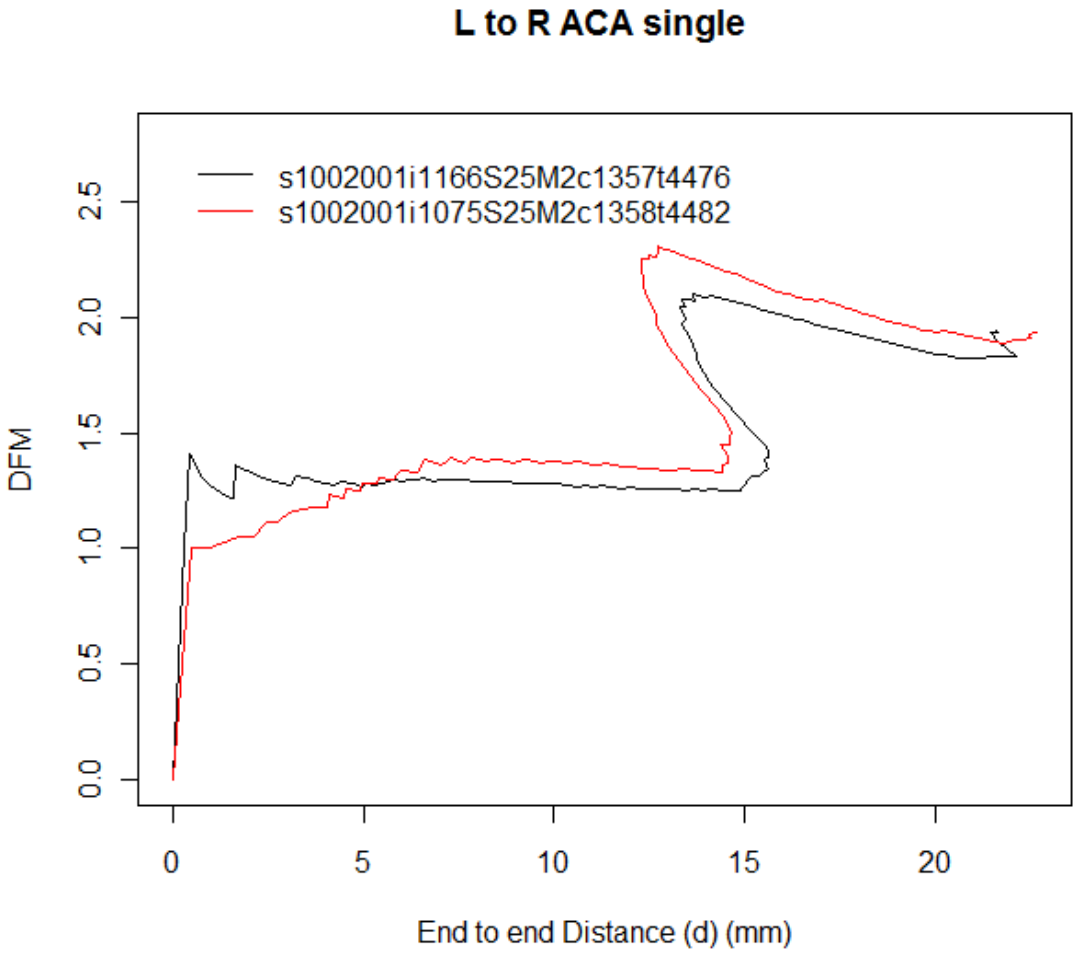

Figure 3.5 continued.

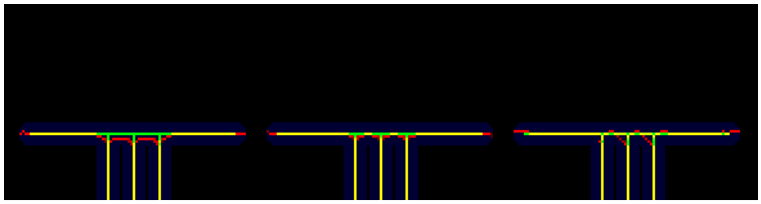

Figure 3.6. Comb phantom. Comb phantom where green is the true centerline, red is the algorithm calculated centerline and yellow is where the true and calculated centerline overlap. (left). The COM accuracy was displayed. (center) The MDFE accuracy was displayed. (right) The DFE-COM accuracy was displayed.

Figure 3.7. Phantom tortuosity curves. Helix phantom tortuosity curves are shown in maximum intensity projection. The pitch 5(2π) (black), pitch 10(2π) (red), pitch 20(2π) (green) and pitch 40(2π) (blue) phantoms decrease in tortuosity. (top) DFM tortuosity plotted versus distance d from the start. (bottom) DFM tortuosity plotted versus Length L from the start.

top

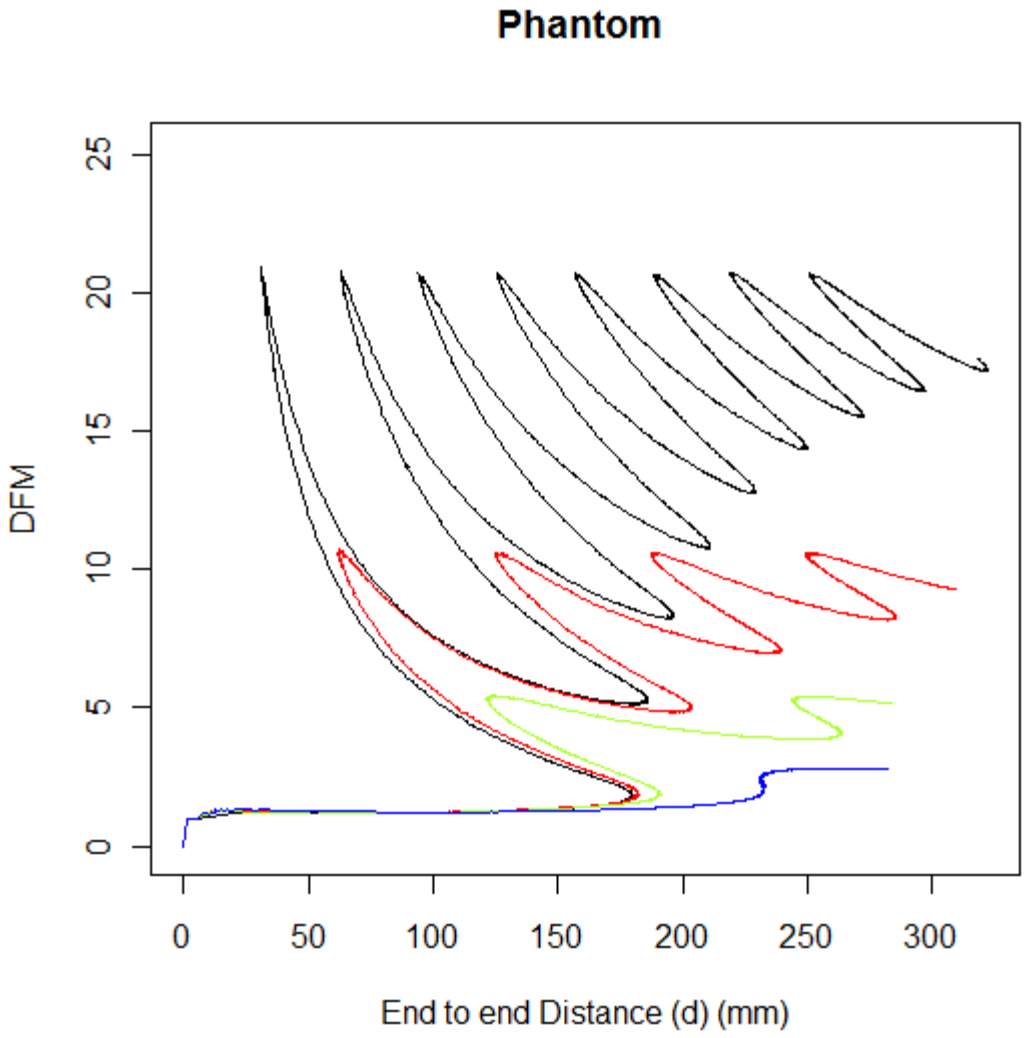
Phantom
DFM
0
5
10
15
20
25
0
50
100
150
200
250
300
End to end Distance (d) (mm)

bottom

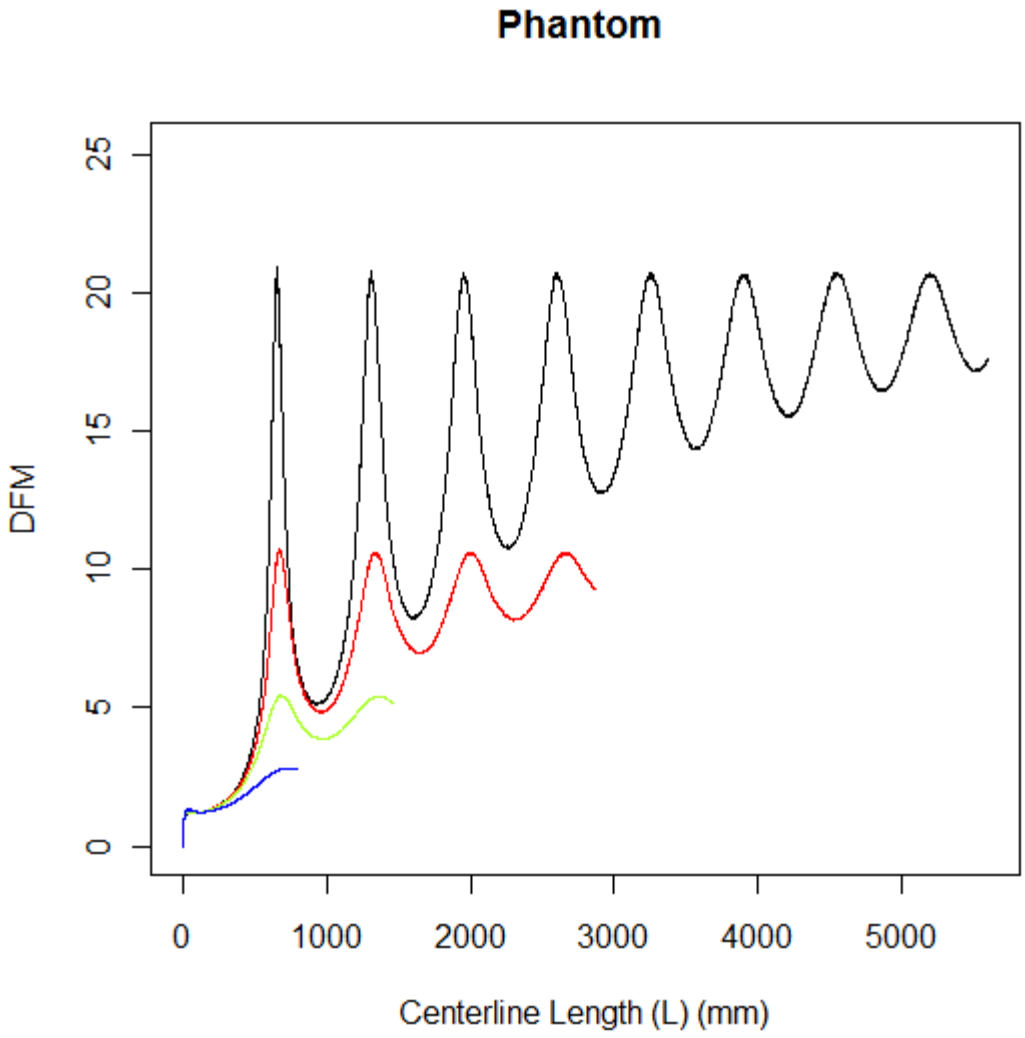

Figure 3.7 continued.

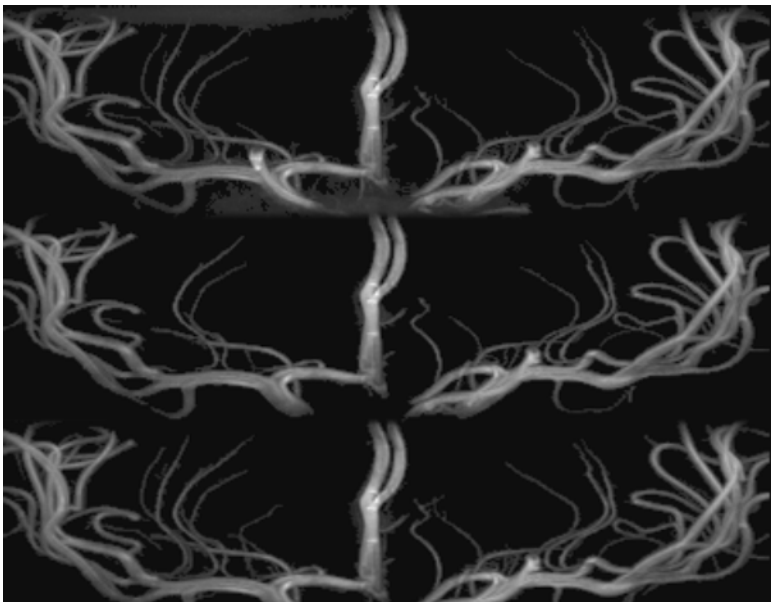

Figure 3.8. Median filtered segmentations. Median filter subtraction segmentations of a 7.0 T NRI image of a hypertensive patient were displayed in maximum intensity projection. (top) Segmentation without the median filter subtraction left background noise in the segmentation. (center) Segmentation with the 5x5 median filter subtraction removed background noise and smaller lenticulostriate arteries (LSA). (bottom) Segmentation with the 11x11 median-filter leaves small amounts of background noise near the larger arteries while leaving the LSAs in the segmentation.

Figure 3.9. Tortuosity and resolution. Comparison of mean tortuosity of the same Korean subjects from NRI with one standard deviation error bars. (top) Left and right ICA tortuosity measurements from higher 0.2x0.2x0.2 mm (0.2 mm) resolutions interpolations of the same images increased compared to 0.4x0.4x0.4 mm (0.4 mm) resolution. (bottom) The mean DFM tortuosity of the 0.2x0.2x0.2 mm (0.2) and 0.23x0.23x0.36 mm (0.23) resolution images were closer together than to the 0.4x0.4x0.4 mm images (0.4).

top

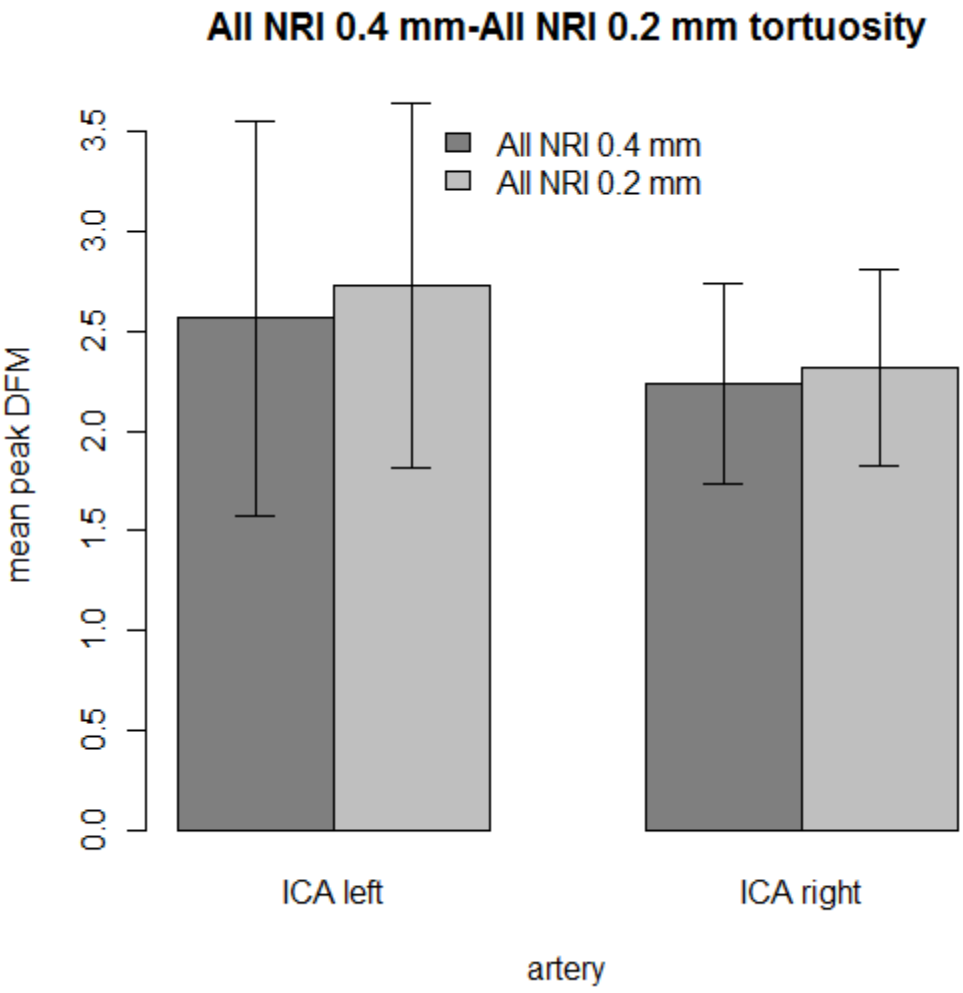
All NRI 0.4 mm-All NRI 0.2 mm tortuosity
All NRI 0.4 mm
All NRI 0.2 mm
mean peak DFM
0.0
0.5
1.0
1.5
2.0
2.5
3.0
3.5
ICA left
ICA right
artery

bottom

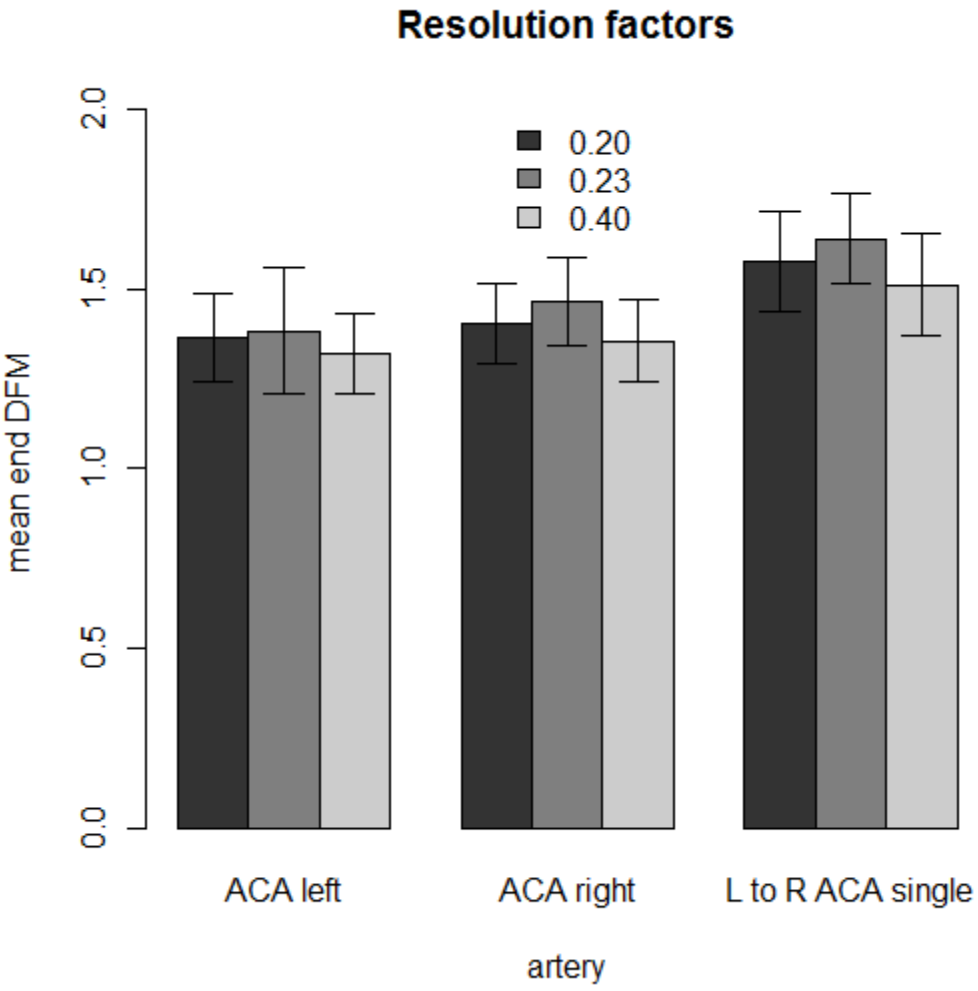

Figure 3.9 continued.

Figure 3.10. Negative control tortuosities. Utah and North Carolina negative (NEG) controls had significantly higher tortuosity than the NRI Korean negative controls: (top) mean end tortuosity measurements, (bottom) mean peak tortuosity measurements.

top

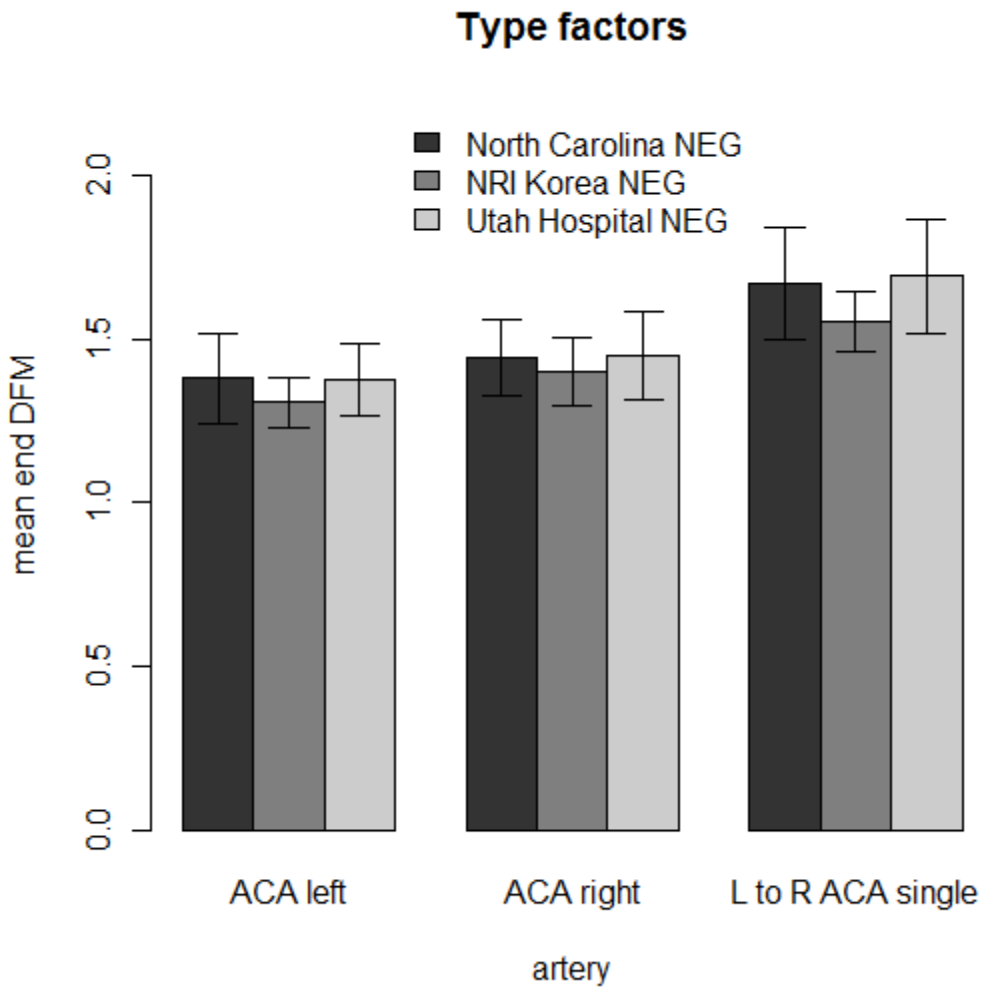
Type factors
North Carolina NEG
NRI Korea NEG
Utah Hospital NEG
mean end DFM
0.0
0.5
1.0
1.5
2.0
ACA left
ACA right
L to R ACA single
artery

bottom

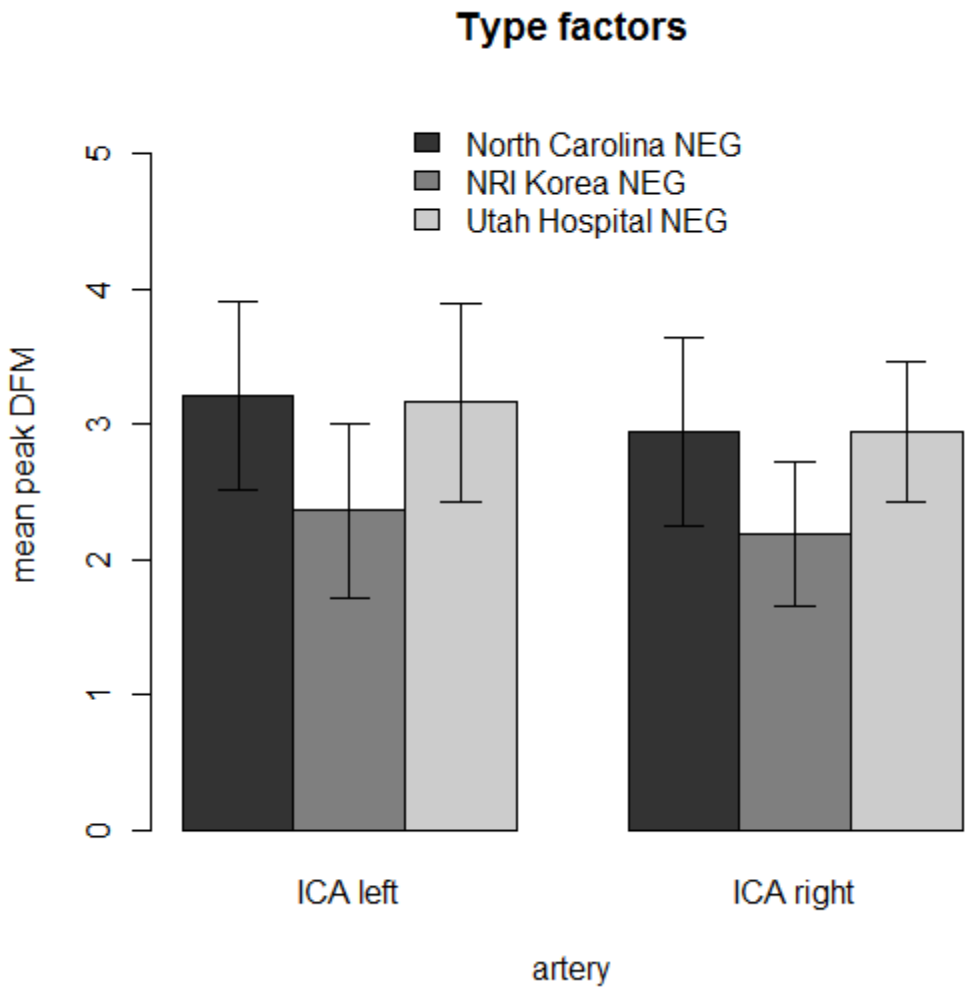

Figure 3.10 continued.

Figure 3.11. Female-male tortuosity. Mean arterial tortuosity comparison with 1 standard deviation error bars between female and male subjects showed no significant differences: (top) mean end DFM and (bottom) mean peak DFM tortuosity measurements.

top

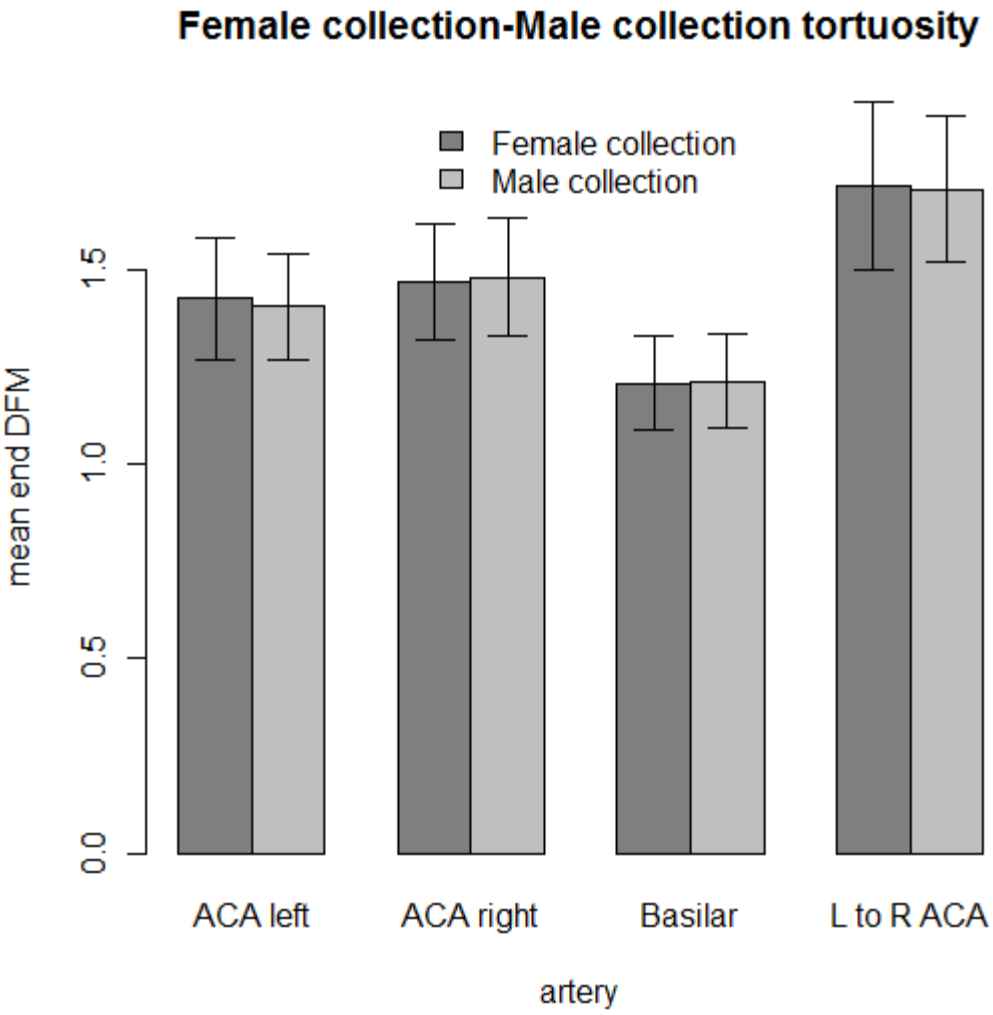
Female collection-Male collection tortuosity
Female collection
Male collection
mean end DFM
0.0
0.5
1.0
1.5
ACA left
ACA right
Basilar
L to R ACA
artery

bottom

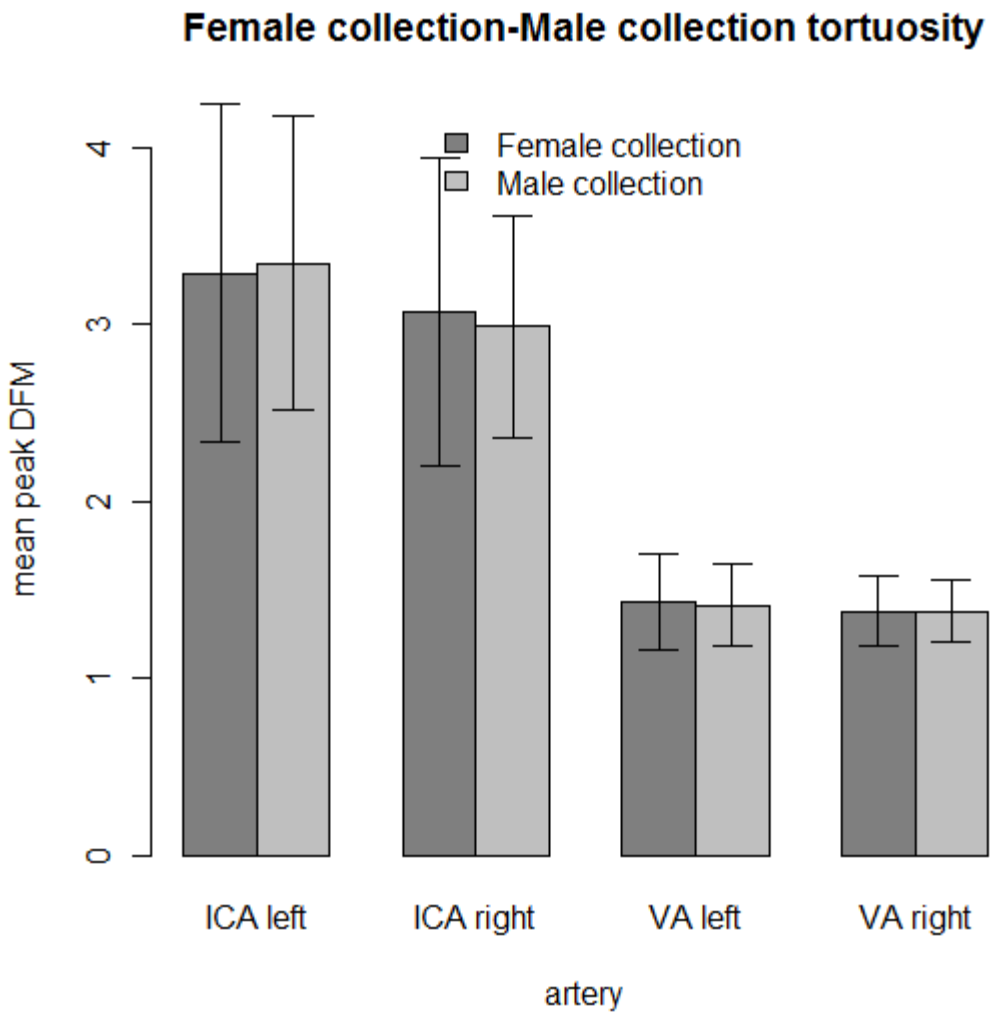

Figure 3.11 continued.

Figure 3.12. NRI Korean tortuosities. NRI Korean negative versus hypertensive (HTN) arterial mean tortuosity comparisons with 1 standard deviation error bars. LSA 1 left was the left most LSA and LSA 1 right was the right most LSA. (top) The figure showed the mean end DFM tortuosity measures. (bottom) The figure showed the mean peak DFM tortuosity measures.

top

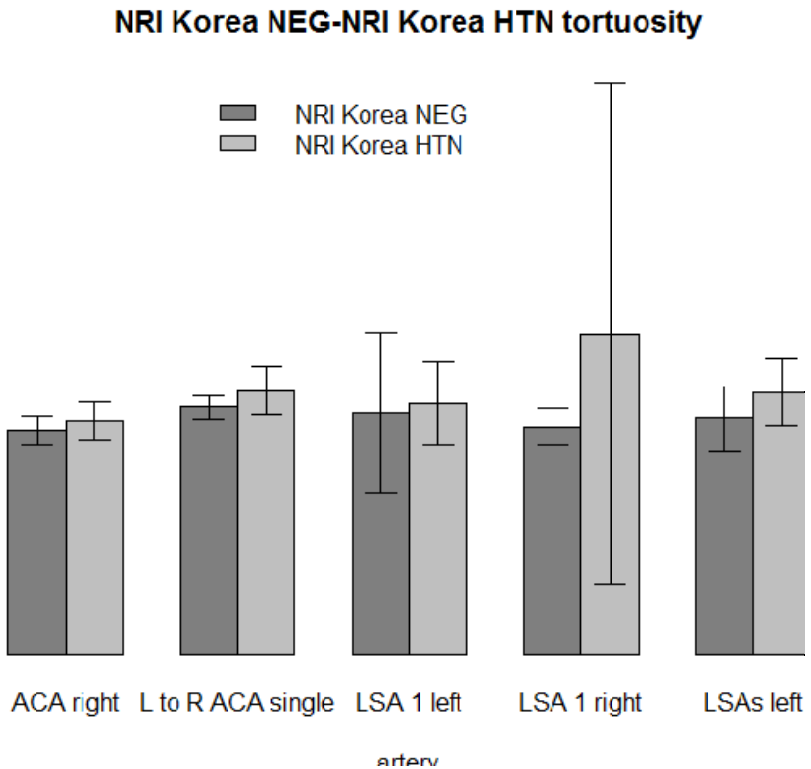
NRI Korea NEG-NRI Korea HTN tortuosity
NRI Korea NEG
NRI Korea HTN
ACA right
L to R ACA single
LSA 1 left
LSA 1 right
LSAs left
artery

bottom

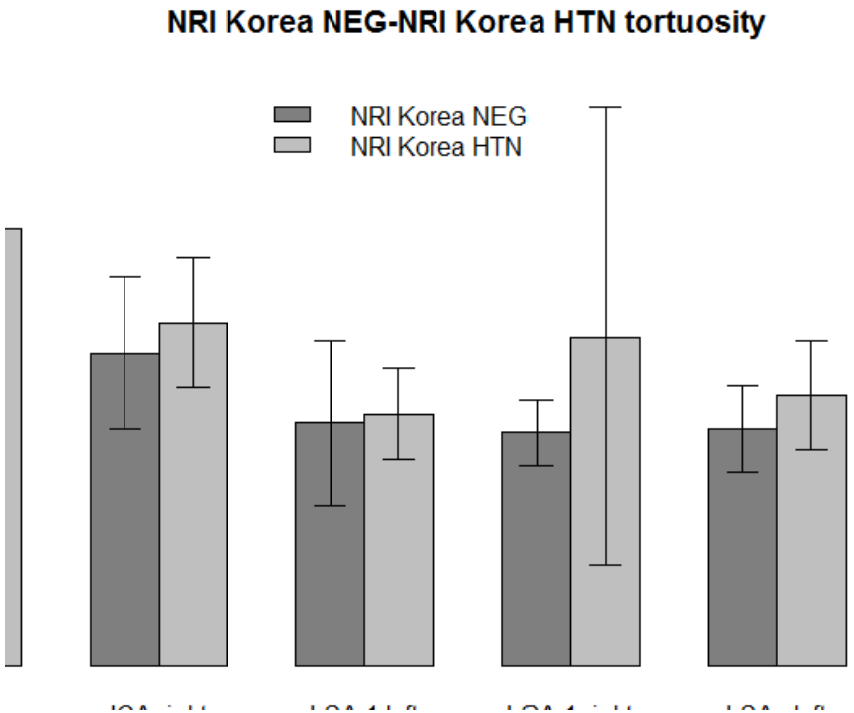

Figure 3.12 continued.

Figure 3.13. Utah hypertensive tortuosity. Comparison of Utah common hypertension (HTN) and Utah hospital negative (NEG) control with 1 standard deviation error bars: (top) mean end DFM tortuosity measures and (bottom) mean peak DFM measures.

top

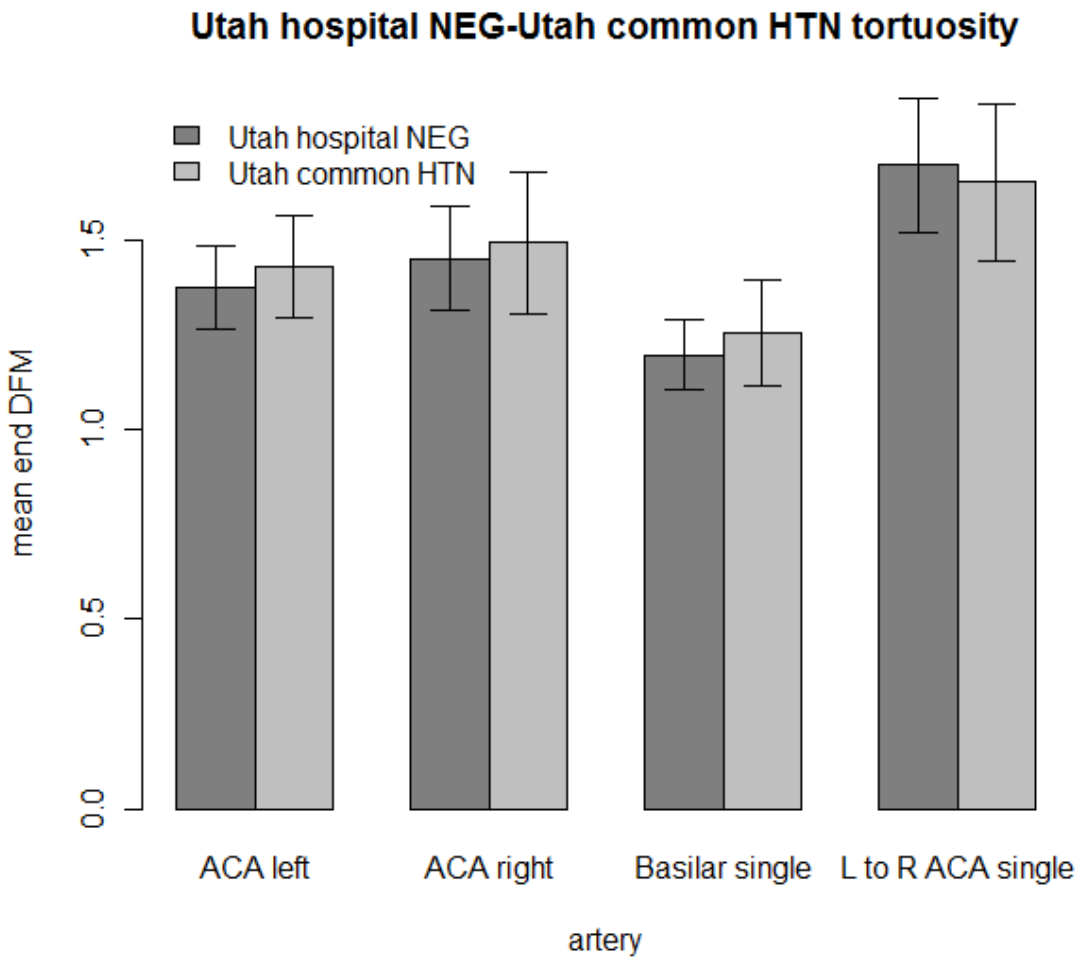
Utah hospital NEG-Utah common HTN tortuosity
Utah hospital NEG
Utah common HTN
mean end DFM
0.0
0.5
1.0
1.5
ACA left
ACA right
Basilar single
L to R ACA single
artery

bottom

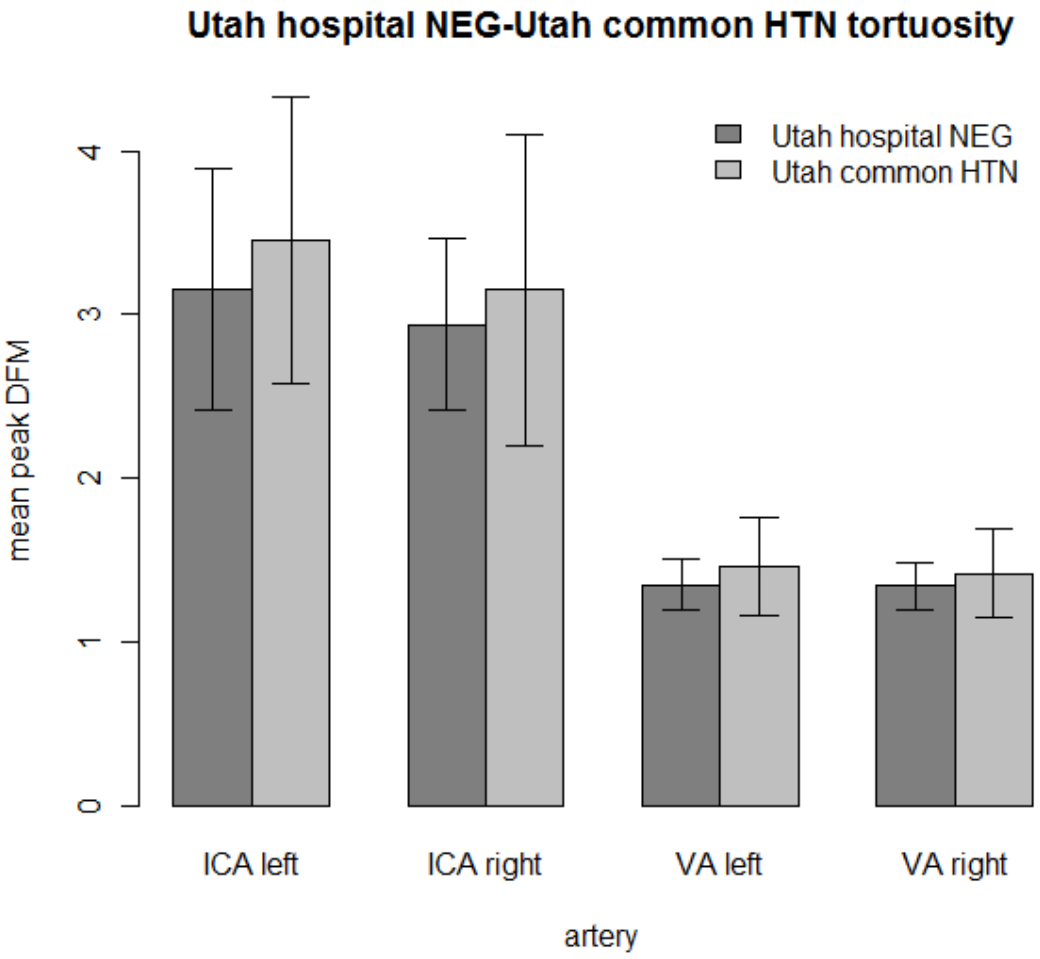

Figure 3.13 continued.

Table 3.1. Tortuosity curve measurement point

Artery	Start	End	Measurement
Left ACA	Left ICA/ACA bifurcation	Acom	End to end
Right ACA	Right ICA/ACA bifurcation	Acom	End to end
Left ACA - Acom - Right ACA	Left ICA/ACA bifurcation	Right ICA/ACA bifurcation	End to end
Basilar	Posterior cerebrals	Vertebral arteries	End to end
Left ICA and Right ICA	ACA/MCA bifurcation	Bottom of slab	Peak
Left and Right VA	Basilar artery	Bottom of slab	Peak
LSA (7 T images)	MCA	Visible end	Peak and end-end

The measurement for each artery is taken from different points on the tortuosity curve of the anterior cerebral artery (ACA), internal carotid artery (ICA), anterior communicating (Acom), vertebral artery (VA), basilar arteries and lenticulostriate artery (LSA). Middle cerebral artery (MCA) bifurcations are used a starting points for some measurements.

Table 3.2. Comparison of algorithm stability and accuracy of comb phantom

Algorithm	Number of trees	Stability	RMSE of Accuracy
COM	6	0.918	0.879
MDFE	6	0.819	0.417
DFE-COM	6	0.905	0.413

The COM cost function shortest paths centerline algorithm was less accurate in the comb phantom than the MDFE cost and DFE-COM cost function algorithms.

Table 3.3. Comparison of algorithm stability and accuracy on 3 branch phantom

Phantom noise	Algorithm	Number of trees	Stability	RMSE of Accuracy
SD-10	COM	3	0.960	0.463
SD-10	MDFE	3	0.930	0.393
SD-10	DFE-COM	3	1.00	0.556
SD-20	COM	3	0.950	0.528
SD-20	MDFE	3	0.946	0.674
SD-20	DFE-COM	3	0.955	0.561

The DFE-COM cost function shortest paths centerline algorithm had similar stability and accuracy to the COM based centerline algorithm. The MDFE cost algorithm accuracy degraded going from standard deviation (SD) 10 to 20 noise.

Table 3.4. Comparison of centerline algorithms on MRA brain images

Algorithm	ICA siphons accurate	Portion ICA siphons correct	Both ICA correct in image	Portion correct images	Mean number of trees	Standard deviation of trees	Mean stability	Standard deviation stability
COM	15/16	0.938	7/8	0.875	37.000	12.352	0.872	0.0459
MDFE	7/16	0.438	1/8	0.125	39.875	13.228	0.673	0.0732
DFE-COM	15/16	0.938	7/8	0.875	38.625	11.439	0.825	0.0434

The COM and DFE-COM cost function shortest paths centerline algorithms calculated the correct centerline in the same number of correct ICA siphons.

Table 3.5. Helix phantom tortuosity

Phantom	Peak Distance Factor Metric	Approximate coils	Peak DFM/2.80 ratio
Pitch 5(2π)	20.95	8	7.48
Pitch 10(2π)	10.76	4	3.84
Pitch 20(2π)	5.45	2	1.95
Pitch 40(2π)	2.80	1	1.00

The peak distance factor metric tortuosity scores are lower with increasing pitch of the three-dimensional helix phantoms.

Table 3.6. Negative control demographics

(-) control	Total	Mean age	Male (%)	Female (%)	White	Asian	Black
NRI Korean	20	47.7	3(15.0)	17 (85.0)	0 (0.00)	20 (100.0)	0 (0.00)
North Carolina	95	42.7	45 (47.4)	50 (52.6)	83 (87.4)	8 (8.4)	4 (4.2)
Utah	45	46.7	23 (51.1)	22 (48.9)	-	-	-

The Korean negative control population was mostly female whereas the North-Carolina and Utah negative control populations where evenly split between females and males.

Table 3.7. Utah retrospective tortuosity comparison

Artery	Negative (N)	Hypertensive (N)	1-sided Wilcoxon	2-sided F Test
Left ACA	43	21	0.0565	+0.232
Right ACA	39	21	0.279	-0.0824
Basilar	42	18	0.0641	+0.0302
L to R ACA	24	11	0.805	+0.501
Left ICA	35	19	0.132	+0.371
Right ICA	36	19	0.366	**+0.00206**
Left VA	36	18	0.283	**+0.00093**
Right VA	35	16	0.297	+0.00174

A (+) indicates increased hypertensive tortuosity and a (-) indicates decreased hypertensive tortuosity.

References

1. Hiroki M, Miyashita K, Oda M: **Tortuosity of the white matter medullary arterioles is related to the severity of hypertension**. *Cerebrovasc Dis* 2002, **13**:242-250.

2. Dobrin PB, Schwarcz TH, Baker WH: **Mechanisms of arterial and aneurysmal tortuosity**. *Surgery* 1988, **104**:568-571.

3. Kang C-K, Park C-A, Lee H, Kim S-H, Park C-W, Kim Y-B, Cho Z-H: **Hypertension correlates with lenticulostriate arteries visualized by 7T magnetic resonance angiography**. *Hypertension* 2009, **54**:1050-1056.

4. Capowski JJ, Kylstra JA, Freedman SF: **A numeric index based on spatial frequency for the tortuosity of retinal vessels and its application to plus disease in retinopathy of prematurity**. *Retina (Philadelphia, Pa.)* 1995, **15**:490-500.

5. Bullitt E, Gerig G, Pizer SM, Lin W, Aylward SR: **Measuring tortuosity of the intracerebral vasculature from MRA images**. *IEEE Trans Med Imaging* 2003, **22**:1163-1171.

6. Lotmar W, Freiburghaus A, Bracher D: **Measurement of vessel tortuosity on fundus photographs**. *Albrecht Von Graefes Arch Klin Exp Ophthalmol* 1979, **211**:49-57.

7. Hart WE, Goldbaum M, Côté B, Kube P, Nelson MR: **Measurement and classification of retinal vascular tortuosity**. *Int J Med Inform* 1999, **53**:239-252.

8. O'Flynn PM, O'Sullivan G, Pandit AS: **Geometric variability of the abdominal aorta and its major peripheral branches**. *Ann Biomed Eng* 2010, **38**:824-840.

9. Dougherty G, Varro J: **A quantitative index for the measurement of the tortuosity of blood vessels**. *Med Eng Phys* 2000, **22**:567-574.

10. O'Flynn PM, O'Sullivan G, Pandit AS: **Methods for three-dimensional geometric characterization of the arterial vasculature**. *Ann Biomed Eng* 2007, **35**:1368-1381.

11. Dijkstra EW: **A note on two problems in connexion with graphs**. *Numerische Mathematik* 1959, **1**:269-271.

12. Zhang L, Chapman BE, Parker DL, Roberts JA, Guo J, Vemuri P, Moon SM, Noo F: **Automatic detection of three-dimensional vascular tree centerlines and bifurcations in high-resolution magnetic resonance angiography**. *Invest Radiol* 2005, **40**:661-71.

13. Jeong E-K, Parker DL, Tsuruda JS, Won J-Y: **Reduction of flow-related signal loss in flow-compensated 3D TOF MR angiography, using variable echo time (3D TOF-VTE)**. *Magn Reson Med* 2002, **48**:667-676.

14. Parker DL, Goodrich KC, Roberts JA, Chapman BE, Jeong E-K, Kim S-E, Tsuruda JS, Katzman GL: **The need for phase-encoding flow compensation in high-resolution intracranial magnetic resonance angiography**. *J Magn Reson Imaging* 2003, **18**:121-127.

15. Aylward SR, Bullitt E: **Initialization, noise, singularities, and scale in height ridge traversal for tubular object centerline extraction**. *IEEE Trans Med Imaging* 2002, **21**:61-75.

16. Parker DL, Chapman BE, Roberts JA, Alexander AL, Tsuruda JS: **Enhanced image detail using continuity in the MIP Z-buffer: applications to magnetic resonance angiography**. *J Magn Reson Imaging* 2000, **11**:378-88.

17. Cormen TH, Leiserson CE, Rivest RL, Stein C: *Introduction to Algorithms, Third Edition*. The MIT Press; 2009.

18. Bullitt E, Reardon DA, Smith JK: **A review of micro- and macrovascular analyses in the assessment of tumor-associated vasculature as visualized by MR**. *Neuroimage* 2007, **37 Suppl 1**:S116-9.

19. Johnson PT, Chen JK, Loeys BL, Dietz HC, Fishman EK: **Loeys-Dietz syndrome: MDCT angiography findings**. *AJR Am J Roentgenol* 2007, **189**:W29-35.

20. Loeys BL, Chen J, Neptune ER, Judge DP, Podowski M, Holm T, Meyers J, Leitch CC, Katsanis N, Sharifi N, Xu FL, Myers LA, Spevak PJ, Cameron DE, De Backer J, Hellemans J, Chen Y, Davis EC, Webb CL, Kress W, Coucke P, Rifkin DB, De Paepe AM, Dietz HC: **A syndrome of altered cardiovascular, craniofacial, neurocognitive and skeletal development caused by mutations in TGFBR1 or TGFBR2**. *Nat. Genet* 2005, **37**:275-281.

21. Bullitt E, Zeng D, Mortamet B, Ghosh A, Aylward SR, Lin W, Marks BL, Smith K: **The effects of healthy aging on intracerebral blood vessels visualized by magnetic resonance angiography**. *Neurobiol Aging* 2010, **31**:290-300.

22. Kang C-K, Park C-W, Han J-Y, Kim S-H, Park C-A, Kim K-N, Hong S-M, Kim Y-B, Lee KH, Cho Z-H: **Imaging and analysis of lenticulostriate arteries using 7.0-Tesla magnetic resonance angiography**. *Magn Reson Med* 2009, **61**:136-144.

23. Cho Z-H, Kang C-K, Han J-Y, Kim S-H, Kim K-N, Hong S-M, Park C-W, Kim Y-B: **Observation of the lenticulostriate arteries in the human brain in vivo using 7.0T MR angiography**. *Stroke* 2008, **39**:1604-1606.

24. Du YP, Parker DL, Davis WL, Cao G: **Reduction of partial-volume artifacts with zero-filled interpolation in three-dimensional MR angiography**. *J Magn Reson Imaging* 1994, **4**:733-741.

25. **R: A language and environment for statistical computing. R Foundation for Statistical Computing, Vienna, Austria. ISBN 3-900051-07-0** [http://www.R-project.org/].

CHAPTER 4

MEDICAL RECORD AND IMAGING EVALUATION TO IDENTIFY ARTERIAL TORTUOSITY PHENOTYPE IN POPULATIONS AT RISK FOR INTRACRANIAL ANEURYSMS

Karl T. Diedrich, MS[1,2], John A. Roberts, PhD[1], Richard H. Schmidt, MD, PhD[3], Lisa A. Cannon Albright, PhD[4,6], Anji T. Yetman, MD[5] and Dennis L. Parker, PhD[1,2]

[1]Utah Center for Advanced Imaging Research, Department of Radiology, University of Utah, 729 Arapeen Drive, Salt Lake City, UT 84108, USA

[2]Department of Biomedical Informatics, University of Utah, 26 South 2000 East Room 5775 HSEB, Salt Lake City, UT 84112

[3]Department of Neurosurgery, University of Utah, Health Science Center, Bldg 550, 5th Floor, 175 N. Medical Drive East, Salt Lake City, UT 84132, USA,

[4]Genetic Epidemiology, Department of Internal Medicine, 391 Chipeta Way, Suite D, Salt Lake City, UT 84108, USA

[5]Department of Pediatrics, Division Of Cardiology, Primary Children's Medical Center, 100 North Mario Capecchi Drive, Salt Lake City, UT 84113, USA

[6]George E. Wallen Department of Veterans Affairs Medical Center, Salt Lake City, Utah

Grant sponsors: Ben B. and Iris M. Margolis Foundation, NLM training grant T15LM007124, and NIH grants: R01-NS-37737 and R01-HL-48223.

Correspondence to: Karl T. Diedrich, Department of Radiology, University of Utah, 729 Arapeen Drive, Salt Lake City, UT 84108, USA. E-mail: Karl.Diedrich@utah.edu Tel.: 1-801-581-3141. Fax: 1-801-585-3592

Abstract

High arterial tortuosity may signify early arterial pathology which may precede development of intracranial aneurysms. We measured arterial tortuosity of intracranial vessels and reviewed the medical records of three groups of patients: with intracranial aneurysms, without aneurysms but at increased clinical risk, and controls without aneurysms or associated risk factors. There was significant but inconsistent evidence of increased arterial tortuosity in aneurysm cases and high-risk cases across different arteries. Medical records review identified that a subset of aneurysm cases carried a diagnosis of Loeys-Dietz syndrome that is often misdiagnosed as Marfan syndrome. We found increased arterial tortuosity in the Loeys-Dietz syndrome cases. A combination of medical record screening for Marfan syndrome or Loeys-Dietz symptoms such as aneurysms and evaluation of arterial tortuosity by a curve of scores from medical images may identify previously undiagnosed cases of Loeys-Dietz syndrome.

Key words: Aneurysm, MRA, Loeys-Dietz, tortuosity.

Introduction

There are autopsy reports of increased arterial and arteriolar tortuosity in aged subjects with hypertension and aneurysms[1]. While hypertension is considered a risk factor for developing intracranial aneurysms, the clinical importance of the greater arteriolar tortuosity noted on autopsy[2,3], to the development of intracranial aneurysms is not clear. The small arterioles visible on dissection at autopsy are not readily visible using current medical imaging techniques but Time of Flight-Magnetic Resonance

Angiography (TOF-MRA) imaging has been used to assess arterial tortuosity of larger vessels. Increased tortuosity of arteries visible in MRA has been shown to correlate with aging[4], exercise level[5], tumors[6], retinal pathology[7] and certain genetic syndromes[8,9]. The degree of arterial tortuosity can be quantitatively measured from MRA images with the Distance Factor Metric (DFM) tortuosity score that is calculated by measuring the length (L) along the centerline of the artery divided by the straight line distance (d) from two points[10-13]. In the conventional use of DFM, only two points are selected per artery, producing a single tortuosity score or zero-dimensional measure of tortuosity (DFM_0) for the artery. Whether used for intersubject or intrasubject measurements, DFM_0 is constrained by the underlying data: images may not consistently contain the same two well defined points along the artery, images may contain different lengths of the artery, and the tortuosity may be sensitively dependent upon the selection of the two points. This study expands the conventional use of DFM to create a one dimensional tortuosity score curve (DFM_c) displaying local tortuosity information along a vessel. The DFM_c is then used to assess the relationship between arterial tortuosity of larger vessels seen in TOF-MRA with the development of intracranial aneurysms.

This study utilized medical imaging to assess the degree of arterial tortuosity noted in patients with a clinical history of aneurysm, or predisposition to aneurysm[14-16], recorded in the medical record. We were specifically interested in determining whether or not patients with familial aneurysms, nonfamilial aneurysms or in high-risk subjects without any history of aneurysms as yet, have abnormally increased arterial tortuosity.

Materials and methods

Source images

All TOF-MRA images were collected from the University of Utah Medical Center in Salt Lake City, UT, U.S.A. with approval from the University of Utah Institutional Review Board. A negative control population was collected retrospectively from clinical TOF-MRA head images taken within the last three years. The negative control population included patients with a diagnosis of headache or trigeminal neuralgia who underwent TOF-MRA head imaging but in whom no vascular disease (aneurysmal dilation or stenosis) was identified in the radiology report and in whom no risk factors for vascular disease were noted in the medical record (including: arterial disease, atrial fibrillation, diabetes, hypertension, and acquired heart disease). The control group also had cancer or genetic syndromes screened out. The high-risk group and aneurysm group were comprised of cases previously identified in a study on high (two-fold) familial risk of intracranial aneurysms[14] and from patients treated for aneurysms at the University of Utah Medical Center. The images were clinical scans at a range of resolutions. Lower resolution images were interpolated to higher resolution with a sinc interpolation for comparison to higher resolution images.

Arterial tortuosity measurement summary

The arterial tortuosity measures were made by segmenting the arteries from the background, generating a centerline through the segmentation and selecting two end points along the centerline of the artery measured. The Distance Factor Metric (DFM)

tortuosity score is calculated by measuring *L* along the centerline of the artery divided by *d* from the starting point[10-13]. Rather than compute a single DFM tortuosity score per artery (DFM_0), the *L/d* tortuosity was calculated at every point on the centerline with respect to the starting point to create a one-dimensional tortuosity score curve (DFM_c). A tortuosity measure based upon a smoothed centerline was also calculated by averaging the position of each centerline point with its two adjacent neighbors to compute a smoothed version of *L* (L_s) and the smoothed tortuosity score, $DFM_{cs} = L_s/d$. After computing the DFM_c curve, an optimal point along each artery was selected for reporting DFM. In this study, the final DFM tortuosity scores were taken as either the peak DFM value of the DFM_c curve or the end DFM value of the DFM_c curve when the arterial centerline left the image volume and no defined second end existed.

Tools

The segmentation and tortuosity measurement tools were implemented as ImageJ plugins[17-19]. The measured centerline positions and subject information were stored in a MySQL relational database available at http://www.mysql.com/. Plotting of tortuosity score curves, box and whiskers plot comparisons, and statistical tests were conducted with R[20], connected directly to MySQL using MySQL Open Database Connectivity (ODBC), using statistical methods previously described[21].

Statistical tests

Statistical significance was set at the $\alpha = 0.05$ level and Bonferroni corrected to $\beta = \alpha/n$, where n is the number of tests in a set. The significance level was adjusted instead of the P-value of statistical tests to show raw test results. The Wilcoxon rank sum test was used throughout the study as it does not require normality of the underlying populations and is resistant to outliers. F-test and T-test were used with larger sample set sizes where normality can be assumed by the central limit theorem. The F-test tested for differences in variation of tortuosity scores and the T-test was used to confirm the Wilcoxon rank sum test results.

Segmentation

The TOF-MRA images (Figure 4.1) were segmented using a Maximum Intensity Projection (MIP) Z-buffer segmentation[22](Figure 4.2).

Centerlines

The centerlines were generated from the segmentations using a centerline algorithm based on algorithms previously described[23,24] with a cost function modification where the Center of Mass (COM) voxel costs were multiplied by the Distance From Edge (DFE) values of the voxels to give higher weights to voxels at the center of the segmented arteries. Due to the limitations of intensity based segmentation, the internal carotid artery often segments as a closed loop structure, presenting two apparent paths

during centerline extraction. The ability of the centerline algorithm employed here to extract the proper geometry of the internal carotid artery was validated using the centerline stability metric previously developed[24].

Artery selection and tortuosity measurement

Arteries were selected for tortuosity measurement by first selecting two end-points of a centerline through the segmentation of the desired artery. Unlike a traditional DFM_0 measurement, in this case it was only necessary that one of the two end-points be a common anatomical location for each measured artery, generally a bifurcation shared by all subjects. The second end-point could either be another common anatomical location or the point at which the artery of interest exited the image volume. The three-dimensional segmented artery image was colored to assist the user in selecting centerline segments for tortuosity measurement. The red centerlines connect at the bifurcations which are indicated by green dots (Figure 4.3). A separate random color was assigned to each centerline to cause a color change at the bifurcations to aid the user when locating bifurcations.

Visual correlation

The quantitative DFM tortuosity scores were correlated to visual tortuosity rankings. A total of 315 subjects including negative controls and vascular disease cases from multiple ongoing tortuosity studies were ordered highest to lowest by the DFM_{cs}

based tortuosity score at the end of the basilar artery where it bifurcates into the left and right vertebral arteries (Figure 4.4). Every 11^{th} subject beginning with the subject with the highest tortuosity score was selected to obtain a subset of 25 subjects with a wide range of arterial tortuosities. For each of the 25 subjects, MIP images were computed in the transverse plane with 18 rotations taken every 10 degrees (MIP images at 180 degrees difference are the same) showing the entire brain vasculature imaged. These images were shown to a group of five volunteer medical imaging researchers who ranked the basilar arteries highest (rank 1) to lowest (rank 25) in tortuosity. The volunteers were advised to compare images pairwise and were given no time limit or consistency training to avoid bias[25]. The means of the human rankings were compared by Spearman rank correlation to the rank determined by the quantitative end of artery DFM_c and DFM_{cs} scores of the basilar artery.

Tortuosity was measured for multiple arteries in the image slabs. The arteries measured were the left and right anterior cerebral arteries (ACA), across the left ACA through the anterior communicating artery (Acomm) to the right ACA; the basilar artery, the left and right internal carotid arteries (ICA) from the ICA bifurcation with the middle cerebral artery (MCA) and ACA to the lower end of the image slab, and the left and right vertebral arteries from the bifurcation with the basilar artery to the lower end of the image slab. The tortuosity score was taken from the tortuosity score curve at the end of the curve for the basilar, anterior cerebral artery (ACA) and ACA-anterior communicating artery (AComm)-ACA measurements. The tortuosity score was taken at the peak of the curve for the internal carotid artery (ICA) and vertebral artery (VA)

measurements because the end of these arteries varied depending on the depth of the image slabs.

Results

The end DFM_c had higher correlation to the mean visual rankings than the smoothed end DFM_{cs} tortuosity score. The end DFM_c had a 0.72 Spearmen rank correlation coefficient ($P < 0.0001$) (Figure 4.5) with the mean visual ranking while the end DFM_{cs} correlation was 0.67 ($P = 0.00025$). The mean of the correlation between all pairs of human visual ranks was 0.88 ± 0.048. Both the end DFM_c and end DFM_{cs} quantitative tortuosity scores were calculated and used in statistical tests of differences between the test cases and negative controls. Only the end DFM_c scores are reported due to better correlation with the mean visual ranks and due to the fact that the results of the tests differed little with the two measurements.

We measured the arterial tortuosity of eight arteries between the intracranial aneurysm group and the negative control population. The difference in tortuosity was tested at the $\beta = \alpha/n = 0.05/8 = 0.00625$ level to account for testing eight arteries. Only the left ACA tortuosity measurement was noted to be significantly greater in the aneurysm cohort (indicated in bold in Table 1). While the aneurysm group had greater tortuosity in all eight arteries (indicated with a + in the “Difference of means” column in Table 4.1), the difference from the control group was not statistically significant for the other seven arteries. The aneurysm cases also had significantly higher variance in right ICA and left VA than the negative controls. Of note, the aneurysm population was

approximately eight years older than the negative control group. As the data set was obtained from existing images taken for other purposes, the images often included different arteries and in some instances image quality prevented measurement of some arteries resulting in different number (N) of measurements for each artery recorded in Table 4.1.

The negative controls who were < 40 or > 55 years produced no statistically significant differences at $\beta = 0.00625$ with the 1-sided Wilcoxon signed rank test (used exclusively due to the small sample size) across the eight arteries. Three arteries had higher tortuosity in the > 55 population (+) and five arteries had higher tortuosity in the < 40 population (-) (Table 4.2).

The familial aneurysm cases had significantly higher tortuosity of the left ACA than the negative controls at the $\beta = 0.00625$ level. Eight of the eight arteries had higher arterial tortuosity (+) in the familial aneurysm cases than the negative controls but seven were not significant (Table 4.3).

A manual medical record chart review of the highest scoring tortuosity measures of intracranial aneurysms cases revealed one diagnosis of Marfan syndrome (without genetic confirmation), two of Loeys-Dietz syndrome (LDS) (with genetic confirmation) and eight high familial risk intracranial aneurysm (IA) cases. Before 2005 LDS cases were often diagnosed with Marfan syndrome making diagnosis without genetic confirmation ambiguous. Further chart review demonstrated that the one patient diagnosed with Marfan syndrome did not meet clinical criteria for this diagnosis raising the question of a misdiagnosis in a patient with a TGF-β LDS causing mutation.

Additional LDS cases were collected to test for an increase in arterial tortuosity in LDS patients. Six syndromic cases including five genetically confirmed Loeys-Dietz syndrome (LDS) and the one unconfirmed clinical Marfan diagnosis had significantly greater tortuosity of the basilar and the left VA at the $\beta = 0.00625$ level (Table 4.4). Examples of tortuous vertebral arteries of Loeys-Dietz patients are shown in Figure 4.6 and Figure 4.7. For comparison Figure 4.8 shows a low tortuosity VA and Figure 4.9 shows the tortuosity curves of those arteries. These patients had greater tortuosity of eight of eight arteries measured. Two of the confirmed LDS patients and the one unconfirmed clinical Marfan syndrome cases had intracranial aneurysms and the other three confirmed LDS cases did not have aneurysms.

Patients with nonfamilial aneurysms and without an underlying genetic syndrome had significantly greater left ACA arterial tortuosity by t-test than negative controls. Tortuosity measures were greater in seven of eight arteries. Nonfamilial aneurysm cases also had significantly higher variation in the left and right ICAs (Table 4.5).
High intracranial aneurysm risk family case subjects without aneurysms themselves had significantly higher arterial tortuosity in the left ICA and significantly higher variance in the left VA. These case subjects had higher tortuosity in seven of the eight arteries measured (Table 4.6).

Discussion

Measurement of arterial tortuosity is a newly developed technique that may prove to be of clinical utility in identifying diseased vasculature. The DFM_c tortuosity score

curve and associated peak and end measurements described herein appear to provide more information than the traditional single value DFM_0 tortuosity score. By selecting the peak tortuosity score from a curve of values defined from a single end-point, we obtain a meaningful tortuosity value from arteries with only one well-defined end-point in a medical image. The original DFM_0 method required selection of the same two defined end-points for all arteries to be compared, making it unusable when there was only one defined point as is often the case with the long ICA and vertebral arteries. Furthermore, analysis of the DFM_c tortuosity score curves shows that the tortuosity score may vary significantly along the vessel as indicated in Figure 4.9. Thus, by considering only two particular end-points per artery, the traditional tortuosity analysis may both greatly underestimate the peak value and be sensitively dependent on end-point selection.

Using the methods described herein, we have been able to demonstrate a significantly greater degree of arterial tortuosity in patients with connective tissue syndromes who are known to be at risk for intracranial aneurysms[8,27]. Nonsyndromic patients with intracranial aneurysms, subjects with high familial risk of intracranial aneurysms, relatives of high-risk aneurysm cases, and patients with nonfamilial aneurysms had inconsistently higher arterial tortuosity than negative controls. The overlap in tortuosity scores between high familial risk intracranial aneurysm cases with negative controls indicates high-risk subjects with normal tortuosity scores can develop intracranial aneurysms. There was also no significant difference between high-risk subjects with aneurysms compared to relatives without aneurysms. In contrast, arterial

tortuosity in patients with Loeys-Dietz syndrome, a disorder associated with the presence of intracranial aneurysms, was significantly different than in negative controls.

Age has been shown to mildly increase tortuosity in healthy populations[4]. The age comparisons conducted here showed no significant tortuosity increase due to age. It is thus unlikely that the age difference between the aneurysm and negative control populations accounted for the differences in tortuosity.

The human visual rankings correlation to each other was closer than to the quantitative tortuosity score based ranks. This phenomenon of humans correlating with each other better than a computer score has been previously described[25]. The human rankers may be using information seen in the surrounding image, or alternatively there could be a bias in the projections shown to the rankers causing their ranks to cluster together.

The results of this study provide evidence that tortuosity measurements may be able to assist in characterizing specific nonnormal states and may even assist in distinguishing between patients with Loeys-Dietz syndrome and Marfan syndrome. Loeys-Dietz syndrome is a more aggressive disorder associated with visible arterial tortuosity and aneurysms throughout the arterial tree[8,27] where many but not all affected patients will go on to develop cerebral aneurysms. In light of the fact that Loeys-Dietz syndrome was only determined to be a unique clinical entity apart from Marfan syndrome within the last decade[28], many affected patients may still carry the diagnosis of Marfan syndrome. Marfan syndrome is caused by a mutation in the *FBN*1 gene that encodes for the glycoprotein fibrillin[29]. Patients are typically followed with only echocardiographic

imaging of the ascending aorta as the remainder of the arterial vessels are not thought to be at significant risk of aneurysm formation. In contrast, Loeys-Dietz syndrome is caused by mutations in the *TGFBRI* and *TGFBRII* genes which encode for receptors for the cytokine TGF-β[27,28]. By collecting and measuring arterial tortuosity data in patients with either clinical diagnosis we hope to be able to distinguish between the two disorders and determine which patients with Loeys-Dietz syndrome are at greatest risk for cerebral aneurysm formation. Initial review of arterial tortuosity in Loeys-Dietz patients demonstrated that these patients may have the greatest increase in tortuosity in the extra-cranial vertebral arteries which are typically more caudal than the sections analyzed in this study. Assessment of both the cervicocephalic vessels and intracranial vessels may prove valuable [30].

This study demonstrates the potential to combine medical record screening with automated image analysis to screen patient data. The study started with familial and nonfamilial intracranial aneurysm cases and discovered the syndromic patients during the course of the research. The method for measuring arterial tortuosity is now semi-automated. Future development will further automate the tortuosity measurement. Automated medical record screening systems already exist. In this case the two methods of medical record and image screening could be combined to look for patients with diagnosis of Marfan syndrome or other Loeys-Dietz symptoms and high arterial tortuosity to identify undiagnosed Loeys-Dietz patients in electronic medical records.

Acknowledgments

We greatly appreciate the help of the staff at the Utah Center for Advanced Imaging Research in supporting this research. The research including database collection supported by grants from the Ben B. and Iris M. Margolis Foundation, NLM training grant T15LM007124, and NIH grants: R01-NS-37737 and R01-HL-48223.

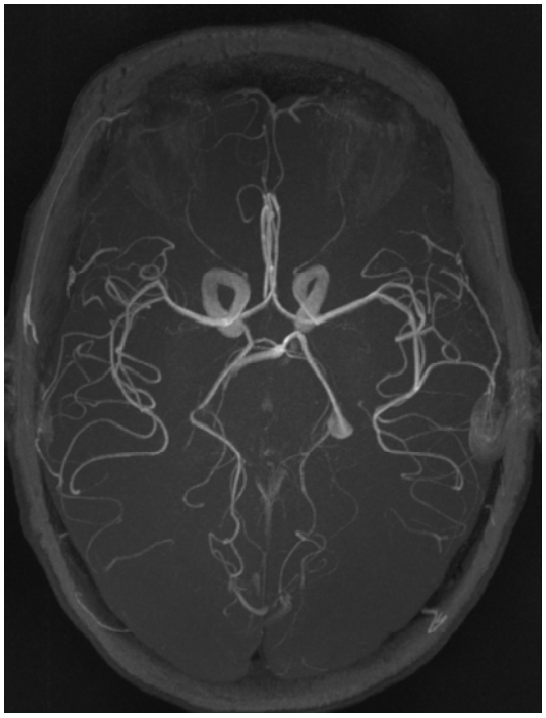

Figure 4.1. Time of Flight-Magnetic Resonance Angiography (TOF-MRA) medical image shown in Maximum Intensity Projection (MIP).

Figure 4.2. Segmented arteries from TOF-MRA with color changes at bifurcations in shaded surface display[26].

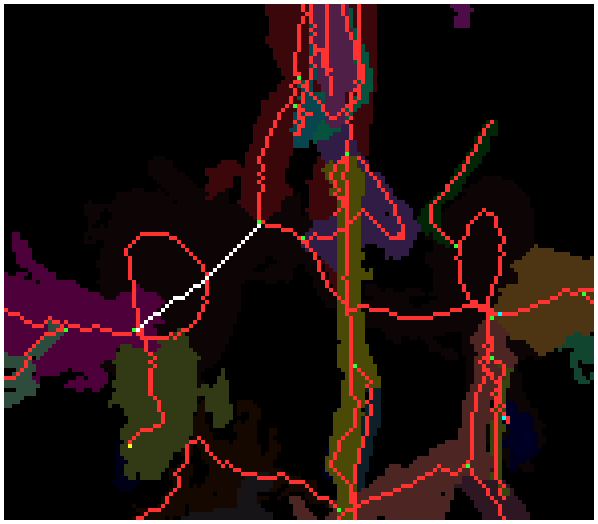

Figure 4.3. Selection in white of anterior cerebral artery (ACA) shown in Maximum Intensity Projection (MIP).

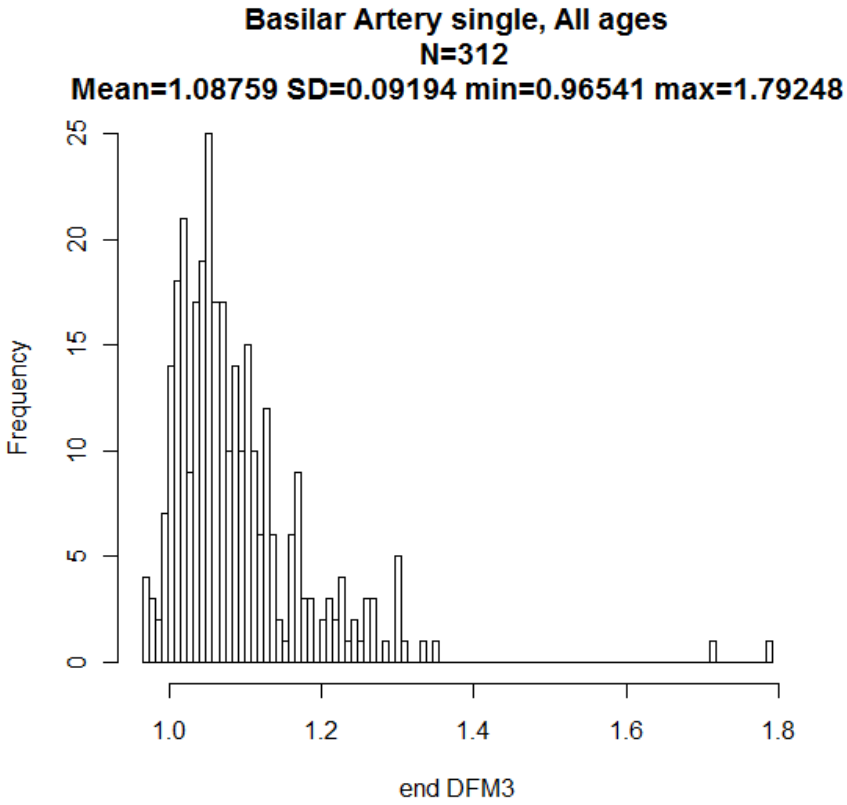

Figure 4.4. Histogram of basilar artery end DFM_{cs} (labeled end DFM3) tortuosity scores.

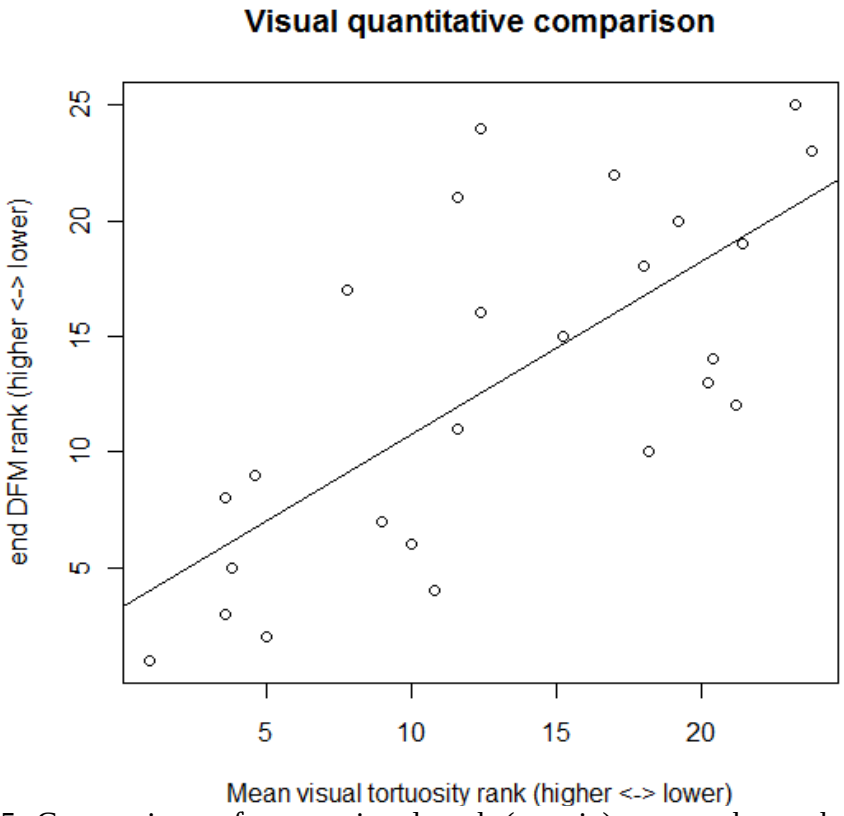

Figure 4.5. Comparison of mean visual rank (x-axis) versus the rank of the end DFM_c tortuosity score (y-axis) of the basilar artery with regression line (0.72 Spearmen rank correlation coefficient).

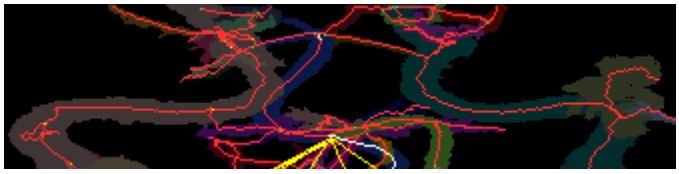

Figure 4.6. Distance Factor Metric (DFM) = Length (*L*) / distance (*d*) tortuosity scores of the left vertebral artery of a suspected Loeys-Dietz patient selected in white. Yellow lines show *d* and progressive steps. This subject had the maximum left vertebral artery tortuosity of the aneurysm subjects. Black line in Figure 4.9.

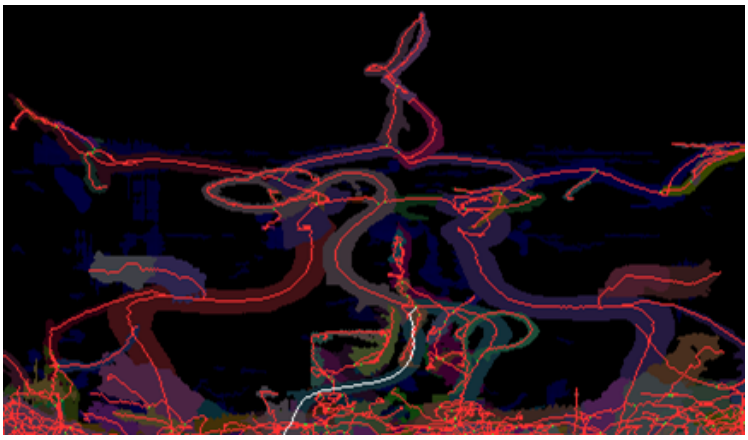

Figure 4.7. Loeys-Dietz syndrome intracranial aneurysm subject with median tortuosity among aneurysm case subjects of the left vertebral artery and high tortuosity of the basilar artery. Green line in Figure 4.9.

Figure 4.8. Nonfamilial intracranial aneurysm subject with low tortuosity left vertebral artery. Red line in Figure 4.9.

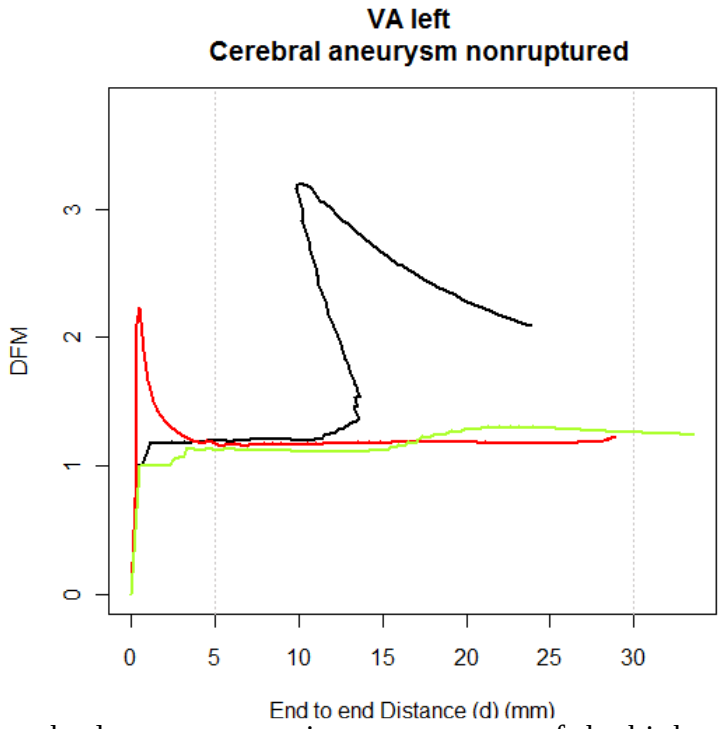

Figure 4.9. Vertebral artery tortuosity score curves of the highest peak tortuosity score (black line), median tortuosity score (green line) and low tortuosity score (red line). The peak score is taken between the dotted lines to avoid small variations causing spikes when the lengths L and d are short and subject to noise and before vertebral arteries twist around the first cervical vertebrae.

Table 4.1. Aneurysm cases versus negative control tortuosity comparisons

Artery	Measurement	Negative (N)	Mean DFM ± SD	Mean age	Aneurysm (N)	Mean DFM ± SD	Mean age	% Difference of means	1-sided Wilcoxon Test	2-sided F Test
Left ACA	End	43	1.375± 0.110	46.674	64	1.462± 0.141	54.822	+6.3	**0.00054**	0.088
Right ACA	End	39	1.450± 0.135	45.641	65	1.497± 0.159	54.099	+3.2	0.079	0.289
L-R ACA	End	24	1.695± 0.176	41.375	32	1.715± 0.184	52.944	+1.2	0.320	0.819
Basilar	End	42	1.196± 0.093	46.333	56	1.216± 0.105	53.900	+1.7	0.157	0.408
Left ICA	Peak	35	3.157± 0.737	48.343	55	3.522± 1.053	55.831	+11.5	0.097	0.028
Right ICA	Peak	36	2.941± 0.521	47.056	51	3.341± 1.075	55.940	+13.6	0.078	**<0.0001**
Left VA	Peak	36	1.350± 0.155	46.000	49	1.448± 0.318	54.105	+7.3	0.043	**<0.0001**
Right VA	Peak	35	1.340± 0.142	46.400	50	1.352± 0.176	53.850	+0.85	0.431	0.196

Table 4.2. Negative control age comparisons

Artery	Measurement	Under 40 (N)	Mean DFM ± SD	Mean age	Over 55 (N)	Mean DFM ± SD	Mean age	% Difference of means	1-sided Wilcoxon Test
Left ACA	End	16	1.379±0.120	27.938	16	1.368±0.106	65.562	-0.80	0.566
Right ACA	End	16	1.449±0.142	27.938	15	1.435±0.148	64.333	-1.0	0.727
L-R ACA	End	12	1.699±0.150	26.000	6	1.708±0.223	68.000	+0.51	0.625
Basilar	End	16	1.176±0.089	27.938	15	1.166±0.075	65.867	-0.88	0.673
Left ICA	Peak	12	2.796±0.556	28.250	14	3.438±0.699	66.500	+23.0	0.013
Right ICA	Peak	13	2.849±0.380	28.000	14	3.010±0.534	64.857	+5.7	0.229
Left VA	Peak	14	1.339±0.154	28.357	13	1.318±0.104	64.615	-0.46	0.215
Right VA	Peak	14	1.324±0.180	29.286	13	1.312±0.097	65.231	-2.1	0.547

Table 4.3. Familial aneurysm cases versus negative control tortuosity comparisons

Artery	Familial Aneurysm (N)	Mean DFM ± SD	Mean age	% Difference of means	1-sided Wilcoxon Test
Left ACA	23	1.474±0.127	58.610	+7.2	**0.00063**
Right ACA	22	1.535±0.136	56.250	+5.8	0.019
L-R ACA	12	1.708±0.168	55.067	+0.82	0.389
Basilar	18	1.217±0.096	57.571	+1.8	0.183
Left ICA	20	3.345±0.685	59.654	+6.0	0.220
Right ICA	20	3.171±0.843	58.568	+7.8	0.268
Left VA	21	1.432±0.234	58.603	+6.1	0.087
Right VA	22	1.366±0.184	58.485	+2.0	0.357

Table 4.4. Loeys-Dietz/Marfan syndrome cases versus negative control tortuosity comparisons

Artery	Syndrome (N)	Mean DFM ± SD	Mean age	% Difference of means	1-sided Wilcoxon Test
Left ACA	5	1.407±0.168	19.200	+2.3	0.474
Right ACA	4	1.704±0.448	20.000	+17.5	0.131
L-R ACA	4	2.143±0.709	20.000	+26.5	0.063
Basilar	5	1.443±0.300	25.300	+20.6	**0.0045**
Left ICA	3	3.361±0.388	26.833	+6.5	0.323
Right ICA	3	3.263±0.688	26.833	+10.9	0.216
Left VA	6	1.931±0.652	23.750	+43.1	**0.00043**
Right VA	6	1.511±0.297	23.750	+12.7	0.051

Table 4.5. Nonfamilial aneurysms versus negative control tortuosity comparisons

Artery	Nonfamilial aneurysm (N) Mean DFM ± SD		Mean age	% Difference of means	1-sided Wilcoxon Test	2-sided F Test	1-sided T Test
Left ACA	42	1.454±0.150	54.751	+5.7	0.0069	0.047	**0.0036**
Right ACA	44	1.471±0.167	54.953	+1.4	0.330	0.193	0.270
L-R ACA	19	1.725±0.202	54.596	+1.8	0.310	0.526	0.303
Basilar	38	1.207±0.107	55.789	+0.89	0.328	0.360	0.318
Left ICA	34	3.577±1.262	54.710	+13.3	0.165	**0.0024**	0.049
Right ICA	30	3.450±1.216	56.703	+17.3	0.059	**<0.0001**	0.020
Left VA	27	1.395±0.155	54.333	+3.3	0.105	0.980	0.128
Right VA	27	1.317±0.097	53.790	-1.7	0.562	0.050	0.773

Table 4.6. High-risk relative cases versus negative control tortuosity comparisons

Artery	High-risk (N)	Mean DFM ± SD	Mean age	% Difference of	1-sided Wilcoxon Test	2-sided F Test	1-sided T test
Left ACA	53	1.423±0.111	46.604	+3.5	0.012	0.921	0.019
Right ACA	52	1.494±0.131	46.577	+3.0	0.076	0.805	0.061
L-R ACA	25	1.706±0.149	50.000	+0.68	0.241	0.421	0.403
Basilar	31	1.182±0.082	47.387	-1.2	0.724	0.490	0.724
Left ICA	37	3.850±1.053	46.405	+21.9	**0.0023**	0.039	**0.00092**
Right ICA	36	3.330±0.781	45.639	+13.2	0.028	0.019	0.0079
Left VA	47	1.423±0.254	48.234	+5.4	0.087	**0.0030**	0.054
Right VA	43	1.404±0.189	47.302	+4.8	0.086	0.087	0.046

References

1. Dobrin PB, Schwarcz TH, Baker WH. Mechanisms of arterial and aneurysmal tortuosity. Surgery. 1988 Sep;104(3):568-571.

2. Spangler KM, Challa VR, Moody DM, Bell MA. Arteriolar tortuosity of the white matter in aging and hypertension. A microradiographic study. J. Neuropathol. Exp. Neurol. 1994 Jan;53(1):22-26.

3. Hiroki M, Miyashita K, Oda M. Tortuosity of the white matter medullary arterioles is related to the severity of hypertension. Cerebrovasc. Dis. 2002;13(4):242-250.

4. Bullitt E, Zeng D, Mortamet B, Ghosh A, Aylward SR, Lin W, et al. The effects of healthy aging on intracerebral blood vessels visualized by magnetic resonance angiography. Neurobiol. Aging [Internet]. 2008 May 7 [cited 2009 Nov 20];Available from: http://www.ncbi.nlm.nih.gov/pubmed/18471935

5. Bullitt E, Rahman FN, Smith JK, Kim E, Zeng D, Katz LM, et al. The Effect of Exercise on the Cerebral Vasculature of Healthy Aged Subjects as Visualized by MR Angiography. AJNR Am J Neuroradiol [Internet]. 2009 Jul 9 [cited 2009 Oct 2];Available from: http://www.ncbi.nlm.nih.gov/pubmed/19589885

6. Bullitt E, Reardon DA, Smith JK. A review of micro- and macrovascular analyses in the assessment of tumor-associated vasculature as visualized by MR. Neuroimage. 2007;37 Suppl 1:S116-9.

7. Dougherty G, Johnson MJ, Wiers MD. Measurement of retinal vascular tortuosity and its application to retinal pathologies. Med Biol Eng Comput. 2010 Jan;48(1):87-95.

8. Johnson PT, Chen JK, Loeys BL, Dietz HC, Fishman EK. Loeys-Dietz syndrome: MDCT angiography findings. AJR Am J Roentgenol. 2007 Jul;189(1):W29-35.

9. Ritelli M, Drera B, Vicchio M, Puppini G, Biban P, Pilati M, et al. Arterial tortuosity syndrome in two Italian paediatric patients. Orphanet J Rare Dis. 2009;4:20.

10. O'Flynn P, O-Sullivan G, Pandit A. Methods for three-dimensional geometric characterization of the arterial vasculature. [cited 2009 Mar 9];Available from: http://www.ncbi.nlm.nih.gov/pubmed/17431787?ordinalpos=8&itool=EntrezSystem2.PEntrez.Pubmed.Pubmed_ResultsPanel.Pubmed_DefaultReportPanel.Pubmed_RVDocSum

11. Bullitt E, Gerig G, Pizer SM, Lin W, Aylward SR. Measuring tortuosity of the intracerebral vasculature from MRA images. IEEE Trans Med Imaging. 2003 Sep;22(9):1163-1171.

12. Capowski JJ, Kylstra JA, Freedman SF. A numeric index based on spatial frequency for the tortuosity of retinal vessels and its application to plus disease in retinopathy of prematurity. Retina (Philadelphia, Pa.). 1995;15(6):490-500.

13. Lotmar W, Freiburghaus A, Bracher D. Measurement of vessel tortuosity on fundus photographs. Albrecht Von Graefes Arch Klin Exp Ophthalmol. 1979 Jul 2;211(1):49-57.

14. Farnham JM, Camp NJ, Neuhausen SL, Tsuruda J, Parker D, MacDonald J, et al. Confirmation of chromosome 7q11 locus for predisposition to intracranial aneurysm. Hum Genet. 2004 Feb;114(3):250-5.

15. Cannon Albright LA, Camp NJ, Farnham JM, MacDonald J, Abtin K, Rowe KG. A genealogical assessment of heritable predisposition to aneurysms. J. Neurosurg. 2003 Oct;99(4):637-643.

16. Berthelemy-Okazaki N, Zhao Y, Yang Z, Camp NJ, Farnham J, Parker D, et al. Examination of ELN as a candidate gene in the Utah intracranial aneurysm pedigrees. Stroke. 2005 Jun;36(6):1283-1284.

17. Burger W, Burge MJ. Digital Image Processing: An Algorithmic Introduction using Java: [Internet]. [cited 2009 Mar 7]. Available from: http://www.imagingbook.com/

18. Abramoff MD, Magelhaes PJ, Ram SJ. Image Processing with ImageJ. Biophotonics International. 2004;11(7):36-42.

19. Rasband W. ImageJ, U.S. National Institutes of Health, Bethesda, Maryland, USA [Internet]. 1997 2005 [cited 2009 Mar 8];Available from: http://rsb.info.nih.gov/ij/

20. R Development Core Team. R: A language and environment for statistical computing. R Foundation for Statistical Computing, Vienna, Austria. ISBN 3-900051-07-0 [Internet]. 2009 [cited 2010 Apr 23];Available from: http://www.R-project.org/

21. Crawley MJ. The R Book. 1st ed. Wiley; 2007.

22. Parker DL, Chapman BE, Roberts JA, Alexander AL, Tsuruda JS. Enhanced image detail using continuity in the MIP Z-buffer: applications to magnetic resonance angiography. J Magn Reson Imaging. 2000 Apr;11(4):378-88.

23. Zhang L, Chapman BE, Parker DL, Roberts JA, Guo J, Vemuri P, et al. Automatic detection of three-dimensional vascular tree centerlines and bifurcations in high-resolution magnetic resonance angiography. Invest Radiol. 2005 Oct;40(10):661-71.

24. Diedrich KT, Roberts JA, Schmidt RH, Parker DL. Comparing performance of centerline algorithms for quantitative assessment of brain vascular anatomy. Under review.

25. Dougherty G, Johnson MJ. Clinical validation of three-dimensional tortuosity metrics based on the minimum curvature of approximating polynomial splines. Med Eng Phys. 2008 Mar;30(2):190-198.

26. Phong BT. Illumination for computer generated pictures. Commun. ACM. 1975;18(6):311-317.

27. Loeys BL, Schwarze U, Holm T, Callewaert BL, Thomas GH, Pannu H, et al. Aneurysm syndromes caused by mutations in the TGF-beta receptor. N. Engl. J. Med. 2006 Aug 24;355(8):788-798.

28. Loeys BL, Chen J, Neptune ER, Judge DP, Podowski M, Holm T, et al. A syndrome of altered cardiovascular, craniofacial, neurocognitive and skeletal development caused by mutations in TGFBR1 or TGFBR2. Nat. Genet. 2005 Mar;37(3):275-281.

29. Dietz HC, Cutting GR, Pyeritz RE, Maslen CL, Sakai LY, Corson GM, et al. Marfan syndrome caused by a recurrent de novo missense mutation in the fibrillin gene. Nature. 1991 Jul 25;352(6333):337-339.

30. Yetman AT, Beroukhim RS, Ivy DD, Manchester D. Importance of the clinical recognition of Loeys-Dietz syndrome in the neonatal period. Pediatrics. 2007 May;119(5):e1199-1202.

CHAPTER 5

CONCLUSION

Developing the use of arterial tortuosity

Arterial tortuosity has been associated with a limited number of vascular diseases and is used clinically in only in limited diseases. As described in the introduction visual tortuosity is used to assist in diagnosing LDS and quantitative tortuosity is used in diagnosing retinal diseases. Other vascular diseases have been associated with increased arterial tortuosity but are not used clinically due to lack of evidence of associations and clinical tools to quantitatively measure arterial tortuosity.

This research developed a system for measuring and comparing arterial tortuosity between populations. The system was able to detect increases in arterial tortuosity in a hypertensive population and in clinical images of LDS patients versus negative controls. While the measure detects differences at the population level the means of the Korean hypertensive and LDS samples fell within one standard deviation of the corresponding negative controls. This prevents the measure from differentiating individual clinical samples. The ability to detect the population differences demonstrates the ability of the tortuosity measurement system to measure increases in tortuosity at the population level since there is no gold standard to compare against for arterial tortuosity measurements. The increases in tortuosity seen with hypertension and LDS provide evidence of

increased arterial tortuosity in those populations. Due to limited sample size and diversity more samples of both hypertensives and LDS patients are needed to confirm the increases in arterial tortuosity associated with these diseases. The tortuosity measurement system developed here can be used for future studies on more hypertensive, LDS and other disease populations.

Validation of arterial tortuosity measurement

The tortuosity measure combining the DFE-COM based centerline algorithm and DFM tortuosity curve was able to detect tortuosity differences in a prospective hypertensive population and in the clinical LDS population demonstrating the methods ability. There is no gold standard for measuring arterial tortuosity. As demonstrated in the visual tortuosity ranking experiment in Chapter 4, visual tortuosity scoring has intra-ranker variability (0.88±0.048 Spearman rank coefficient). A repeat of the ranking experiment with neurosurgeons had a lower 0.65±0.13 Spearman rank coefficient between rankers demonstrating the instability of visual tortuosity scoring. As mentioned earlier the SOAM measurement detected changes due to aging while the ICM did not [1] and ICM measurement detected changes due to exercise while the SOAM did not [2]. There is no single gold standard way to measure tortuosity in all situations. The tortuosity measurement method used depends on the disease.

LDS patient tortuosity is characterized by type I tortuosity with long gently curving arteries without abrupt changes in slope of the centerline. The DFM measurement was successful in detecting type I tortuosity [3]. The integral of second

derivative tortuosity measure was designed to detect abrupt changes in slope of the centerline making it less than ideal for detecting the type I tortuosity displayed in LDS patients. The DFE-COM based centerline DFM tortuosity curve measurement used here was able to detect increased tortuosity in LDS patients.

Which type of tortuosity is displayed by hypertensives was less clear, but the DFE-COM based centerline DFM curve consistently measured arterial tortuosity across several arteries. Additional measurement methods were not needed. Other diseases that cause abrupt changes in direction of the centerline may require different tortuosity detection methods.

The hypertension study was able to make quantitative measurements of the smaller LSA arteries due to the use of 7.0 T MRA and the ability of the ZBS algorithm [4, 5] to segment the LSAs. Segmentation of arteries is a difficult ongoing area of research [6]. Therefore the hypertension study pushed down the lower diameter limit of what arteries can be measured from MRA images in living patients. Hypertension showed greater change in tortuosity of the narrow diameter LSAs than other larger diameter arteries. Smaller diameter arteries may increase (or decrease) in response to disease progression or treatment sooner than larger diameter arteries. Thus tortuosity measurements on high field angiography may be a way to measure disease and treatment effects earlier.

Quantitative image phenotype measurement of genotype

The tortuosity measurement of LDS patients is a quantitative measurement of the phenotypic effect of the LDS genotype. LDS can be caused by mutations in at least two different genes, TGFBR1 and TGFBR2 and there are multiple mutations within those genes [7-9]. The different mutations may have different levels of effect [10] that may be quantifiable by the tortuosity measurement. Quantitative measurement of arterial tortuosity could also be used to identify the presence of genetic modifiers that are secondary genes that alter the phenotypic expression of the primary mutations. Genetic modifiers are thought to explain the range of severity of MFS [11]. Quantitative phenotype measurement is also important for epigenetics research into how environmental factors alter genotypes expression [12]. Epigenetic research studies the changes in gene expression (phenotype) not due to changes in DNA [13]. Quantitation is important when attributing part of a phenotype to genotype and part to environmental factors or an interaction of the two [12].

Flexible analysis system

The tortuosity measurement and group comparison system developed stored data for reanalysis with new algorithms. The system included a relational database for storing data such as the centerline voxel positions and subject information. Tortuosity measurements were calculated on the fly for comparison between groups. This allowed reanalysis of the data with different algorithms. The intracranial aneurysm analysis tried an alternative centerline smoothing algorithm that had little effect on the results. The

storing of the centerline points allows for future development of smoothing algorithms on the centerlines. Calculation of tortuosity on the fly allows new tortuosity measurement algorithms as necessary. This tortuosity measurement system also handles measurement of many different arteries. The system was first developed on the basilar, anterior cerebral arteries (ACA), internal carotid arteries (ICA) and vertebral arteries (VA). Then the study on hypertension added the lenticulostriate arteries (LSA) and the system was able to detect an increase in LSA tortuosity in a hypertensive population compared to the corresponding negative control. The system was designed for reanalysis accumulated data, newly added data and new arteries with the same or new analysis methods.

The data storage and on the fly tortuosity measurement were important for analysis of existing data and new clinical data. The database enabled reanalysis when new subject data were added to existing diagnosis groups. The storage of diagnostic and demographic data makes creation of new groups to answer questions that arise from previous experiments simple. An example of this was when the Korean negative control group, which was predominantly female, had significantly lower arterial tortuosity than two other control groups. The system developed here was able to easily compare groups of females versus males to find out sex did not show any significant effect on arterial tortuosity. The database allowed iterative asking and answering of questions.

Value of quantitative measurement

The quantitative measurement of tortuosity is useful for determining the difference between groups, changes in tortuosity over time and can be used in automated

screening of medical images. The experiments comparing the quantitative measure to human tortuosity scores had the people rank images according to arterial tortuosity. Ranking was used instead of having the person assign a numeric score because as the person sees new images they re-evaluate previous scores. A person is also unlikely to keep scores consistent when following a single patient over years. The quantitative tortuosity measure was partially automated in this study. The user only had to select the artery centerline ends. Work on automated centerline selection is underway. Artery characteristics such as diameter length and position are being used to automatically select the arteries. Automated tortuosity measurements could eventually be added to radiologic systems.

Secondary use of image data

Clinical images provide a huge repository to study the effects of numerous vascular diseases on artery morphology. Up to now, studies on quantitative arterial tortuosity have imaged cases and controls under the same conditions. Clinical images are obtained on different machines at different resolutions. This research measured tortuosity of the same subjects at different resolutions to measure the effect of resolution on tortuosity in the hypertension experiment. Knowing the resolution effect allows comparison of clinical images taken at different resolutions. In the Korean hypertension experiment doubling the resolution from 0.4 x 0.4 x0.4 mm to 0.2 x 0.2 x 0.2 mm increased the tortuosity measurement 4.2±1.3% across five artery measurements. The increase in LDS syndrome arterial tortuosity ranged from 2.3% to 43.1% with a less than

15% increase in resolution of the LDS subjects versus the negative controls therefor resolution does not account for the increase in LDS arterial tortuosity. The use of clinical images will allow testing of arterial tortuosity of a variety of vascular diseases not commonly associated with increased visual tortuosity.

Future work

Arterial tortuosity in hypertension

The system of reuse of existing images makes possible more measurements of hypertensive populations that are needed to determine in hypertension correlates with increased arterial tortuosity. The hypertension experiment measured increased arterial tortuosity in one prospective Korean sample and did not detect a difference in the clinical Utah population. Future experiments could measure arterial tortuosity prospectively in additional hypertensive populations. Hypertensive patients could also be followed over time to determine if arterial tortuosity increases with progression of the disease or if tortuosity decreases with treatments lowering blood pressures. Repeated microvessel imaging of hypertensive patients before and after treatment showed some early indication of changes in microvessels [14]. It is not yet known if arteries lower tortuosity in response to treatment with anti-hypertensive medication. The tortuosity measurement tools developed and validated here can provide methods to study hypertension over broad populations.

Arterial tortuosity in LDS

High arterial tortuosity is one of the distinguishing characteristics between LDS and the more common Marfan syndrome (MFS) caused by the mutations in the FBN1 gene; but clinically the two diseases' tortuosities are only distinguished qualitatively [7, 8]. Future research plans include measuring MFS patient tortuosity for comparison to LDS patients to determine if quantitative tortuosity screening can aid in identifying LDS patients misdiagnosed with MFS. LDS is caused by mutations in either the TGFBR1 or TGFBR2 genes [7]. The LDS patients in the intracranial aneurysm study here only had TGFBR2 mutations [9] but all LDS patients are known for increased tortuosity. The TGFBR1 and TGDFBR2 mutations show little phenotypic differences [15]. It is not known if one type has more tortuosity than the other. Quantitative tortuosity measurements between TGFBR1 and TGFBR2 mutation patients could determine if there is a difference.

Weakened arterial walls are a proposed cause of both arterial tortuosity and aneurysms [16]. Under this hypothesis arterial tortuosity would increase with age and correlate with aneurysm development. LDS is a genetic disease often diagnosed in pediatric patients that will be followed over time, once again showing the importance of distinguishing LDS from MFS patients that are not typically reimaged outside of the aortic arch area [9]. The high arterial tortuosity is seen in young patients but it is not known if arterial tortuosity increases over time. By obtaining images of the same patients taken over years quantitative arterial tortuosity measurements could be used to determine if arterial tortuosity increases over time. Due to the high rate of aneurysms in LDS

patients, quantitative tortuosity measurement could also be used to look for correlations between high or increasing arterial tortuosity and development of intracranial aneurysms.

MFS is not known to increase arterial tortuosity and it only raises the risk of aortic arch aneurysms. LDS increases tortuosity in head and neck arteries and raises aneurysm risk in the aortic arch and other arteries. The FBN1 and TGFBR1 and TGFBR2 proteins are all in the TGF-β signaling pathway but the difference in tortuosity and locations of aneurysms signals some difference in disease mechanism.

Quantitative measurement of LDS patient arterial tortuosity could potentially be used to monitor new treatments. It is possible treatment prevents normal increases in LDS patients or even decreases tortuosity, but these hypotheses need testing. The FDA approved TGFβ activity inhibiting antihypertensive drug Losartan is being tested in MFS patients and clinicians are using it to treat LDS patients [17]. MFS and LDS both show signs of TGF-β signaling pathway hyperactivity [17]. More is known about the MFS disease pathway than LDS disease.

MFS has a range for disease severity. MFS may be a dominant negative mutation in some of the most severe cases where the heterozygous FBN1 mutated gene product dimerizes with the healthy gene product[18]. The MFS genetic cause FBN1 is part and modulates the TGFβ signaling pathway [18]. The MFS mouse model homozygous mgΔ mice for MFS showed increased TGFβ in lung tissue [18]. These mice were successfully treated with TGFβ neutralizing antibodies demonstrating the role the TGFβ hyperactivity in MFS.

LDS mutations affect TGFBR1 or TGFBR2 in the TGFβ signaling pathway. LDS is a mutation of TGFβ I or II receptor but results in increased TGFβ activity possibly due to a gain of function mutation or by triggering unproductive compensatory events since the receptor is less active [7, 19]. An LDS patient was known to have a duplication of the TGFBR1 gene adding further evidence of a gain of mutation function [10].

The screening of images can be combined with medical record screening to identify undiagnosed LDS cases. Diagnoses of MFS or Ehlers-Danlos syndrome along with high arterial tortuosity are potential LDS cases. A diagnosis of an Arnold-Chiari malformation along with high arterial tortuosity is another flag for LDS. In LDS patients 13.3% of 30 developed Arnold-Chiari malformations [8]. This study identified a patient with an Arnold-Chiari malformation and high-tortuosity (third highest left VA tortuosity). Arnold-Chiari malformation is rare, 1 in 1280 [20]. Because high tortuosity is also rare, the combination of two rare events could be an undiagnosed case of LDS. Future advances in automated arterial tortuosity measurement along with electronic medical record system screening could automate identification the rare LDS disease that clinicians will not be actively looking for due to its rarity.

Quantitative phenotypes

Quantitation of phenotypes is necessary for epigenetic research. Due to rapidly dropping DNA sequencing costs there will be more genotype information on patients in the future and genotype data may become part of the standard medical record [12]. It will

be useful to measure the genotypic effects in medical images. Tortuosity is one example of measurement; there will be more in the future.

New technologies in automated DNA sequencing are making whole genome sequencing drop rapidly in time and price [12, 21]. There has been a 14,000-fold price decrease in DNA sequencing from 1999 to 2009 [22]. Exome sequencing that sequences only the protein coding part of the DNA, which is only around 1% of the human genome, is an even faster and less expensive alternative [21, 23]. There will soon be DNA sequence information available for individual patients usable for research and personalized medical treatment [12, 24].

Genetic variation data are becoming more common but due to the lack of information on the function of genetic variation, genomics has had little impact on clinical medicine [22, 25]. Determining function from genotype is an open ended project [22]. Personalized medicine depends on an understanding of genetic and environmental factors [22]. The next challenge in genomics, as sequence data become an inexpensive commodity, is in linking genetic variation to physiology and disease phenotypes [24]. Medical imaging has the potential to measure phenotypes before they develop into clinical disease and has the potential to separate similar clinical phenotypes such as MFS from LDS and its subtypes.

Contribution to the field of bioinformatics

Medical informatics is “the study, invention, and implementation of structures and algorithms to improve communication, understanding and algorithms to improve

communication, understanding, and management of medical information" [26]. The components of medical informatics are 1) signal processing, 2) database design, 3) decision making, 4) modeling and simulation, 5) optimizing interfaces between human and machine. This research involved signal processing of medical images and database design to allow comparison of subject tortuosity on many factors such as disease, age, sex and resolution of the image. By focusing on making secondary use of medical images this research will help enable reusing and combining data sets together to analyze tortuosity in arteries and diseases not studied before. This study also began a new line of research combining image processing, medical record analysis and genotype analysis to assist decision making.

Summary

The DFE-COM centerline DFM curve tortuosity measurement system detected increased arterial tortuosity with hypertension and LDS validating the measurement method in these diseases. The tortuosity measure can be used to further study arterial tortuosity in hypertensive and LDS patients. Further study of hypertension could determine if tortuosity increases with progression of the disease. Quantitative tortuosity measurement is a potential method to distinguish LDS from related genetic syndromes. The quantitative measurement of phenotypes in medical images is a potential tool for determining the effects of genetic variation.

References

1. Bullitt E, Zeng D, Mortamet B, Ghosh A, Aylward SR, Lin W, Marks BL, Smith K: **The effects of healthy aging on intracerebral blood vessels visualized by magnetic resonance angiography**. *Neurobiol Aging* 2010, **31**:290-300.

2. Bullitt E, Rahman FN, Smith JK, Kim E, Zeng D, Katz LM, Marks BL: **The Effect of Exercise on the Cerebral Vasculature of Healthy Aged Subjects as Visualized by MR Angiography**. *AJNR Am J Neuroradiol* 2009.

3. Bullitt E, Gerig G, Pizer SM, Lin W, Aylward SR: **Measuring tortuosity of the intracerebral vasculature from MRA images**. *IEEE Trans Med Imaging* 2003, **22**:1163-1171.

4. Chapman BE, Stapelton JO, Parker DL: **Intracranial vessel segmentation from time-of-flight MRA using pre-processing of the MIP Z-buffer: accuracy of the ZBS algorithm**. *Med Image Anal* 2004, **8**:113-26.

5. Parker DL, Chapman BE, Roberts JA, Alexander AL, Tsuruda JS: **Enhanced image detail using continuity in the MIP Z-buffer: applications to magnetic resonance angiography**. *J Magn Reson Imaging* 2000, **11**:378-88.

6. Suri JS, Liu K, Reden L, Laxminarayan S: **A review on MR vascular image processing: skeleton versus nonskeleton approaches: part II**. *IEEE Trans Inf Technol Biomed* 2002, **6**:338-350.

7. Loeys BL, Chen J, Neptune ER, Judge DP, Podowski M, Holm T, Meyers J, Leitch CC, Katsanis N, Sharifi N, Xu FL, Myers LA, Spevak PJ, Cameron DE, De Backer J, Hellemans J, Chen Y, Davis EC, Webb CL, Kress W, Coucke P, Rifkin DB, De Paepe AM, Dietz HC: **A syndrome of altered cardiovascular, craniofacial, neurocognitive and skeletal development caused by mutations in TGFBR1 or TGFBR2**. *Nat Genet* 2005, **37**:275-281.

8. Loeys BL, Schwarze U, Holm T, Callewaert BL, Thomas GH, Pannu H, De Backer JF, Oswald GL, Symoens S, Manouvrier S, Roberts AE, Faravelli F, Greco MA, Pyeritz RE, Milewicz DM, Coucke PJ, Cameron DE, Braverman AC, Byers PH, De Paepe AM, Dietz HC: **Aneurysm syndromes caused by mutations in the TGF-beta receptor**. *N Engl J Med* 2006, **355**:788-798.

9. Yetman AT, Beroukhim RS, Ivy DD, Manchester D: **Importance of the clinical recognition of Loeys-Dietz syndrome in the neonatal period**. *Pediatrics* 2007, **119**:e1199-1202.

10. Breckpot J, Budts W, De Zegher F, Vermeesch JR, Devriendt K: **Duplication of the TGFBR1 gene causes features of Loeys-Dietz syndrome**. *Eur J Med Genet* 2010, **53**:408-410.

11. Ramirez F, Dietz HC: **Marfan syndrome: from molecular pathogenesis to clinical treatment**. *Curr Opin Genet Dev* 2007, **17**:252-258.

12. Marian AJ: **Medical DNA sequencing**. *Curr. Opin. Cardiol* 2011, **26**:175-180.

13. Jiang Y-H, Bressler J, Beaudet AL: **Epigenetics and human disease**. *Annu Rev Genomics Hum Genet* 2004, **5**:479-510.

14. Kang C-K, Park C-A, Lee H, Kim S-H, Park C-W, Kim Y-B, Cho Z-H: **Hypertension correlates with lenticulostriate arteries visualized by 7T magnetic resonance angiography**. *Hypertension* 2009, **54**:1050-1056.

15. **Loeys-Dietz Syndrome** [http://www.ncbi.nlm.nih.gov/books/NBK1133/].

16. Dobrin PB, Schwarcz TH, Baker WH: **Mechanisms of arterial and aneurysmal tortuosity**. *Surgery* 1988, **104**:568-571.

17. Choo JTL, Tan TH, Lai AHM, Wong KY: **Loeys-Dietz syndrome: a Marfan-like syndrome associated with aggressive vasculopathy**. *Singapore Med J* 2009, **50**:e353-357.

18. Pereira L, Andrikopoulos K, Tian J, Lee SY, Keene DR, Ono R, Reinhardt DP, Sakai LY, Biery NJ, Bunton T, Dietz HC, Ramirez F: **Targetting of the gene encoding fibrillin-1 recapitulates the vascular aspect of Marfan syndrome**. *Nat Genet* 1997, **17**:218-222.

19. Mizuguchi T, Collod-Beroud G, Akiyama T, Abifadel M, Harada N, Morisaki T, Allard D, Varret M, Claustres M, Morisaki H, Ihara M, Kinoshita A, Yoshiura K-ichiro, Junien C, Kajii T, Jondeau G, Ohta T, Kishino T, Furukawa Y, Nakamura Y, Niikawa N, Boileau C, Matsumoto N: **Heterozygous TGFBR2 mutations in Marfan syndrome**. *Nat Genet* 2004, **36**:855-860.

20. Speer M, Enterline D, Mehltretter L, Hammock P, Joseph J, Dickerson M, Ellenbogen R, Milhorat T, Hauser M, George T: **Review Article: Chiari Type I Malformation with or Without Syringomyelia: Prevalence and Genetics**. *Journal of Genetic Counseling* 2003, **12**:297-311.

21. Bonetta L: **Whole-Genome Sequencing Breaks the Cost Barrier**. *Cell* 2010, **141**:917-919.

22. Collins F: **Has the revolution arrived?** *Nature* 2010, **464**:674-675.

23. Teer JK, Mullikin JC: **Exome sequencing: the sweet spot before whole genomes**. *Hum Mol Genet* 2010, **19**:R145-151.

24. Venter JC: **Multiple personal genomes await**. *Nature* 2010, **464**:676-677.

25. Yngvadottir B, Macarthur DG, Jin H, Tyler-Smith C: **The promise and reality of personal genomics**. *Genome Biol* 2009, **10**:237.

26. Warner HR: **Medical informatics: a real discipline?** *J Am Med Inform Assoc* 1995, **2**:207-214.